INAUGURAL DISSERTATION

ZUR

ERLANGUNG DER DOKTORWÜRDE

DER

NATURWISSENSCHAFTLICH-MATHEMATISCHEN

GESAMTFAKULTÄT

DER

RUPRECHT–KARLS–UNIVERSITÄT

HEIDELBERG

VORGELEGT VON

DIPLOM–PHYSIKER PANAGIOTIS DROUVELIS

AUS ATHEN (GRIECHENLAND)

TAG DER MÜNDLICHEN PRÜFUNG: 02. 11. 2006

Electronic structure and quantum transport in systems of quantum dots exposed to magnetic fields

Gutachter: **Prof. Dr. Peter Schmelcher**
Prof. Dr. Jochen Schirmer

Abstract

The present thesis is about artificial nanostructures in which the electronic motion is restricted in all spatial dimensions precisely in the regime where quantum effects dominate. These structures which are called quantum dots can be prepared in the laboratory and offer a high degree of access to their electronic and transport properties thereby naturally being established as a prominent candidate for future nanoelectronics. In the present thesis a theoretical investigation of the electronic structure and quantum transport properties of quantum dots has been performed. In addition to the research performed, the theoretical framework for investigating transport through open and almost isolated quantum dots are reviewed. Thereby it is natural to divide the present contribution in two parts.

In the first part, which deals with transport in open quantum dot systems, we will contribute a parallel algorithm solving for the Green's function which goes beyond the trivial parallelization with regard to the external parameters of the transport problem, such as Fermi energy or magnetic field strength. Combining techniques of parallel linear algebra and cyclic reduction algorithms, the algorithm proceeds with the parallel treatment of the decomposed scattering region, thereby giving significant flexibility regarding the handling of highly demanding numerical problems as those encountered in materials with complex electronic structure (thereby requiring n-band effective mass models and atomistic Hamiltonians in order to be described). Further on, we apply our formalism to linear artificial crystals which are formed by quantum dots of various geometries. We review their properties from the perspective of building novel electronic devices based on quantum features and how they could operate at large temperatures.

In the second part of the thesis, we review the physics of almost isolated dots, whose transport properties are determined solely by their electronic structure. The effects of electron-electron interactions, anisotropy in the confinement and magnetic field on the electronic structure of two-electron quantum dots are calculated via a configuration interaction approach, i.e., exact diagonalization of the two-body Hamiltonian matrix. Additionally, we introduce a stable numerical method for the evaluation of matrix elements containing integrals due to electron-electron (e-e) interactions. In this respect we have employed a combination of Gauss-Hermite and Gauss-Kronrod quadratures, that has allowed for the efficient and direct evaluation of the e-e matrix elements with large basis sets. Contrary to previous works, we were able to calculate several hundreds of excited states. Subsequently those were analysed statistically making it possible to trace the quantum chaotic patterns in the dot-spectrum, which determine the fluctuations of electron transport coefficients and other spectroscopic and thermodynamic properties. As a supplementary tool for our investigations, classical dynamics have been studied in the corresponding classical phase space. Regarding the application of a magnetic field we introduced new maps of the low-lying excitation profile of the spectrum that allow the interpretation of experiments in few-electron quantum dots in a simple and straightforward manner. The experimental parameters are the strength of a homogeneous magnetic field applied vertically to the plane of the dot and the anisotropic shape of the dot. Many-body features due to strong e-e correlations can be easily identified by measurements.

Zusammenfassung

Das Thema dieser Dissertation sind künstliche Nanostrukturen in denen die Elektronenbewegung in allen räumlichen Dimensionen eingeschränkt ist. Diese Strukturen, die als Quantenpunkte bezeichnet werden, können im Labor hergestellt werden und bieten breite Zugriffsmöglichkeiten auf ihre elektronische Struktur und ihre Transporteigenschaften. Das macht sie zu vielsprechenden Kandidaten für zukünftige nanoelektronische Bauteile. Die vorgelegte Arbeit beinhaltet eine theoretische Untersuchung der elektronischen Struktur sowie der quantenmechanischen Transporteigenschaften in Systemen von Quantenpunkten. Wir geben eine Einführung in den theoretischen Rahmen zur Untersuchung von Quantentransport in offenen Quantenpunkte sowie in fast isolierten Systemen als Grenzfall. Deshalb ist die Arbeit in zwei Teile aufgeteilt.

Im ersten Teil behandeln wir Transport in offenen Quantenpunkten mit einer auf Green's Funktionen basierenden Methode. Wir präsentieren einen parallelen Algorithmus für den Transportformalismus, der auf der Zerlegung der mesoskopischen Region beruht und die Green's Funktion durch eine Kombination aus Verfahren der parallelen Linearen Algebra und zyklischer Reduktion berechnet. Dieses parallele Verfahren erlaubt die Behandlung von komplexen numerischen Problemen z.B. elektronischer Struktur in Materialien, welche eine Beschreibung durch einen "n-band effektive-mass" oder atomistischen Hamilton Operator erfordern. Im Anschluss wenden wir den Algorithmus auf künstliche, eindimensionale periodische Ketten aus Quantenpunkten mit unterschiedlichen geometrischen Charakteristika an. Wir beobachten einen Zusammenhang zwischen den Transporteigenschaften und der elektronischen Struktur des periodischen Systems. Dies erlaubt die Erkennung der elektronischen Bandstruktur unseres Systems sowie sein mögliche Funktion als elektronisches Schaltelement, das nur auf Quanteneffekten basiert.

Im zweiten Teil dieser Arbeit beschäftigen wir uns mit den physikalischen Prozessen in isolierten Quantenpunkten, in denen die Transporteigenschaften ausschliesslich durch ihre elektronische Struktur determiniert sind. Die Effekte von Elektron-Elektron Korrelationen, Anisotropie des harmonischen Potentials sowie eines homogenen Magnetfelds werden mit einer exakten Konfigurations-Wechselwirkungs-Methode untersucht. Zusätzlich führen wir ein numerisches Verfahren ein, das es uns erlaubt die numerische Instabilitäten bei der Berechnung der zwei-Elektronen Integralen zu vermeiden und die Matrix-elemente, sogar für ein grosses Basissatz, direkt und effizient zu berechnen. Dadurch war es möglich Energien von mehreren hundert aufgeregten Zuständen zu berechnen. Dia statistische Analyse der Energien hat uns erlaubt quantenchaotische Muster im Spektrum aufzuspüren. Zusätzlich haben wir eine detaillierte Untersuchung der Klassischen Dynamik beziehungsweise des klassischen Phasenraumes als Funktion der Anisotropie und der Stärke des Magnetfeldes durchgeführt. Ausserdem führen wir Abbildungen der energetisch niedrigen angeregten Zuständen als Funktion des Magnetfeldes und der Anisotropie ein, die ein einfaches und direktes Interpretation von Experimenten mit Quantenpunkten mit wenigen Elektronen ermöglichen.

Contents

Chapter 1

Introduction

The quest for numerical operations executed in an ultrafast time scale has led to a tremendous exponential increase in the number of the elementary circuits integrated on a chip. The current state of the art, i.e. the very large scale integration techonology, has allowed for millions of such circuits to be jammed on the wafer's surface, thereby arriving at the borders of reign of the classical Ohmic law. Unavoidably, the continuation of this trend, well known as the Moore's law, will lead to hybridization of the existing technology with quantum interference effects and ultimately to the design of devices which will be solely based on the latter. An exploration of the physics and possibilities that arise due to the gradual reduction of the devices' dimensions can be found for the non-specialist reader in Ref. [1]. The specialist reader could pump information from Refs. [2–4]. One of the most prominent candidates for quantum electronic devices is the quantum dot. The terminology dot is used to refer to a zero-dimensional structure which can be prepared as follows: a two-dimensional electron gas is formed by the successive arrangement of different semiconductor layers, i.e. a semiconductor heterostructure in the transversal direction. The electronic motion can be further constrained by applying an electrostatic potential via metal gates. The resulting potential confines one or more electrons in all three spatial dimensions. In terms of the density of states (DOS), a three-dimensional electron gas has a density of states $n_{3D}(E) \sim \sqrt{E}$ where E denotes the energy. In a two-dimensional electron gas the electronic motion is assumed to be quantized in the tranversal direction but free on the plane leading to a DOS being a sum of step functions. By further lowering the dimensions, i.e. restricting the electronic motion, we obtain a quantum wire, in which the DOS is $n_{1D}(E) \sim 1/\sqrt{E}$ and finally a quantum dot in which the electronic motion is spatially confined, thereby obtaining a discrete spectrum, and a DOS being a sum of δ-like peaks.

The confinement of the quantum dot's electrons takes place in the mesoscopic regime, i.e. on intermediate length scales with respect to the macrosopic solid state and the microscopic atomic regime. In practice the mesoscopic regime translates to dimensions comparable to the electron's Fermi wavelength λ_F, its mean free path L_0 and its phase relaxation length L_ϕ (for an illuminating discussion on these three length scales we refer the reader to Ref. [5]).

The scattering of an electron with a time independent scatterer is phase coherent. At low temperatures, static impurities in the semiconductor like the boundaries of the sample, can be treated as phase coherent scatterers. Therefore, L_ϕ can be significantly larger than L_0, giving rise to quantum interference effects. A few hallmarks of the latter can be considered the weak localization [6], the universal conductance fluctuations [7, 8] and the Aharonov-Bohm effect [9]. A pedagogical discussion of these effects can be found in Ref. [5]. Indeed phase-relaxation can be induced if the electron accesses a scattering channel that changes its state. Conceptually by measuring the state after scattering, we have an information about the electron's path and quantum interference is suppressed. Sources of phase-randomization can be attributed to non-stationary (fluctuating) impurities such as electron-phonon (e-p) and electron-electron (e-e) interactions or spin-flip scattering with magnetic impurities.

Mesoscopic effects can be probed to a large extent in a quantum dot due to the high degree of access and even manipulation it offers on its internal degrees of freedom. The information about the physics of the quantum dot comes from its coupling to the environment, which in our case are the attached leads. The coupling between the dot and the leads can be tuned by electrostatic gates, so that it allows us to distinguish between quantum dots which are strongly or weakly coupled to the leads, and they are called open or closed, respectively. Let us briefly summarize the meaning of the coupling strength. The coupling of the dot to the leads introduces a finite level-width in the DOS of the dot. In an open dot, the width of the lead may accomodate a large number of propagating modes with large transmission coefficients. Thus, the resonant-type levels of the dot strongly overlap and induce fluctuations in the conductance. On the other hand, for closed dots the transmission coefficients are very small and the dot's conductance exhibits peaks which correspond to resonant tunneling between the leads and the quantum dot's energy levels.

Quantum dots, intriguing as much as extensively investigated [10], remain a research field that continues to provide new insights in fundamental questions concerning nature and their properties are to a large extent the main field of investigation of the present thesis, which is divided in two parts. The first part provides the basis for understanding quantum transport through systems of open quantum dots whereas the second one deals with closed quantum dots and provides a detailed overview on the effects of asymmetry in the confinement, magnetic field and e-e interaction on their electronic properties. The thesis is structured as follows. In chapter 2 we introduce the Landauer formalism for treating linear quantum transport through open quantum dots. In chapter 3 we present a parallel algorithm for the numerical evaluation of the formalism derived in the preceding chapter. This technique combines algorithms borrowed from parallel linear algebra and parallel cyclic reduction for the transfer of the information. This algorithm is used to calculate the transport properties in systems of open quantum dots. Furthermore it offers a deeper and more practical insight in the computational aspects of the Landauer theory. Chapter 4 contains an investigation of quantum transport through open quantum dot arrays. In the latter quantum transport is mediated by the formation of artificial energy bands due to the successive repetition of the

quantum dot cells. By changing the geometry of the coupling media as well as by applying an external magnetic field of moderate strength we are allowed to observe a magnetically controlled linear response current which can flow coherently for several tens of Kelvin and owes to the electronic band structure of the periodic system. Furthermore we will proceed with the investigation of isolated quantum dots. In chapter 5 the weak coupling regime and the conditions that define it will be discussed, providing a short review of the prominent phenomena and the wealth of literature that accompanies this regime. At hand of the considerations of the chapter 5, in chapter 6 we are going to perform a detailed investigation of the electronic properties of a two-electron quantum dot which is confined in an anisotropic potential. This small system provides a fundamental working Hamiltonian which is also ideal for a statistical analysis of the spectrum in order to investigate quantum to classical correspondence effects. Chapter 7 will present the response of the electronic properties of the system in the presence of an external homogeneous magnetic field. Finally, in chapter 8 we will draw the conclusions of the research we have performed.

Chapter 2

Theory of linear quantum transport through quantum dots

2.1 Computational aspects of the single-particle Landauer theory

In this chapter we are going to present the Landauer formalism which has associated the quantum-mechanical probability for an electron to transmit through a sample with its quantum transport properties such as conductance [11]. For the purposes of our investigations we assume that current flow in semicounductor heterostructures can be described in terms of the Fermi Liquid theory. In this picture, the low-energy excitations (quasiparticles) behave as a degenerate noninteracting Fermion gas (DNFG) in the sense that the mass of the particles is renormalized due to screened interactions with the atoms of the crystal and the band structure. In this context let us assume a two-probe setup, i.e. two leads, which act as electronic reservoirs, are attached to a mesoscopic scattering region. The two-probe setup we describe is illustrated schematically in Fig.2.1, for an arbitrary scattering region,

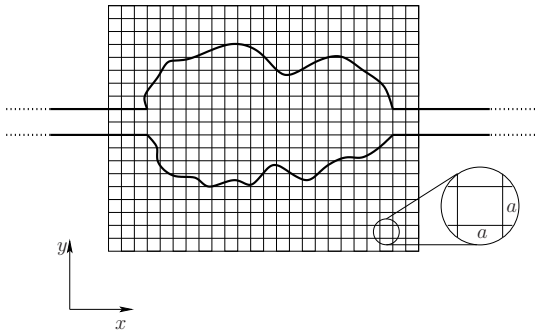

Figure 2.1: Arbitrary scattering region attached to two reservoirs.

Inside the leads we assume a DNFG that fills the energies up to the Fermi energy E_F.

The Hamiltonian of the composite system (leads + scattering region) can be described by the general Hamiltonian in the notation of second quantization [12],

$$H = \sum_{ka \in K} \epsilon_{ka} c^{\dagger}_{ka} c_{ka} + H_S(d^{\dagger}_n; d_n) + \sum_{ka \in K; n} (V_{ka,n} c^{\dagger}_{ka} d_n + h.c.) \tag{2.1}$$

in which the operators $c^{\dagger}_{ka}(c_{ka})$ create (destroy) an electron in the state with momentum k and a unique quantum number a either in the left ($K = L$) or right ($K = R$) lead with a Fermi distribution $f(\epsilon_{ka}) = [exp(\frac{\epsilon_{ka}-E_F}{k_B T}) + 1]^{-1}$. Operators $d^{\dagger}_n, d_n$ form a complete orthonormal creation and annihilation set of the states $|n\rangle$ in the scattering region. For our investigations we restrict to the case of non-interacting electrons inside the scattering region and we remain with this picture throughout our investigations and definitions. For this picture the Hamiltonian for the scattering region reduces to $H_S(d^{\dagger}_n; d_n) = \sum_{nm} \epsilon_{nm} d^{\dagger}_n d_m$.

In the noninteracting picture, the conductance for electrons with Fermi energy E_F is given by the Landauer formula:

$$G(E_F) = \frac{2e^2}{hV_{SD}} \int_{-\infty}^{\infty} T(E)(f_L(E) - f_R(E))dE \tag{2.2}$$

where $T(E)$ is the transmission coefficient and denotes the probability that an electron with Fermi energy E will transmit through a mesoscopic scatterer. For the explicit evaluation of $T(E)$, we refer the reader to section 2.2. The leads are modeled by a DNFG with a Fermi distribution $f_K(E) = [exp(\frac{E-\mu_K}{k_B T}) + 1]^{-1}$, $\mu_K = E_F \pm \frac{eV_{SD}}{2}$ being the chemical potential in the left and right lead, when applying a bias voltage V_{SD}. A large applied bias voltage V_{SD} causes a modification to the confining potential due to the accumulated charge at the boundaries of the conductive medium with th leads. The new modified potential profile can be obtained by solving self-consistenly the Poisson and the Schrödinger equation. The latter is pedagogically presented in Ref. [2]. An analysis of this situation goes beyond the scope of the present contribution, in which we do not address such effects, i.e. $V_{SD} \to 0$ and its role restricts to the one that enforces current flow. In this regime, the so called linear response regime,

$$G_{l.r.}(E_F) = \lim_{V_{SD} \to 0} G(E_F) = \frac{2e^2}{h} \int_{-\infty}^{\infty} T(E) \left(-\frac{\partial f_0}{\partial E} \right) dE \tag{2.3}$$

with $f_0(E) = [exp(\frac{E-E_F}{k_B T}) + 1]^{-1}$. Hereafter, we will use the notation $G_{l.r.}(E_F) \equiv G(E_F)$. For zero temperature the conductance is given by,

$$G(E_F) = \frac{2e^2}{h} T(E_F) \tag{2.4}$$

So far, we have introduced the two-probe Landauer formula for non-interacting electrons propagating along a mesoscopic sample. This formalism can take into account electron/electron interactions in terms of non-interacting particles moving in a mean field, i.e. the Hamiltonian to be the Fock matrix, or within density functional theory for electrons described by the Kohn-Sham Hamiltonian. If one would like to generalize this formalism to a strongly interacting system beyond mean field theories one has to proceed with a more general expression for the conductance which exploits the Keldysh (or Kadanoff-Baym) formalism [13]. However, within our approach to quantum transport we are going to deal with elastic scattering of non-interacting electrons due to the boundaries of a region in the linear response regime. In the next section, we present the computational aspects for the calculation of the quantum transport properties in the framework of the Landauer formalism.

2.2 Computational aspects of the Landauer formalism

As we saw in the previous section, the conductance of a mesoscopic sample attached to two reservoirs (Fig. 2.1) is proportional to the quantum-mechanical probability $T(E)$ that an incoming electron at Fermi energy E in the reservoirs will transmit through it. To evaluate the transmission probability $T(E)$ one has to solve the Schrödinger equation:

$$\lim_{\eta \to 0^+} (E - H(\mathbf{r}) + i\eta) G_0(\mathbf{r}; \mathbf{r}') = \delta(\mathbf{r} - \mathbf{r}') \tag{2.5}$$

where $H(\mathbf{r})$ is the Hamiltonian of eq.(2.1) and $G_0(\mathbf{r}; \mathbf{r}')$ is the Green's function operator of the open system (scatterer + reservoirs). We remark that the above definition holds if the Hamiltonian H can be expressed in terms of single-particle operators. In the following we restrict ourselves to two-dimensional ($2D$) quantum transport, as it is shown in Fig.2.1. Transport in $2D$ can be realised experimentally if the electrons occupy the ground state in the z- direction and excitations can occur in the other two dimensions, i.e. as in the case of a $2D$ electron gas. To proceed with the calculation of $T(E)$ we discretize the space on a uniform lattice with constant a. In order to represent the Hamiltonian operator $H(\mathbf{r})$ we use the tight-binding model assuming only nearest neighbor interactions [14]. In this case the Hamiltonian can be written:

$$\mathbf{H}(\mathbf{r}) = \sum_{\mathbf{r}} |\mathbf{r}\rangle \epsilon_{\mathbf{r}} \langle \mathbf{r}| + \sum_{\mathbf{r}, \mathbf{\Delta r}} |\mathbf{r}\rangle V_{\mathbf{r}, \mathbf{\Delta r}} \langle \mathbf{r} + \mathbf{\Delta r}| \tag{2.6}$$

where $\epsilon_{\mathbf{r}}$ is called on-site energy at the position $\mathbf{r} = (x, y)$ with $x = na$ and $y = ma$, $n, m \in \mathcal{N}$, $\mathbf{\Delta r}$ represents the vectors from $\mathbf{r}$ to their nearest neighbor sites and $V_{\mathbf{r},\mathbf{\Delta r}}$ is the nearest neighbor hopping energy. For a constant on-site energy the dispersion relation for the $2D$ discretized lattice reads:

$$E_{2D}(\mathbf{k}) = 4V - 2Vcos(k_x a) - 2Vcos(k_y a) \tag{2.7}$$

Here $\mathbf{k} = (k_x, k_y)$ is the electron's wavevector and $V = \hbar^2/(2m^* a^2)$ is the matrix hopping element linking each site to its nearest neighbor. In the limit $a \to 0$ we recover the usual parabolic relationship of a free particle in a continuum space. In practice, the condition to converge to the continuum dictates that the number of lattice sites in the transversal direction that couple the scatterer with the leads is much larger than the number of channels we have opened with our Fermi energy, times π, i.e.:

$$N_D + 1 >> (\#\ of\ open\ channels) \times \pi$$

where $D = (N_D + 1)a$ is the width of the lead and N_D the number of lattice sites that couple to the scatterer.

The full tight-binding Hamiltonian of the open system (scatterer + leads) can be then decomposed in the following block form:

$$\mathbf{H}(\mathbf{r}) = \begin{pmatrix} \mathbf{H_L} & \mathbf{V_L} & \mathcal{O} \\ \mathbf{V_L^\dagger} & \mathbf{H_S} & \mathbf{V_R} \\ \mathcal{O} & \mathbf{V_R^\dagger} & \mathbf{H_R} \end{pmatrix}$$

where the Hamiltonian $\mathbf{H_S}$ is the matrix representation of H_S and the coupling to the two external reservoirs from the left and right, is described via the semi-infinite matrices $\mathbf{V_L}$ and $\mathbf{V_R}$, respectively. The matrices of the Hamiltonian operators $\mathbf{H_L}$ and $\mathbf{H_R}$ are of infinite size and describe the electronic flow within the reservoirs.

One can accordingly partition the overall Green's function operator $\mathbf{G_0}(E)$ of equation (2.5) such that,

$$\begin{pmatrix} (E+i\eta)\mathbf{I} - \mathbf{H_L} & \mathbf{V_L} & \mathcal{O} \\ \mathbf{V_L^\dagger} & (E+i\eta)\mathbf{I} - \mathbf{H_S} & \mathbf{V_R} \\ \mathcal{O} & \mathbf{V_R^\dagger} & (E+i\eta)\mathbf{I} - \mathbf{H_R} \end{pmatrix} \cdot \begin{pmatrix} \mathbf{G_L} & \mathbf{G_{LS}} & \mathbf{G_{LR}} \\ \mathbf{G_{SL}} & \mathbf{G_S} & \mathbf{G_{SR}} \\ \mathbf{G_{RL}} & \mathbf{G_{RS}^\dagger} & \mathbf{G_R} \end{pmatrix} = \mathbf{I}$$

If we solve the above set of equations for $\mathbf{G_S}(E)$ we receive the following expression

$$\mathbf{G_S}(E) = [E\mathbf{I} - \mathbf{H_S} - \mathbf{\Sigma_R}(E) - \mathbf{\Sigma_L}(E)]^{-1} \tag{2.8}$$

This is the so called Dyson equation for the Green's function of the composite system (leads + scatterer) which can also be expressed as:

$$\mathbf{G_S}(E) = \mathbf{g_S}(E) + \mathbf{g_S}(E)\mathbf{\Sigma}(E)\mathbf{G_S}(E) \tag{2.9}$$

or alternatively: $\mathbf{G_S}(E) = (\mathbf{g_S}^{-1}(E) - \mathbf{\Sigma}(E))^{-1}$. The total self-energy matrix $\mathbf{\Sigma}(E) = \mathbf{\Sigma_L}(E) + \mathbf{\Sigma_R}(E)$ takes into account the effect of the coupling to the reservoirs, via the so called self-energy matrices $\mathbf{\Sigma_K}(E) = \mathbf{V_K^\dagger g_K}(E)\mathbf{V_K}$ due to the left ($\mathbf{K} = \mathbf{L}$) and right ($\mathbf{K} = \mathbf{R}$) reservoir. The function $\mathbf{g_K}$ is the matrix representation of the retarded Green's function operator of the reservoir $\mathbf{K}$, i.e., $\mathbf{g_K}(E) = [(E + i\eta)\mathbf{I} - \mathbf{H_K}]^{-1}$.

We consider that the electrons occupy states at the middle (energetically lowest) point of a conduction band which is parabolic. In the case that the electrons are freely propagating along the x-direction and are confined in the y-direction then the matrix elements for the Green's function at the interface of the lead with the scatterer, let us say at an arbitrary position $x = x_S$, can be evaluated analytically using the expression [5],

$$g_K(x_S, y; x_S, y') = -\frac{1}{V}\sum_m \chi_m(y)\chi_m(y')e^{ik_m a} \tag{2.10}$$

in which the transversal mode eigenfunctions satisfy the equation

$$\left(-\frac{\hbar^2}{2m}\frac{d^2}{dy^2} + U(y)\right)\chi_m(y) = \epsilon_m\chi_m(y) \tag{2.11}$$

with $U(y)$ being the confinement potential along the y-direction and k_m the wavevector along the x-direction which satisfies the $1D$ dispersion relation. As we can see the expression for the surface Green's functions in the leads does not depend on the position x_S along the x-axis of the interface with the scatterer.

Due to the tight-binding discretization, the space of the scattering region now consists of $n = 1, 2 \ldots, N$ slices along the x-direction each of which consists of $m = 1, 2, \ldots, M$ sites along the y-direction. The matrix $\mathbf{A} = E\mathbf{I} - \mathbf{H_S} - \mathbf{\Sigma_R}(E) - \mathbf{\Sigma_L}(E)$ we want to invert in order to evaluate $\mathbf{G_S}(E)$ is a $N \times N$ block tridiagonal matrix [14] whose elements are the blocks $\mathbf{A_{ij}}$ each of which is of size $M \times M$:

$$\mathbf{A} = \begin{pmatrix} \mathbf{A_{11}} & \mathbf{A_{12}} & \mathcal{O} & \cdots & \mathcal{O} & \mathcal{O} & \mathcal{O} \\ \mathbf{A_{21}} & \mathbf{A_{22}} & \mathbf{A_{23}} & \cdots & \mathcal{O} & \mathcal{O} & \mathcal{O} \\ \mathcal{O} & \mathbf{A_{32}} & \mathbf{A_{33}} & \cdots & \mathcal{O} & \mathcal{O} & \mathcal{O} \\ \vdots & \vdots & \vdots & \ddots & \vdots & \vdots & \vdots \\ \mathcal{O} & \mathcal{O} & \mathcal{O} & \cdots & \mathbf{A_{N-2,N-2}} & \mathbf{A_{N-2,N-1}} & \mathcal{O} \\ \mathcal{O} & \mathcal{O} & \mathcal{O} & \cdots & \mathbf{A_{N-1,N-2}} & \mathbf{A_{N-1,N-1}} & \mathbf{A_{N-1,N}} \\ \mathcal{O} & \mathcal{O} & \mathcal{O} & \cdots & \mathcal{O} & \mathbf{A_{N,N-1}} & \mathbf{A_{N,N}} \end{pmatrix}$$

The expression for the evaluation of $T(E)$ is given in a compact form by the Fisher-Lee relation [15]:

$$T(E) = Tr[\mathbf{\Gamma_R}(E)\mathbf{G_S}(E)\mathbf{\Gamma_L}(E)\mathbf{G_S^\dagger}(E)] \tag{2.12}$$

where $\mathbf{\Gamma_K}(E) = i[\mathbf{\Sigma_K}(E) - \mathbf{\Sigma_K^\dagger}(E)]$ is the strength of the coupling of the reservoir $\mathbf{K}$ to the scatterer. Due to the fact that the reservoirs are coupled only to the left and right of the scatterer, the blocks that correspond to the left interface of the scatterer with the lead, i.e. the upper left block $\sigma_\mathbf{L}(E)$ of $\mathbf{\Sigma_L}(E)$, and to the right interface of the scatterer with the lead, i.e. the down right block $\sigma_\mathbf{R}(E)$ of $\mathbf{\Sigma_R}(E)$, are the nonzero blocks of the matrices $\mathbf{\Sigma_K}(E)$. Therefore, the total self-energy due to the right and left reservoir has the following block structure:

$$\mathbf{\Sigma_L}(E) + \mathbf{\Sigma_R}(E) = \begin{pmatrix} \sigma_\mathbf{L}(E) & \mathcal{O} & \mathcal{O} & \cdots & \mathcal{O} & \mathcal{O} & \mathcal{O} \\ \mathcal{O} & \mathcal{O} & \mathcal{O} & \cdots & \mathcal{O} & \mathcal{O} & \mathcal{O} \\ \mathcal{O} & \mathcal{O} & \mathcal{O} & \cdots & \mathcal{O} & \mathcal{O} & \mathcal{O} \\ \vdots & \vdots & \vdots & \ddots & \vdots & \vdots & \vdots \\ \mathcal{O} & \mathcal{O} & \mathcal{O} & \cdots & \mathcal{O} & \mathcal{O} & \mathcal{O} \\ \mathcal{O} & \mathcal{O} & \mathcal{O} & \cdots & \mathcal{O} & \mathcal{O} & \mathcal{O} \\ \mathcal{O} & \mathcal{O} & \mathcal{O} & \cdots & \mathcal{O} & \mathcal{O} & \sigma_\mathbf{R}(E) \end{pmatrix}$$

Due to this structure of the self-energy matrix, only the upper left block of $\mathbf{\Gamma_L}(E)$, $\gamma_\mathbf{L}(E) = i(\sigma_\mathbf{L}(E) - \sigma_\mathbf{L}^\dagger(E))$ and the down right block of $\mathbf{\Gamma_R}(E)$, $\gamma_\mathbf{R}(E) = i(\sigma_\mathbf{R}(E) - \sigma_\mathbf{R}^\dagger(E))$ are nonzero. Hence, the trace of the product of the four matrices occuring in equation (2.12) simplifies to:

$$T(E) = Tr[\gamma_\mathbf{R}(E)\mathbf{G_{1,N}}(E)\gamma_\mathbf{L}(E)\mathbf{G_{1,N}^\dagger}(E)] \tag{2.13}$$

Equation (2.13) implies that only the upper right block of the inverse of $\mathbf{A}$, $\mathbf{A_{1,N}^{-1}} = \mathbf{G_{1,N}}$ is necessary for the evaluation of $T(E)$. The ultimate goal is therefore to compute $\mathbf{A_{1,N}^{-1}}$. The

physical interprentation of this result is that $\mathbf{G_{1,N}}$ is the Green's function containing the information for the transmission from slice with label 1 to slice with label N. For example if we would attach an additional lead to slice with label e.g. 10 in order to find the transmission from 1 to 10 one should calculate the Green's function $\mathbf{G_{1,10}}$ and naturally for the transmission from 10 to N the Green's function $\mathbf{G_{10,N}}$ is required. Since we have in mind the interpretation for the particular blocks of the Green's function matrix we could proceed with introducing a multi-probe Landauer formalism, which is particularly useful to interpret experimental setups or to estimate decoherent components in transport via a model suggested by Büttiker [16].

2.3 Büttiker model

So far we have addressed a two-probe setup in which only two leads are attached to the scatterer at the left and right part of it, i.e. we have a longitudinal symmetry for the current flow (there are no transversal components of the current). In this section we are going to review a general setup in which N maximum additional probes are attached transversally to each slice that forms the discrete representation of the scatterer thereby breaking the longitudinal symmetry in the current flow and introducing transversal components. Figure 2.2 shows such a setup. In order to avoid confusion with section 2.2 and the same time for convenience, we note that the symbol G whenever used throughout this section refers to the conductance.

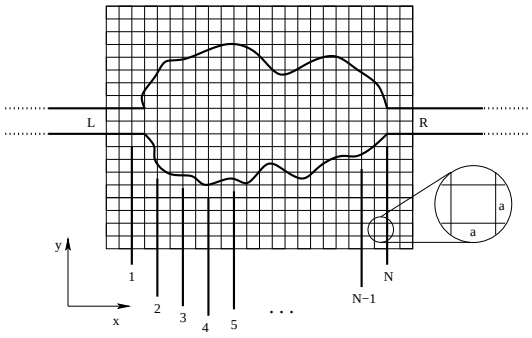

Figure 2.2: Arbitrary scattering region attached N probes in the transversal direction.

Multiprobe setups are very common experimentally since they offer a larger degree of control and possibilities to the experimental quantities. For our purposes we will introduce them for one single reason. We are going to estimate the effect of phase-breaking processes in the process of longitudinal current flow due to electron-phonon (e-p) scattering. As we have previously remarked the electrons propagate in a conductive medium in the vicinity of the atoms that form the crystal of the material. With increasing temperature, the vibrations of the lattice couple to the electronic motion thereby changing its electronic state, leading to a loss of its quantum-mechanical phase. Hence, if one would like to obtain a picture of

quantum transport at large temperatures he should include such e-p scattering processes. One way to proceed is to calculate perturbatively the effect of e-p scattering using diagrammatic theory [5]. A much simpler way to estimate the contribution to decoherence is the so-called Büttiker model [16] which is based on the N-probe Landauer formalism. According to this model one could attach N virtual probes along the scatterer, the role of which is solely restricted to the one that randomizes the phase of the electron. The effect of e-p scattering could be then simulated in terms of collisions of the electrons with these probes. For these virtual probes there is no contribution to the current flow and therefore we are led to the condition $I_i = 0$ for $i = 1 \ldots N$. Their effect can be estimated by taking into account a self-energy due to the attachment of the probes to the scatterer and an additional contribution to the total longitudinal transmission which can be calculated in the following way. If we label, for the sake of simplicity, the left lead with zero ($L \equiv 0$) and the right lead with $N+1$ ($R \equiv N+1$) then we have a matrix representation $\mathbf{I} = \mathbf{GV}$ that links the components of currents I_i and voltages V_i via their individual conductances G_{ij} and which leads to the general relationship for the current flow in each probe-lead,

$$I_i = \sum_{\substack{j=0 \\ j \neq i}}^{N+1} G_{ij}(V_i - V_j); \quad i = 0, \ldots, N+1 \tag{2.14}$$

Hence, the current that flows to the right ($N+1$) reservoir is given by the equation,

$$I_{N+1} = -G_{N+1,0}V_0 - \sum_{j=1}^{N} G_{N+1,j}V_j \tag{2.15}$$

In equation 2.15 we have chosen $V_{N+1} = 0$ as a reference for the applied voltages. In this equation $G_{N+1,0} = \frac{2e^2}{h}T_{N+1,0}$ for zero temperature, i.e. the longitudinal transmission coefficient from left to right. In order to calculate the V_j we exploit the fact that $I_i = 0$ for $i = 1 \ldots N$,

$$\sum_{\substack{j=0 \\ j \neq i}}^{N+1} G_{ij}(V_i - V_j) = 0; \quad i = 1, \ldots, N \tag{2.16}$$

If we set $g_i = \sum_{\substack{j=0 \\ j \neq i}}^{N+1} G_{ij}$ and for $V_{N+1} = 0$ the equation 2.16 can be written as,

$$g_i V_i - \sum_{\substack{j=1 \\ j \neq i}}^{N} G_{ij}V_j = G_{i,0}V_0; \quad i = 1, \ldots, N \tag{2.17}$$

Now let us define a matrix $\mathbf{W}$ the matrix elements of which are $W_{ij} = g_i\delta_{ij} - (1 - \delta_{ij})G_{ij}$. Obviously for $i = j$ the transmission coefficients G_{ii} which translate simply to backscattering to the same lead are not required. The diagonal elements of this matrix are the quantities g_i and the off-diagonal elements correspond to G_{ij}. Both indices $i, j = 1 \dots N$. Hence, equation 2.17 can be written in a compact form,

$$\sum_{j=1}^{N} W_{ij}V_j = G_{i,0}V_0 \tag{2.18}$$

or in a matrix representation $\mathbf{WV} = \mathbf{G_0}V_0$ where $\mathbf{V}$ corresponds to a column vector with components V_j and $\mathbf{G_0}$ a column vector with components $G_{i,0}$. Easily by inverting the matrix $\mathbf{W}$ we can evaluate each voltage V_j and end up with a final expression for the current total current flow to the right including simultaneously the effect of non-current flowing probes,

$$I_{N+1} = -G_{N+1,0}V_0 - \sum_{j=1}^{N}\sum_{i=1}^{N} G_{N+1,j}\mathbf{W}^{-1}_{ji}G_{i,0}V_0 \tag{2.19}$$

The corresponding expression for the transmission coefficients follows readily if we consider that $I_{N+1} = G_{tot}V_0$ and assume for zero temperature that $G_{ij} = \frac{2e^2}{h}T_{ij}$ for all participating probes. In this regard the total transmission coeffiecient from left to right taking into account the possibility of collisions of electrons with the probes is given by,

$$T_{tot} = T_{N+1,0} + \sum_{j=1}^{N}\sum_{i=1}^{N} T_{N+1,j}\mathbf{W'}^{-1}_{ji}T_{i,0} \tag{2.20}$$

in which case the matrix $\mathbf{W} = \frac{2e^2}{h}\mathbf{W'}$ for zero temperature. This expression is the one used in Ref. [17] in order to describe in a phenomenological way the effect of e-p interactions in the decoherence of molecular conductors and can be viewed as a generalization of the single-probe Büttiker model for decoherence [16]. In order to calculate the full longitudinal transmission coefficient it is clear from equation 2.20 that one has to calculate the whole set of transmission coefficients between each attached probe (see matrix elements of $\mathbf{W}$). In the case that we have no magnetic field then the following symmetry property holds $T_{ij} = T_{ji}$ which comes from the fact that the Green's function matrix is transpose. If we apply magnetic field then the above symmetry property does not apply. Mathematically, the Peierls factor introduces a phase which couples the off-diagonal elements of the tight-binding Hamiltonian leading to the loss of the above mentioned symmetry for the Green's functions. This can be interpreted in physical terms by the fact that the path that an electron has followed can not be time-reversed just like in the absence of the magnetic field. This

becomes more clear if we think of an electron injected from the left lead to probe with label 1 in figure 2.2. Then the electron is reinjected, since $I_1 = 0$, but due to the magnetic field obviously it will not follow the same path back to the left lead.

This effect is responsible for the destruction of the weak localization's signature in the mesoscopic conductance. Briefly, weak localization means that the mesoscopic conductance is corrected due to coherent backscattering if we sum over all contributions of the paths that the electron can follow. In the presence of magnetic fields this correction vanishes. For a pedagogical discussion of this effect we refer the reader to Ref. [5].

Chapter 3

Parallel recursive Green's function method

3.1 Introduction

The theoretical framework for the description of mesoscopic electronic transport has been established within the Landauer formalism, which we introduced in chapter 2. This formalism relies on the computation of the transmisison coefficient, i.e. the probability that an electron injected into a mesoscopic sample will transmit through it. To this end, several numerical techniques have been developed and applied in order to calculate the transmission coefficient and describe various physical setups. The most efficient method to attack the problem of quantum transport has proven to be the recursive Green's function (RGF) approach. The general framework for this approach can be found in Ref. [14] and depending on the emphasis of the individual scattering problem, alternative numerical techniques can be applied. Therefore, RGF method adapted to the subdivision of transversal modes in a wire allowed for the efficient simulation of the fully diffusive regime [18] and techniques such as the boundary element method [19], with an emphasis on the arbitrary geometry of the scattering region, or the modular Green's function method [20, 21], in which the scattering region is initially decomposed in modules which are finally joined via the Dyson equation, have been developed to take into account the particular geometrical features of the scattering problem. Recently, a RGF technique has been applied to describe scanning probe experiments [22]. This technique describes tunneling, through the STM tip, which comprises the whole scattering area but scales equally well with the standard RGF method. As an alternative solution to improve the efficiency and consequently the capability to treat larger systems, approximations in the Schrödinger eigenvalue problem, as in the contact block reduction method [23, 24], have been employed to treat multi-terminal three-dimensional problems with relatively good accuracy.

The aim of this chapter is to present a parallel algorithm for the computation of the electronic transmission probability, within the framework of the RGF method. This algorithm

goes beyond the straightforward parallelization of the external parameters of the problem such as the range of Fermi energies and magnetic fields but divides the scattering region into subblocks, which are treated in parallel. In this regard, the parallelization will allow us to reduce the computational time and treat large systems with many degrees of freedom. It will also be particularly efficient to handle highly complex modular scattering structures for which the serial RGF algorithm is not applicable on a reasonable time scale. This chapter is organized as follows. In section 3.2 we present the parallel algorithm and calculate its numerical complexity. Section 3.3 contains an analysis of performance and scalability for certain numerical benchmarks. Within this investigation useful conclusions for the optimal use of our algorithm will be deduced. Finally, section 3.4 draws our main conclusions.

3.2 The parallel algorithm

The overall scattering problem, as discussed in section 2.2, can be algebraically translated to a $N \times N$ block tridiagonal matrix $\mathbf{A} = E\mathbf{I} - \mathbf{H} - \mathbf{\Sigma_R}(E) - \mathbf{\Sigma_L}(E)$ of which each block is of size $M \times M$. The goal is to compute the upper right block of the inverse of $\mathbf{A}$, $\mathbf{A^{-1}_{1,N}}$. The inverse of a band matrix is in general a full matrix. Applying a Gaussian elimination in order to calculate $\mathbf{A^{-1}_{1,N}}$ requires storage and processing of many more blocks of $\mathbf{A^{-1}}$. This so called fill-in can be reduced by applying an appropriate permutation to the matrix $\mathbf{A}$ before calculating the inverse. In the following we show, how we can exploit permutations in order to efficiently evaluate $\mathbf{A^{-1}_{1,N}}$ by introducing an expression of $\mathbf{A^{-1}}$ via the Schur's complement block $\mathbf{S}$. This expression allows an effective parallelization, because it involves only the inversion of a block diagonal matrix, products of sparse matrices and finally, at the last step the inversion of $\mathbf{S}$, which is even still a full matrix but much smaller than $\mathbf{A}$ itself.

3.2.1 Prerequisites

The algorithm that we pursue should possess the following properties:

1. Storage requirements should be restricted to a small number of blocks of size $M \times M$.

2. The number of inversions and multiplications of the $M \times M$ blocks $\mathbf{A_{ij}}$, which are the dominant contributions to the computational cost because they scale with M^3, should be proportional to N. This corresponds to the numerical complexity of the sequential RGF technique in the asymptotic limit of large N and M:

$$C_{\mathrm{seq}}(N, M) \approx NM^3$$

3. Exploit the fact that the Hamiltonian matrix $\mathbf{H_S}$ is Hermitian, leading to a block Hermitian matrix $\mathbf{A}$, i.e., for the off-diagonal blocks is claimed that $\mathbf{A^{\dagger}_{ij}} = \mathbf{A_{ji}}$.

4. The algorithm should be parallelizable.

3.2.2 Preparations

Change of the inverse under permutation

Let $\mathbf{P_{ij}}$ be an elementary permutation matrix with the following properties:

1. Set $\tilde{\mathbf{A}} = \mathbf{P_{ij}A}$, then $\tilde{\mathbf{A}}$ is identical to $\mathbf{A}$ except that rows i and j are interchanged.
2. Set $\tilde{\mathbf{A}} = \mathbf{AP_{ij}}$, then $\tilde{\mathbf{A}}$ is identical to $\mathbf{A}$ except that columns i and j are interchanged.
3. $\mathbf{P_{ij}^T} = \mathbf{P_{ij}} = \mathbf{P_{ji}}$.
4. $\mathbf{P_{ij}} \cdot \mathbf{P_{ij}^T} = \mathbf{I}$, i.e., $\mathbf{P_{ij}}$ is orthogonal and self-inverse $\mathbf{P_{ij}} = \mathbf{P_{ij}^{-1}}$.

We call $\mathbf{P} = \mathbf{P_{i_n,j_n}} \dots \mathbf{P_{i_1,j_1}}$ a permutation matrix. Then $\mathbf{P^{-1}} = (\mathbf{P_{i_n,j_n}} \cdot \dots \cdot \mathbf{P_{i_1,j_1}})^{-1} = \mathbf{P_{i_1,j_1}^{-1}} \cdot \dots \cdot \mathbf{P_{i_n,j_n}^{-1}} = \mathbf{P_{i_1,j_1}} \cdot \dots \cdot \mathbf{P_{i_n,j_n}} = \mathbf{P^T}$. Now if we apply row and column permutations to the matrix $\mathbf{A}$, $\tilde{\mathbf{A}} = \mathbf{PAP^T}$ then for the inverse we have that $\tilde{\mathbf{A}}^{-1} = (\mathbf{PAP^T})^{-1} = \mathbf{P^{-T}A^{-1}P^{-1}} = \mathbf{PA^{-1}P^T}$.

The above imply the following two alternative paths for the computation of $\mathbf{A_{1,N}^{-1}}$:

(a) Starting from $\mathbf{A}$ we compute the inverse of it. Then by applying the appropriate row and column permutations, through operation of the permutation matrices, it is possible to shift the desired upper right block $\mathbf{A_{1,N}^{-1}}$ in another position of the inverse. Respectively, the down left block of $\mathbf{A}$ is also shifted. This first path can be illustrated graphically as follows:

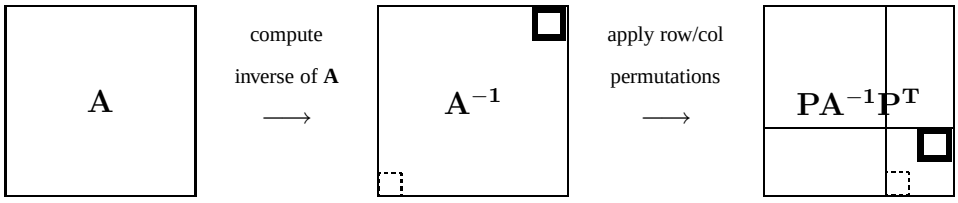

(b) Alternatively, if we start by applying row and column permutations in the initial matrix $\mathbf{A}$, then we can shift the upper right block $\mathbf{A_{1,N}}$ into another position. If we compute the inverse of the new matrix then the desired block $\mathbf{A_{1,N}^{-1}}$ will be located at the same position. Graphically, this second path implies:

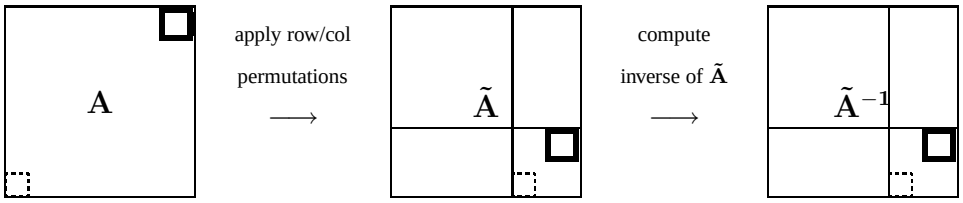

Therefore, the diagram implies that *computation of the desired block of the inverse matrix* $\mathbf{A}^{-1}_{1,\mathrm{N}}$ *by following path (a) is equivalent to the computation of* $\mathbf{A}^{-1}_{1,\mathrm{N}}$ *by following path (b)* .

Expression of the inverse via the Schur complement

Let any matrix $\mathbf{A}$ with a general 2×2 block structure:

$$\mathbf{A} = \begin{pmatrix} \mathbf{A_{11}} & \mathbf{A_{12}} \\ \mathbf{A_{21}} & \mathbf{A_{22}} \end{pmatrix}$$

Then the inverse of $\mathbf{A}$ in block form is:

$$\mathbf{A^{-1}} = \begin{pmatrix} \mathbf{A_{11}^{-1}} + \mathbf{A_{11}^{-1}A_{12}S^{-1}A_{21}A_{11}^{-1}} & \mathbf{-A_{11}^{-1}A_{12}S^{-1}} \\ \mathbf{-S^{-1}A_{21}A_{11}^{-1}} & \mathbf{S^{-1}} \end{pmatrix}$$

where $\mathbf{S} = \mathbf{A_{22}} - \mathbf{A_{21}A_{11}^{-1}A_{12}}$ is the so called Schur's complement block.

Hence, together with the permutation Lemma (section 3.2.1) we arrive at the following statement:

If the block $\mathbf{A}_{1,\mathrm{N}}$ *is transfered to the block* $\mathbf{A_{22}}$ *via permutation transformation then the desired block* $\mathbf{A}^{-1}_{1,\mathrm{N}}$ *of the inverse can be obtained from the inverse* $\mathbf{S^{-1}}$ *of* $\mathbf{S}$.

3.2.3 Parallel recursive algorithm

To construct the parallel recursive algorithm for the computation of $\mathbf{A}^{-1}_{1,\mathrm{N}}$ we proceed as follows. By starting from the matrix $\mathbf{A}$ in its original block tridiagonal form, we induce a virtual additional block structure thereby distributing the domains of the scattering region to p processors as shown in Figure 3.1. This secondary level block structure, due to the scatterer's domain decomposition, consists of p large internal blocks, which in turn contain $n_1, n_2, \ldots, n_p$ blocks respectively. These blocks belong to the individual computational subspace of each processor. Additionally to these blocks, there are $p + 1$ elementary blocks which correspond to the interface slices of the decomposed domains. The position of the upper right block $\mathbf{A}^{-1}_{1,\mathrm{N}}$ that is required to be computed is indicated in Figure 3.1.

In the next step we reorder rows and columns, formally through permutation matrices, and we arrive at the reordered matrix with the structure of Figure 3.2. The reordered matrix has the 2×2 block structure,

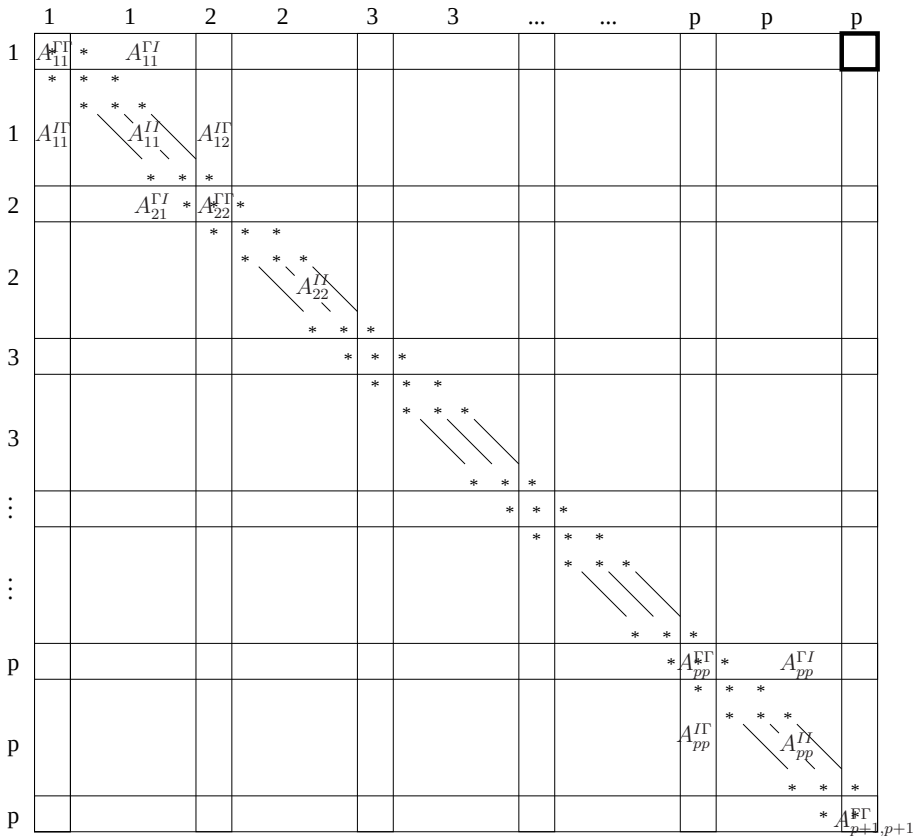

Figure 3.1: Original block tridiagonal matrix with new secondary level block structure due to processor subdivision.

$$\tilde{\mathbf{A}} = \begin{pmatrix} \mathbf{A^{II}} & \mathbf{A^{I\Gamma}} \\ \mathbf{A^{\Gamma I}} & \mathbf{A^{\Gamma\Gamma}} \end{pmatrix}$$

In this new block structure the large blocks that correspond to the internal scatterer's decomposed domains, belong to the individual computational subspace of each processor, i.e. they are decoupled between them and all of them are contained in the block labeled $\mathbf{A^{II}}$. The blocks corresponding to the interface slices are contained in the block labeled $\mathbf{A^{\Gamma\Gamma}}$. Here we should remark that the last processor is assigned to have two interface blocks, i.e. the one that links its own internal domain with the domain of the previous processor and the interface block with the left lead. The blocks that correspond to the couplings due to the kinetic energy and couple the interface slices with the p internal blocks are contained in the block labeled $\mathbf{A^{I\Gamma}}$.Due to the fact that the Hamiltonian matrix is block Hermitian then the following property is in order $\mathbf{A^{\Gamma I}} = (\mathbf{A^{I\Gamma}})^{\dagger}$. Moreover, the desired block to be computed is transfered to the upper right corner of $\mathbf{A^{\Gamma\Gamma}}$. Therefore, according to the permutation's

lemma, in order to compute $\mathbf{A}^{-\mathbf{1}}_{\mathbf{1,N}}$, it suffices to compute $\mathbf{S} = \mathbf{A}^{\mathbf{\Gamma\Gamma}} - \mathbf{A}^{\mathbf{\Gamma I}}(\mathbf{A}^{\mathbf{II}})^{-\mathbf{1}}\mathbf{A}^{\mathbf{I\Gamma}}$ at a first step and then extract the upper right block of $\mathbf{S}^{-\mathbf{1}}$. The computation of $\mathbf{S}$ results again in a block tridiagonal matrix and the algorithm can be applied recursively, i.e., by knowing $\mathbf{S}$ and applying cyclic reduction among the processors which participate in $\mathbf{S}$, we can arrive recursively at a matrix that is small enough to compute $\mathbf{A}^{-\mathbf{1}}_{\mathbf{1,N}}$ directly.

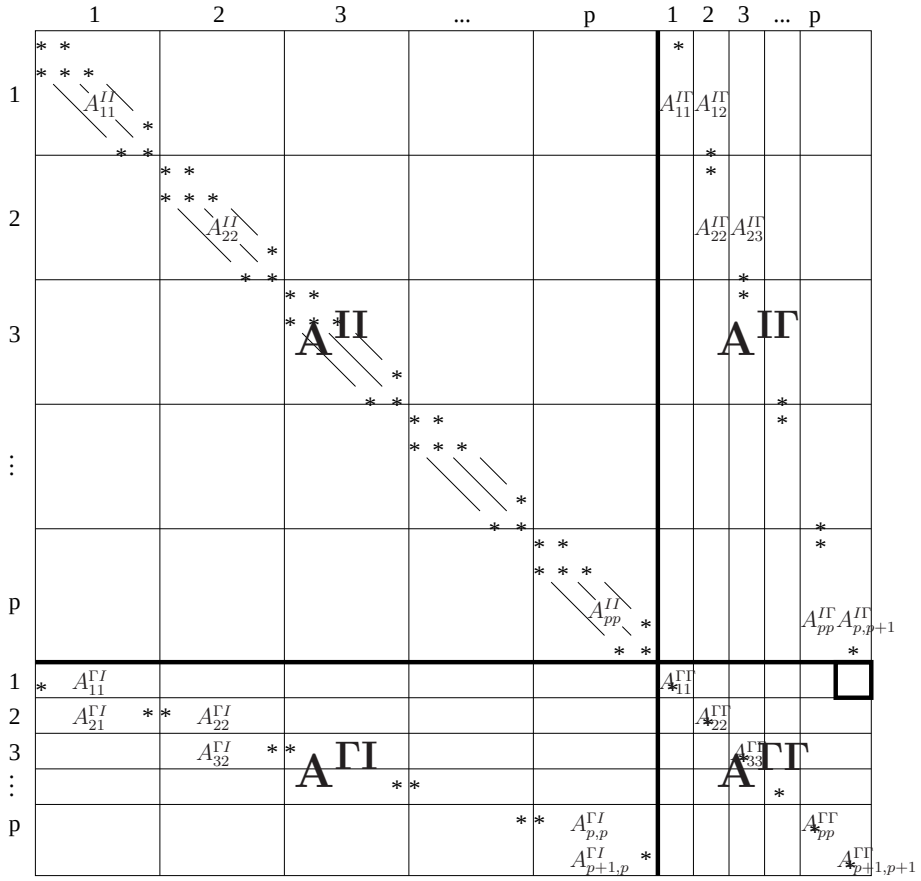

Figure 3.2: Reordered matrix $\mathbf{A}$ after row and column permutations.

Explicitly, the stages to which the parallel RGF algorithm is divided as well as the corresponding numerical complexities are the following:

1. First Stage: *Scatterer's domain decomposition and computation of* $\mathbf{S}$

   The scatterer is decomposed to internal scatterer's domains with $n_1, n_2, \ldots, n_k, \ldots, n_p$ blocks. Each domain corresponds to one of the altogether p processors participating in the computation and additionally, there are $p+1$ elementary interface blocks corresponding to the slices between the internal domains (Fig. 3.1). At this point we have to note that the last processor stores the two interface blocks $\mathbf{A}^{\mathbf{\Gamma\Gamma}}_{\mathbf{pp}}$ and $\mathbf{A}^{\mathbf{\Gamma\Gamma}}_{\mathbf{p+1,p+1}}$. Then we reorder rows and columns such that the matrix $\mathbf{A}$ has the block structure of Fig.

3.2. Subsequently, the algorithm performs a block Gaussian elimination adapted to the special sparse block structure of Fig. 3.2, i.e., it proceeds by eliminating $\mathbf{A^{\Gamma I}}$ using $\mathbf{A^{II}}$. Analytically, the steps of the block Gaussian elimination applied hereby:

$\forall$ processor k
  for ($i = 1 \ldots n_k$){
    $\mathbf{B} = (\mathbf{A^{II}_{kk}})^{-1}_{\mathbf{ii}}$
    $(\mathbf{A^{II}_{kk}})_{\mathbf{i+1,i+1}} = (\mathbf{A^{II}_{kk}})_{\mathbf{ii}} - (\mathbf{A^{II}_{kk}})^{\dagger}_{\mathbf{i,i+1}}\mathbf{B}(\mathbf{A^{II}_{kk}})_{\mathbf{i,i+1}}$
    $(\mathbf{A^{I\Gamma}_{kk}})_{\mathbf{i+1,1}} = -(\mathbf{A^{II}_{kk}})^{\dagger}_{\mathbf{i,i+1}}\mathbf{B}(\mathbf{A^{I\Gamma}_{kk}})_{\mathbf{i,1}}$
    $\mathbf{A^{\Gamma\Gamma}_{kk}} = \mathbf{A^{\Gamma\Gamma}_{kk}} - (\mathbf{A^{I\Gamma}_{kk}})^{\dagger}_{\mathbf{i,1}}\mathbf{B}(\mathbf{A^{I\Gamma}_{kk}})_{\mathbf{i,1}}$
  }
  $\mathbf{B} = (\mathbf{A^{II}_{kk}})^{-1}_{\mathbf{n_k,n_k}}$
  $\mathbf{A^{\Gamma\Gamma}_{kk}} = \mathbf{A^{\Gamma\Gamma}_{kk}} - (\mathbf{A^{I\Gamma}_{kk}})^{\dagger}_{\mathbf{n_k,1}}\mathbf{B}(\mathbf{A^{I\Gamma}_{kk}})_{\mathbf{n_k,1}}$
  $\mathbf{A^{\Gamma\Gamma}_{k,k+1}} = -(\mathbf{A^{I\Gamma}_{kk}})^{\dagger}_{\mathbf{n_k,1}}\mathbf{B}(\mathbf{A^{I\Gamma}_{k,k+1}})_{\mathbf{n_k,1}}$

The algorithm as it is formulated relies on the block Hermitian structure of $\mathbf{A}$ and can be performed fully in parallel apart from its last iteration where it requires one extra communication with its neighbouring processor. The last processor does not require such a communication because it stores additionally the block that corresponds to the last slice of the scatterer. The numerical cost for each processor scales with n_p inversions of $M \times M$ blocks and requires $6 \cdot n_p$ multiplications of matrices (see the algorithm above), i.e., $7 \cdot n_p$ operations that scale with $O(M^3)$. At this point we should remark that the number of $O(M^3)$ operations are counted in a trivial way. This naive strategy will be followed throughout this chapter because it does not consider additional computational specialities using special programming skills. To name a few examples, one could reduce the number of such operations below seven if he would consider the common multiplications between matrices that exist in the above loop, if he would use special routines that perform collectively the matrix multiplications or if one considers the fact that that all off-diagonal blocks that correspond to the kinetic energy coupling are diagonal. With respect to the storage only a few auxiliary blocks of size $M \times M$, independent of n_k, are required. Hence, each processor at the end of the first stage of the computation has stored the diagonal $\mathbf{A^{\Gamma\Gamma}_{k,k}}$ and off-diagonal $\mathbf{A^{\Gamma\Gamma}_{k,k+1}}$ block of the Schur complement. At this point we note that the notation used in the subscript of the newly computed blocks of $\mathbf{S}$ is identical to the one of the blocks of $\mathbf{A^{\Gamma\Gamma}}$ for convenience. The last processor computes, in addition to the two previously mentioned blocks, the last block $\mathbf{A^{\Gamma\Gamma}_{p+1,p+1}}$. The numerical complexity for each processor scales, in the limit of large N and M, with:

$$C_1 \approx 7 n_k M^3 \approx 7 \frac{N}{p} M^3$$

Here we have neglected the last step of the algorithm that corresponds to the single communication of each processor with its neighbouring since in the asymptotic limit it could be absorbed in n_k. After the completion of the first stage, the Schur's complement block $\mathbf{S}$ has been computed. Its blocks $\mathbf{A}^{\mathbf{\Gamma\Gamma}}_{\mathbf{k,k}}$ and $\mathbf{A}^{\mathbf{\Gamma\Gamma}}_{\mathbf{k,k+1}}$ are distributed among the processors. Again, $\mathbf{S}$ has a block tridiagonal structure and is block Hermitian:

$$\mathbf{S} = \begin{pmatrix} \mathbf{A}^{\mathbf{\Gamma\Gamma}}_{\mathbf{11}} & \mathbf{A}^{\mathbf{\Gamma\Gamma}}_{\mathbf{12}} & \mathcal{O} & \cdots & \mathcal{O} & \mathcal{O} & \mathcal{O} \\ \mathbf{A}^{\mathbf{\Gamma\Gamma}^\dagger}_{\mathbf{12}} & \mathbf{A}^{\mathbf{\Gamma\Gamma}}_{\mathbf{22}} & \mathbf{A}^{\mathbf{\Gamma\Gamma}}_{\mathbf{23}} & \cdots & \mathcal{O} & \mathcal{O} & \mathcal{O} \\ \mathcal{O} & \mathbf{A}^{\mathbf{\Gamma\Gamma}^\dagger}_{\mathbf{23}} & \mathbf{A}^{\mathbf{\Gamma\Gamma}}_{\mathbf{33}} & \cdots & \mathcal{O} & \mathcal{O} & \mathcal{O} \\ \vdots & \vdots & \vdots & \ddots & \vdots & \vdots & \vdots \\ \mathcal{O} & \mathcal{O} & \mathcal{O} & \cdots & \mathbf{A}^{\mathbf{\Gamma\Gamma}}_{\mathbf{p-1,p-1}} & \mathbf{A}^{\mathbf{\Gamma\Gamma}}_{\mathbf{p-1,p}} & \mathcal{O} \\ \mathcal{O} & \mathcal{O} & \mathcal{O} & \cdots & \mathbf{A}^{\mathbf{\Gamma\Gamma}^\dagger}_{\mathbf{p-1,p}} & \mathbf{A}^{\mathbf{\Gamma\Gamma}}_{\mathbf{p,p}} & \mathbf{A}^{\mathbf{\Gamma\Gamma}}_{\mathbf{p,p+1}} \\ \mathcal{O} & \mathcal{O} & \mathcal{O} & \cdots & \mathcal{O} & \mathbf{A}^{\mathbf{\Gamma\Gamma}^\dagger}_{\mathbf{p,p+1}} & \mathbf{A}^{\mathbf{\Gamma\Gamma}}_{\mathbf{p+1,p+1}} \end{pmatrix}$$

2. Second Stage: *Cyclic reduction of the processors participating in the Schur's complement block*

   To proceed further, we exploit the block tridiagonal structure of $\mathbf{S}$. To this end we apply a recursive technique called cyclic reduction [25]. The implementation of this technique requires successive reordering of the processors this time, in such a way that in each step the Schur's complement block is half the size as before. The first step of the cyclic reduction algorithm is shown in Fig. 3.3.

   We observe that the reordered block structure possesses again the 2×2 structure of the matrix $\tilde{\mathbf{A}}$. Therefore by eliminating the off-diagonal block using the upper-diagonal, i.e., the procedure of the first stage, we arrive at a new Schur's complement block of half the size as the preceding one. By applying this procedure recursively, after $log_2(p)$ steps we arrive at a 3×3 block matrix, of which the upper-right diagonal block of the inverse is the desired $\mathbf{A}^{-\mathbf{1}}_{\mathbf{1,N}}$ one. At this point we should remark that in each recursive step, the first and the last processor should always participate in the new resulting Schur's complement block, as shown in Fig. 3.3. This condition ensures that the desired block $\mathbf{A}^{-\mathbf{1}}_{\mathbf{1,N}}$ is always located in the upper right corner of $\mathbf{S}$. In this second stage of parallelization, each recursive step requires one inversion and four multiplications for the calculation of the diagonal $\mathbf{A}^{\mathbf{\Gamma\Gamma}}_{\mathbf{kk}}$ and the fill-in $\mathbf{A}^{\mathbf{\Gamma\Gamma}}_{\mathbf{k,k+1}}$ blocks of the resulting Schur's complement block (see algorithm of the first stage applied to the block structure of Fig. 3.3). The numerical complexity of the second stage scales as:

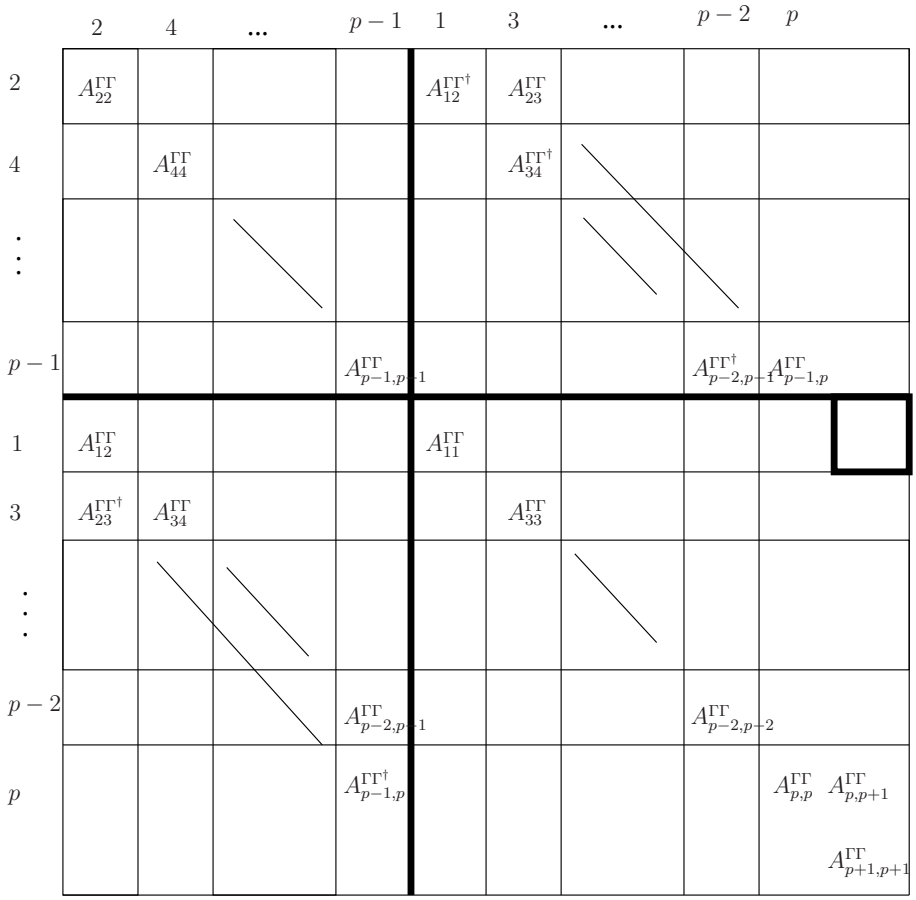

Figure 3.3: Reordering according to the cyclic reduction algorithm for a Schur's complement block of size $(p+1) \times (p+1)$. The size of $\mathbf{S}$ after the applied block Gaussian elimination is reduced to half of the preceding size.

$$C_2 \approx 5log_2(p)M^3$$

After $log_2(p)$ recursive steps operating on $\mathbf{S}$, we are left with a 3×3 block matrix of which the first row, i.e., blocks $\mathbf{C_{11}}$ and $\mathbf{C_{12}}$, are stored in the first processor and the rest two rows, i.e., blocks $\mathbf{C_{22}}$, $\mathbf{C_{23}}$ (second row) and $\mathbf{C_{33}}$ (third row), are stored in the last processor. The upper right block of the inverse of this 3×3 block matrix is the desired $\mathbf{A^{-1}_{1,N}}$ which can be computed directly.

3. Third Stage: *Computation of the transmission coefficient*

   At the last stage, there remain a few multiplications c of the blocks that are included inside the Fisher-Lee relation and are all known for the evaluation of $T(E)$. These

operations are performed sequentially by the first processor. The numerical complexity for this last stage can be evaluated as,

$$C_3 \approx cM^3$$

and since c is a small constant, in the limit of large N, C_3 can be absorbed in C_1.

The numerical complexity of the parallel algorithm scales as:

$$C_{\rm par}(N, M, p) \approx C_1 + C_2 + C_3 \approx 7\frac{N}{p}M^3 + 5log_2(p)M^3 \tag{3.1}$$

and the corresponding sequential ($p = 1$) one, as:

$$C_{\rm seq}(N, M) \approx 7NM^3$$

We should remark that the algorithm developed here holds equally for scattering regions with complex boundary conditions, i.e., blocks $\mathbf{A_{ij}}$ with varying sizes, and can be generalized to the geometry of $3D$ scatterers in a straightforward manner. We further remark that one could reduce the number of numerical operations that scale with M^3 at the first stage, however for the purposes of the present analysis that serves as a tool to identify the sources of computational cost this is not unique and therefore not necessary.

3.3 Numerical benchmarks

3.3.1 Metrics for the analysis of performance and scalability

In this section an analysis of the performance and scalability for two specific numerical benchmarks will be pursued. This is required in order to test the models for the numerical complexity we derived so far and to demonstrate a measure for the capabilities and optimized use of the proposed algorithm. To proceed with such an analysis it is necessary to define some characteristic quantities for our parallel algorithm following Ref. [26]. Firstly, we define the problem size:

$$W(N, M) = 7NM^3$$

which is the number of numerical operations in the sequential algorithm ($p = 1$), i.e., the RGF approach, and is also equal to the serial run time T_s if a unit of time corresponds to each numerical operation. The cost of simulating the parallel algorithm on a single processor is:

$$pT_p(N,M,p) = pC_{\rm par}(N,M,p) = 7NM^3 + 5\,p\,log_2(p)M^3$$

where T_p is the parallel run time corresponding to $C_{\rm par}(N,M,P)$ if we assume a unit of time for each computational step. The overhead function T_0 of the parallel algorithm is defined as:

$$T_0(M,p) = pT_p - W = 5\,p\,log_2(p)M^3$$

and determines the part of its cost that is collectively spent by all processors compared to the sequential algorithm. The sources of overhead of a parallel system can be in general attributed to interprocessor communication, load imbalance and extra computational time due to a part of the program that is not parallelizable. In our algorithm the dominant contribution to the overhead results from the amount of operations during the cyclic elimination of the processors. The extra computational time required for the evaluation of the Fisher-Lee relation (this is the only not parallelizable part) can be neglected in the limit of large N. As far as load imbalance is concerned, the two numerical benchmarks to be investigated will show a different significance of this source of overhead. Finally, we define the efficiency of the parallel algorithm as:

$$F = \frac{W}{pT_p} = \frac{7NM^3}{p\left(7\frac{N}{p}M^3 + 5\,log_2(p)M^3\right)} = \frac{1}{1+\frac{5\,p\,log_2(p)}{7N}} \tag{3.2}$$

From this relation, we conclude that the efficiency is independent of the size of blocks M and depends only on the longitudinal length of the scatterer N and the number of processors p participating in the computation. Moreover, by scaling appropriately N with p, it is possible to maintain the efficiency fixed, a property met in scalable parallel algorithms. From Eq. (3.2) we can define the isoefficiency function:

$$W = KT_0$$

where $K = F/(1-F)$ is given for a specific F. For fixed K we can arrive at the following relation for N and K:

$$N = \frac{5}{7}Kp\,log_2(p) \tag{3.3}$$

Therefore, our algorithm can be cost-optimal if we choose $N = \frac{5}{7}Kp\,log_2(p)$ and scalable if we increase N with rate $O(p\,log_2(p))$. On the other hand, for a fixed size problem,

i.e., keeping N and M fixed, we observe that the efficiency decreases with increasing p as a consequence of Amdahl's law (see Eq. (3.2)). Here some final remarks are in order. In the quantities defined so far, we have assumed lattices of unique size $N \times M$ for the discretization of the scattering regions (perfectly load balanced problems). In addition, the time spent for the interprocessor communications due to message passing is neglected. This is due to the increased granularity of the block tridiagonal system, resulting in a better efficiency of the parallel algorithm. Finally, our numerical procedure is validated with results obtained independently by the numerical code TIMES (Transport In Mesoscopic Systems) used e.g. in recent studies of normal-superconducting hybrid systems [27].

3.3.2 Billiard in a magnetic field

The first numerical benchmark to test the performance of our algorithm is a rectangular billiard in a homogeneous magnetic field. Modified billiards provide a class of systems for testing the correspondence between quantum and classical transport. The magnetic field is included with the Peierl's substitution and is present only in the billiard, so that we end up with a perfectly load balanced problem with respect to the numerical work loaded to each processor. This system represents therefore an excellent example for testing the models of complexity developed in subsection 3.3.1. For the purpose of the current investigation we avoid, therefore, to use leads as an intermediate step for the application of the magnetic field [28, 29], since this would lead to a load imbalanced system. Figure 3.4 shows the setup.

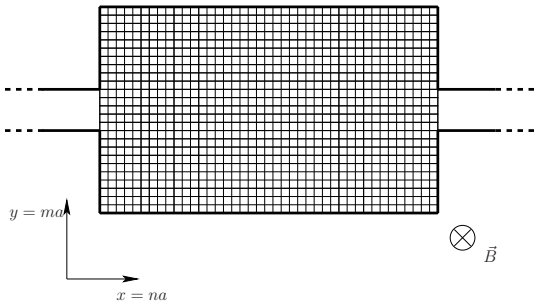

Figure 3.4: Setup of a rectangular billiard attached to two reservoirs with $n = 0, 1, \ldots, N-1$ slices of $m = 0, 1, \ldots, M-1$ sites each, used in the fixed-size efficiency calculations. The ratio of the two dimensions is $\frac{N}{M} = \frac{8}{5}$.

The first setup to test the performance of our algorithm uses a 400×250 lattice for the discretization of the billiard (ten times resolved compared to the one of Figure 3.4). The first type of analysis consists of keeping the lattice fixed and studying how the efficiency of the problem scales with increasing the number of processors. We remind the reader that the total cost of the parallel algorithm is dominated by the cost for the evaluation of the Schur's complement block and the cost due to the cyclic reduction of the processors (see Eq. (3.1)).

Table 3.1 shows the times measured for the evaluation of $T(E, B)$ at a fixed energy E and magnetic field B.

Table 3.1: Measured time (Time) and efficiency (F) as a function of the number p of the processors for a rectangular billiard in a magnetic field with fixed size $N = 400$ and $M = 250$.

p	Time (sec)	$\_F\_$	p	Time (sec)	$\_F\_$	p	Time (sec)	$\_F\_$
1	1723.58	1.0	14	136.82	0.9	48	53.78	0.668
2	871.94	0.989	16	120.09	0.897	56	49.31	0.624
4	444.75	0.969	20	99.84	0.863	64	45.33	0.594
6	300.57	0.956	24	86.57	0.83	80	39.68	0.543
8	229.18	0.94	28	77.58	0.793	96	38.49	0.466
10	185.61	0.928	32	69.51	0.775	112	35.16	0.438
12	158.46	0.906	40	59.11	0.729	128	34.27	0.393

At this point we note that the system used for the time measurements has been a Linux cluster of 256 nodes with Dual AMD Athlon 1.4 GHz processors of 2 GB RAM each [30]. Efficiency is 1.0 for $p = 1$ and gradually decreases with p due to the fact that with increasing p, the term in equation (3.1) proportional to $log_2(p)$, i.e. attributed to interprocessor communication, dominates with respect to the other term that decreases with $\frac{N}{p}$, thereby decreasing the efficiency of the proposed algorithm.

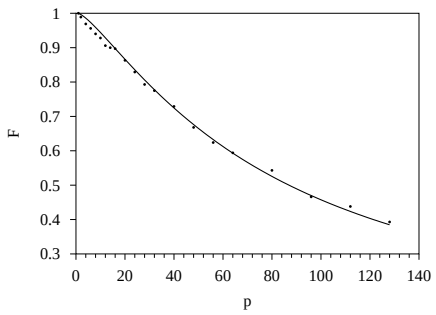

Figure 3.5: Efficiency F as a function of the number p of processors. The dots correspond to the measured efficiency and the solid curve to the theoretical model employed.

Figure 3.5 shows the efficiency F as a function of the number p of processors according to the performed time measurements (dots) compared to the analytical curve of Eq. (3.2). We observe that the agreement between the theoretical model and the measurements is very good. Therefore, we conclude that the dominant sources of numerical load have been succesfully identified and weighted. Further sources of overhead, such as the time required for interprocessors' communication, could be neglected as the work load is dominated by the

amount of numerical operations that scale with M^3, i.e., multiplications and inversions of $M \times M$ blocks.

The next step in our analysis is to perform a size scaling experiment. The aim of this test, is to scale the size of the problem such that the efficiency is kept fixed. As we saw from Eq. (3.2) the efficiency is independent of the size of the transversal dimension M and depends only on the size of the longitudinal dimension N and the number of processors p. Therefore, by scaling appropriately N with p it is possible to arrive at a fixed efficiency F of the algorithm. According to equation (3.3) for $p = 2$ processors the efficiency can be 0.848 if we choose $N = 8$. If we keep increasing the number of processors p and the size of the system N, keeping M fixed, according to the relation:

$$N' = N\frac{p' log_2(p')}{p log_2(p)}$$

where N' and p' are the new size of the system and the new number of processors respectively, then we expect that the efficiency will stabilize around 84.8%. Table 3.2 shows the efficiency for the scaled size problem.

Table 3.2: Efficiency (F) as we increase the longitudinal dimension N of the billiard with the number of the processors p according to $N = O(p log_2(p))$. We keep $M = 100$ fixed.

$N; p$	T_s (sec)	T_p (sec)	F
$8; 2$	1.1	0.68	0.816
$32; 4$	4.76	1.44	0.826
$96; 8$	14.27	2.17	0.822
$256; 16$	38.32	2.82	0.849
$640; 32$	95.25	3.54	0.841
$1536; 64$	228.79	4.27	0.837
$3584; 128$	534.06	5.04	0.828
$8192; 256$	1222.07	5.82	0.82

We observe that the efficiency is stabilized between 0.81 and 0.85 thereby confirming our prediction. The sources of these slight deviations could be attributed to some enhanced contributions of time spent in interprocessor communications. Therefore our models provide a reliable source for the estimation of the computational cost. Table 3.2 shows that the larger the size of the system N, the larger becomes the efficiency. Therefore, our parallel algorithm is suitable for large systems, in particular of enhanced longitudinal dimension. Scattering problems with complex structures could be disentangled into modules with arbitrary complexity, of which the computation could be done efficiently by one processor. Cyclic

reduction among the processors would join the information of the individual modules. If the computational complexity of a module is particularly enhanced for one processor, then more processors could be employed.

3.3.3 Sinai billiard

The second numerical benchmark corresponds to a category of scatterers with enhanced complexity. It consists of a Sinai billiard. This setup has been chosen for simulations in Ref. [31]. The numerical challenge imposed hereby is the exact reproduction of the antidot's circular shape in the continuum limit.

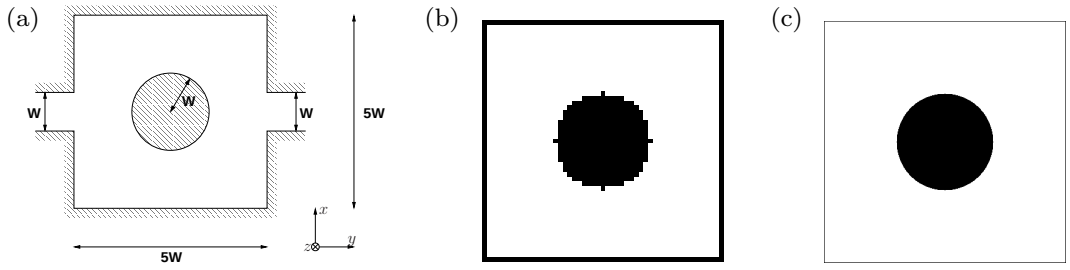

Figure 3.6: (a) Open scattering geometry of a Sinai billiard. Subfigure (b) shows the isolated scatterer on a 49×49 grid of points and width $W = 10a$. Subfigure (c) shows the same setup but four times resolved. The thickness of the border lines in (b) and (c) provide a measure of the lattice constant.

Figure 3.6 shows the discussed geometry. Subfigure 3.6-(a) shows the open geometry and dimensions of the Sinai billiard, while in 3.6-(b) the isolated Sinai billiard is discretized on a 49×49 grid of points. On such a small grid the antidot has, on the scale of Fig. 3.6-(b), the shape appearance of a polygon. Subfigure 3.6-(c) shows the same setup of the Sinai billiard but on a grid which is four times resolved compared to 3.6-(b), i.e., a 399×399 grid. The latter is going to be our fixed input size for the time measurements as we increase p. At this point we remark that the antidot has hard wall boundaries, i.e., the sites which form the antidot are excluded from the computation, thereby leading to blocks $\mathbf{A_{ij}}$ with varying dimensions. Table 3.3 shows the efficiency measured for the evaluation of $T(E)$ at a fixed energy E as a function of p.

Table 3.3: Measured time (Time) and efficiency (F) as a function of the number p of the processors for a Sinai billiard. The lattice $N = 399$ and $M = 399$ is kept fixed.

p	Time (sec)	$\_F\_$	p	Time (sec)	$\_F\_$	p	Time (sec)	$\_F\_$
1	13490.83	1.0	14	1201.49	0.802	48	417.8	0.673
2	6791.23	0.993	16	1058.31	0.797	56	379.9	0.634
4	3917.2	0.861	20	855.45	0.789	64	343.87	0.613
6	2689.56	0.836	24	734.14	0.766	80	271.07	0.622
8	1974.65	0.854	28	655.5	0.735	96	267.04	0.526
10	1649.51	0.818	32	571.54	0.738	112	226.92	0.531
12	1404.99	0.800	40	462.83	0.729	128	224.37	0.47

The efficiency decreases with increasing p as expected. We should note that for these measurements equidistant domains, with respect to the longitudinal dimension, have been distributed among the processors. However, due to the antidot's boundaries, it becomes clear that this kind of distribution leads to an inevitable load imbalance. The domains that include sections of the antidot are described by blocks of smaller size compared to the ones that are kept aside the antidot, resulting thereby in reduced computational load for the corresponding processors. For $p = 2$, we observe an efficiency very close to 100%. This is a result of the symmetry of the geometry of the setup, which results in a load balanced problem for this specific number of processors. If we further increase p then the efficiency falls abruptly. This result is attributed to the intensive load imbalance for few number of processors. To remedy this problem we have to choose a non-uniform domain decomposition of the scattering region, leading, thereby, to a more fair work load for all processors. For a larger number p, however, this problem becomes much less intense, since the total cost is multiply distributed in fairly small pieces of numerical load and the inequality among the processors, with respect to the load they share, significantly reduces. Therefore, for rather large p, load imbalance is not a significant source of parallel overhead, however, deviations compared to a load balanced setup are still evident (see below).

To analytically estimate the efficiency of the parallel algorithm for the setup in discussion, it is necessary to take into account the circular shape of the antidot. For this purpose, we divide the scatterer in two sections. One section of which the numerical cost scales with $N_1 \times M^3$ arithmetic operations, where N_1 the number of slices outside the antidot, and a second one of which its computational load scales with $\sum_{i=1}^{N_2} M_i^3$ where M_i is the varying size of the blocks of each of the N_2 slices that compose the antidot. Therefore, the size of the scattering problem is:

$$W(N,M) = 7N_1M^3 + 7\sum_{i=1}^{N_2} M_i^3$$

Moreover, we assume that at the first stage of parallelization, the work W is distributed uniformly among the processors and that at the second stage the processors that participate in the cyclic reduction are weighted appropriately, with respect to the load that corresponds to them. This is translated to the fact that $\frac{2}{5}p$ processors possess a work load that scales with $\sum_{i=1}^{N_2} M_i^3$ and $\frac{3}{5}p$ processors possess a work load that scales with M^3. Therefore, the cost for the parallel algorithm will be:

$$pT_p = 7N_1M^3 + 7\sum_{i=1}^{N_2} M_i^3 + 3plog_2(\frac{3p}{5})M^3 + 2plog_2(\frac{2p}{5})\sum_{i=1}^{N_2} M_i^3$$

The efficiency, which is no longer independent of the size of the transversal dimension M, will be:

$$F = \frac{W}{pT_p} = \frac{N_1M^3 + \sum_{i=1}^{N_2} M_i^3}{N_1M^3 + \sum_{i=1}^{N_2} M_i^3 + \frac{3}{7}p\,log_2(\frac{3p}{5})M^3 + \frac{2}{7}p\,log_2(\frac{2p}{5})\sum_{i=1}^{N_2} M_i^3} \tag{3.4}$$

Figure 3.7 shows the measured efficiency (dots) as a function of p. We observe a rather abrupt decrease of F for a small number of processors $p < 10$ which smoothens for larger p. The solid curve of Figure 3.7 represents the analytical model of Eq. (3.4), calculated for the 399×399 grid of subfigure (3.6)-c.

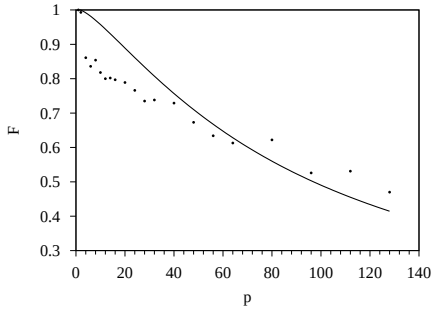

Figure 3.7: Efficiency F as a funtion of the number p of processors. The dots correspond to the measured efficiency and the solid curve to the theoretical model derived to take into account the special geometry of the setup.

The agreement with the measurements is quite well, however, deviations for $p > 2$ are evident. For $p = 2$ the prediction agrees due to the symmetric load share between the two processors for this problem. For $p > 2$, deviations are apparent due to the assumptions within the derivation of our model. Namely, neither does W distribute itself evenly among the processors (load imbalance) nor is the computational load due to the cyclic reduction weighted exactly among the processors, as we assumed. To remove the first assumption one should proceed to an uneven domain decomposition with respect to the processors, which would vary depending on p. We conclude thereby, that in a scattering problem of complex geometry, the strategy to be followed in order to optimize the efficiency of the algorithm, regarding the load that the processors share, should take into account the particular geometric features of the scatterer.

3.4 Conclusions

A parallel algorithm for the implementation of the RGF method has been presented. The algorithm calculates the transmission coefficient through a mesoscopic scattering sample for a certain value of the energy or some other external parameters such as a magnetic field. The algorithm is suited to treat complex scattering problems that cannot be handled by a single processor on an affordable time scale. We emphasize that the algorithm goes beyond the straightforward parallelization with respect to external parameters of the problem such as e.g. Fermi energy or magnetic field strenth, which is much more efficient when treating problems of smaller size. For intermediate size problems, a parallelization of the total problem with respect to the external parameters in combination with the current proposed scheme, taking into account its limitations, should be also considered. The structure of the algorithm is mainly based on an initial domain decomposition of the scattering region due to processors' subdivision and recursive computation of the Schur's complement block through cyclic elimination of the processors. The computational cost due to the longitudinal dimension of the scattering region scales linearly with p. However, the cost due to the cyclic elimination, prevents us from achieving an efficiency of 100%. To demonstrate the efficiency of the parallel RGF algorithm, we proceeded with an analysis of the performance, scalability and sources of overhead for two specific numerical benchmarks. The first numerical benchmark corresponds to a perfectly load balanced setup, such as a rectangular billiard in a magnetic field, and the derived model is in very good agreement with the measurements. The efficiency for a small number of processors is close to 100 % and increases as we increase the size of the problem while keeping the number of processors fixed. The second numerical example contained an additional geometrical challenge, being the exact reproduction of the circular shape of an antidot with hard wall boundaries in a Sinai billiard. The computation hereby required manipulation of blocks with varying sizes leading to a nonuniform numerical load for the processors participating in the computation. A model adapted to the special geometry of this problem has been employed, which exhibited its geometric peculiarities

and indicated the additional source of overhead due to load imbalance. The latter is responsible for the drastic decrease of efficiency even for a small number of processors and can be remedied by a selection of non-uniform decomposed domains distributed to the processors, based on the numerical cost. From our analysis it became apparent that the parallel RGF technique developed here, is particularly suitable for modular scattering structures of high complexity. Parallelization in this context gives the freedom to decompose the scatterer into modules, the computation of each can be efficiently performed by one processor. The optimized distribution of modules to processors depends on their individual complexity. In case their complexity is enhanced, more than one processors could be employed and the corresponding computational load should be shared according to the individual features of the module.

Chapter 4

Quantum magnetotransport through open linear quantum-dot crystals

4.1 Introduction

Single quantum dots are the solid state analogue of an atom whereas the properties of coupled-dots may resemble that of molecules. Arrays of coupled-dots may be considered as one-dimensional artificial crystals with the dot as repeating unit acting as the lattice basis. If the coupling between the single quantum dots is strong enough, the electronic structure uncovers many similarities with the subbands of quasi one-dimensional systems with a much reduced reciprocal lattice vector in comparison to the one of the semiconductor crystal. It is also well known that a uniform magnetic field applied to Bloch electrons yields magnetic subbands with an overall different spectrum [32, 33]. Unlike the lack of any impact in one dimension, in two dimensions these form the famous Hofstadter butterfly [34]. The question to which extent there exists an observable magnetic effect for the intermediate dimensionality, as in the case of an array of open quantum dots, remains open. Moreover, experimental evidence in the literature is scarce [35, 36] and the effect of magnetic subbands is hard to isolate in the common setup of lateral semiconductor superlattices [37]. Hence, the prospect of measuring its properties in a simple fashion is quite attractive.

In this chapter we consider small coupled-dot arrays that present distinct spectral properties regulated via an applied magnetic field B. The electronic transport exhibits bright and dark windows reflecting an electronic structure that is reminiscent of the energy bands of the corresponding linear artificial crystal. This unique feature allows to explore the B-dependence of the subbands of the quasi one-dimensional Bloch electrons. With varying magnetic field, our calculations demonstrate qualitative (and quantitative) changes of the bright and dark transport windows in the suggested array structure, thus, yielding a direct signature of the magnetic subband formation in the magnetoconductance.

Coupled-dot arrays may also be used as elements in magnetoresistive devices. For example, by manipulating Fano (anti)resonances single open quantum dots could form such

building blocks or, as recently suggested, be applied as spin filters [38]. The array structure allows the formation of wide band gaps. This enables magnetically controlled current flow to change up to few orders of magnitude even at elevated temperatures despite thermal broadening; an additional advantage is the fine tuning allowed by the coupling parameters possibly using back gates. Such a design of chaotic and rectangular quantum dots in alignment has been recently realized with a split-gate technique [39,40]. In the experiments of Ref. [40] the classical dynamics of the electrons in a magnetic field triggers reflection giving rise to a large magnetoresistance at a field slightly greater than the magnetic field B_c that corresponds to an electron cyclotron radius equal to the size W of the dot, i.e., $B_c = \hbar k_F/eW$ (k_F is the Fermi wavevector). However, we show that the quantum mechanical effect of magnetic subband structure also gives significant magnetoresistance at more moderate fields.

Furthermore, the coupling between the dots plays a significant role in the formation of the energy bands and subsequently to the transmission mechanism. In this regard results for several geometries, corresponding to various coupling regimes, will be exhibited and useful conclusions on the robustness of current flow with respect to large temperatures will be extracted. Further possibilities to improve the efficiency of the current flow will be shown for various parameters of the materials such as electron densities and effective masses.

The chapter is organized as follows. In section 4.2 we will discuss the geometry of the setup and the working Hamiltonian in the tight-binding representation. We further present the results and interpret them in terms of several material parameters. The physics for different coupling regimes and geometries of the quantum dots are discussed in the corresponding subsections. Section 4.3 contains a presentation of the effects of decoherence and spin Zeeman splitting. Finally, in section 4.4 we summarize our conclusions.

4.2 Linear response magnetotransport in coupled-dot arrays

4.2.1 Discussion of the setup and the results

Fig. 4.1(a) shows the setup in discussion. We assume that square quantum dots of size W are laterally confined near the surface of a semiconductor heterostructure by an electrostatic field which creates effective hard wall boundaries for ballistically propagating electrons whereas the coupled leads are modeled as discussed in chapter 2. The point contacts bridging the dots have square geometry of dimensions $L_b = D = 0.3W$ that are of the order of the Fermi wavelength $\lambda_F = 2\pi/k_F$. Although quantitative details differ, our main conclusions are independent of this simplest design.

We model the electronic structure via a single-band effective mass equation of electrons in a magnetic field, which when discretized on a lattice, is most easily expressed in the notation of second quantization

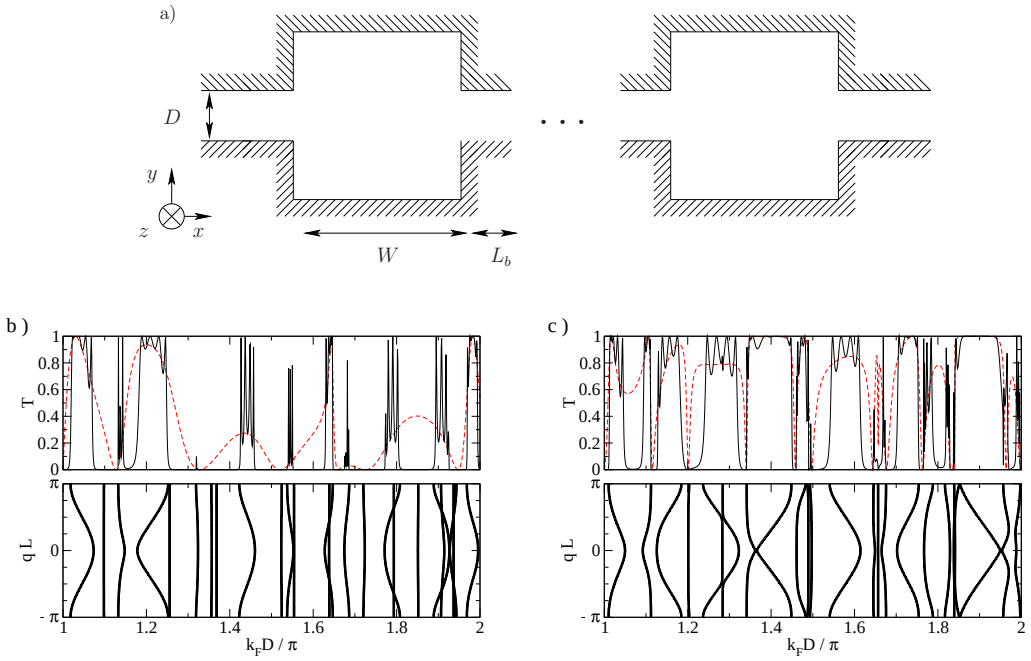

Figure 4.1: (a) Schematic representation of the discussed open array of quantum dots. (b) Upper panel: field-free quantum transmission through a single-dot (dashed curve) and the five-dot array of (a). Lower panel: energy spectrum of the corresponding one-dimensional artificial crystal with lattice spacing $L = W + L_b$. Note that flat energy bands do not contribute to transport since electrons acquire zero group velocity. (c) Same as (b) for a magnetic flux $\Phi \approx 4.5\phi_0$ piercing the unit cell. We recall that the integer part of $k_F D/\pi$ indicates the number of propagating channels in the leads and q defines the Bloch vector of the periodic structure.

$$H(\mathbf{r}) = \sum_{\mathbf{r}} \epsilon_{\mathbf{r}} c^{\dagger}_{\mathbf{r}} c_{\mathbf{r}} + \sum_{\mathbf{r},\mathbf{\Delta r}} (V e^{2\pi i \frac{\mathbf{A}(\mathbf{r})\mathbf{\Delta r}}{\phi_0}} c^{\dagger}_{\mathbf{r}} c_{\mathbf{r}+\mathbf{\Delta r}} + h.c.). \tag{4.1}$$

Here, $\mathbf{\Delta r}$ indicates the vector of the position of the nearest neighbors to the site $\mathbf{r}$ and $\epsilon_{\mathbf{r}} = 4V$ is the on-site energy, with $V = \hbar^2/2m^*a^2$ being the hopping matrix element; m^* is the effective mass (fixed to $0.05m_0$ unless otherwise stated; with m_0 being the bare electron mass) and a is the lattice mesh constant of the tight-binding grid. The magnetic field $\mathbf{B} = B\mathbf{z}$ applied to the dot array is introduced via the vector potential $\mathbf{A}$ in the Peierls phase factor; $\phi_0 = h/e$ is the flux quantum. Charge transport properties are calculated within the Landauer scattering-matrix formalism (see chapter 2) which expresses the current via eq. (2.3),

$$I = \frac{2e}{h} \int_{-\infty}^{\infty} \mathrm{T}(E)(f_L(E) - f_R(E))dE$$

in which the factor two accounts for spin degeneracy. We calculate T using the parallel recursive Green's functions method developed in chapter 3. As the system size increases one needs to invert a block-tridiagonal matrix which scales linearly with the array length. For serial processing this yields an additional cost that we avoid by distributing the scatterer's domain over several processors.

The upper panels of Figs. 4.1(b) and 4.1(c) show the field-free and $B \neq 0$, respectively, quantum transmission in the first open channel. Transport through a five-dot array is indicated by the solid curves. In contrast to the single-dot transmission spectrum - plotted in dashed line - bright and dark windows are formed in which transport is either allowed or suppressed. These compare well to the energy bands and gaps of the electronic structure of the corresponding infinite linear artificial lattice, which are shown for zero and finite B in the lower panels of Figs. 4.1(b) and 4.1(c), respectively. Also evident in those figures is the strong dependence of the band structure on the magnetic flux piercing the unit cell. Broad energy bands contribute electron states that are almost fully transmitted, whereas narrow sections exhibit weaker transmission signals. The remarkable characteristic is that such a transmission spectrum is already obtained for a quantum dot array with just a few unit cells as can be seen from the comparison of the upper and lower panels of Figs. 4.1(b) and 4.1(c). In practice, this facilitates the realization of such a device at length scales comparable to the electronic phase coherence length at finite temperatures so that the features of the transmission spectrum do not wash out due to phase breaking processes. The fast convergence of the transmission with increasing array length has previously been observed in investigations of the conductance of oligomer-based molecular junctions [41]. Here, however, in a trade-off with the typical linear dimension of the device it is possible to apply moderate magnetic fields in order to manipulate the electric response; for the same magnetic flux Φ through the dot, the larger W is, the smaller the magnetic field needs to be since $\Phi = BW^2$.

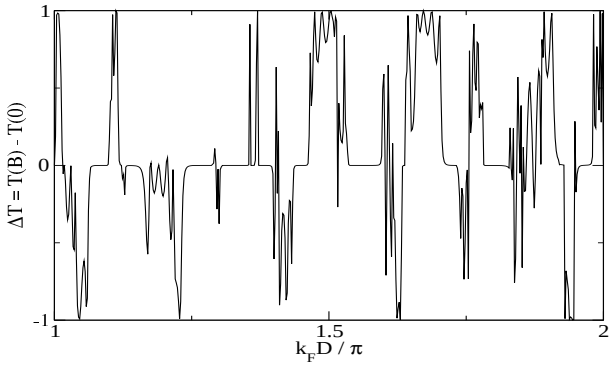

Figure 4.2: Magnetically controlled flow demonstrated via the profile of the difference of the quantum transmission for the field-free and $B = 0.3B_c$ cases.

In Fig. 4.2, we plot the transmission function difference between the field-free structure and that at a field of strength $\xi = B/B_c = 0.3$. The positive and negative parts reflect

the newly formed magnetic subband structure of Bloch electrons in the corresponding one-dimensional artificial crystal which causes the bright and dark transport windows to occur at different spectral positions. As discussed later, for a given geometry and Fermi energy (i.e., fixed $k_F D/\pi$) the contrast in current flow due the differing transmission spectra can also be traced as a function of magnetic field to yield the evolution of the magnetic subbands. We note that there exist broad energy ranges over which bright transport windows at non-zero magnetic field overlap with dark areas at vanishing B, e.g., at $k_F D/\pi \approx 1.5$ and $k_F D/\pi \approx 1.67$. This feature marks a mechanism for magnetically controlled current flow which can be realized at liquid nitrogen temperatures and above as shown below.

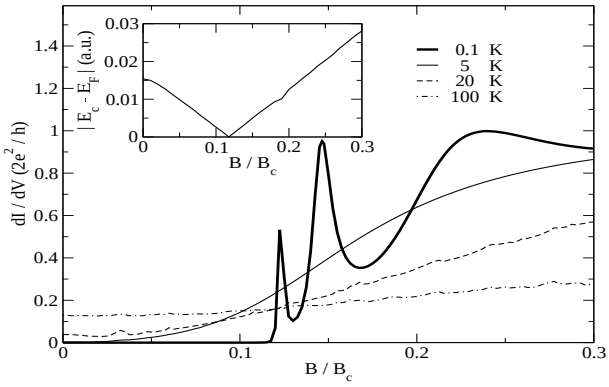

Figure 4.3: Linear-response magnetoconductance at various temperatures ($k_F D/\pi \approx 1.5$). Inset: magnetic field dependence of the distance between the Fermi energy $E_F = 74.5$meV and the band edge E_c accounting for the resonant structure of the low-temperature magnetoconductance when crossing occurs at $B \approx 0.12 B_c \approx 0.45$T.

At this point it is instructive to interpret the system of natural units to SI units. Assuming $\lambda_F = 30$nm with $m^* = 0.05 m_0$ yields $E_F = 33$meV and $B_c = 1.68$T. Regarding dimensions each quantum dot should be $W \approx 75$nm wide and the width of the lead $D \approx 22$nm at $k_F D/\pi \approx 1.5$. The lattice spacing L is around 100nm defining a total array length of less than 500nm for five coupled-dots. In a strict sense, these dimensions define the range of validity of our results regarding temperature. Apart from the thermal broadening, the temperature controls the scattering mechanisms determining the electronic phase coherence length. Since, so far, we have assumed that electrons are propagating coherently, the array length must be shorter than the latter. More examples are presented in Table 4.1. These show the interplay between linear dimensions and B_c.

In Fig. 4.3, we furnish our observations with the linear-response magnetoconductance curve at various temperatures. An overall increase of the conductance with increasing magnetic field strength is clearly observed. A remarkable feature is the fine peak-structure of the magnetoconductance dI/dV at very low temperatures which is a consequence of the formation of the spectrum of Bloch electrons in a magnetic field. This is demonstrated in the inset of Fig. 4.3. As the band structure modifies with the magnetic field, the edge of a single band

Table 4.1: SI units at $k_F D/\pi = 1.5$ assuming $m^* = 0.05m_0$.

λ_F(nm)	W(nm)	E_F(meV)	B_c(T)
20	50	74.5	3.78
30	74	33	1.68
50	123	11.9	0.6

E_c crosses the Fermi energy E_F at $B/B_c \approx 0.12$. When the distance $|E_c - E_F|$ vanishes a bright transport window is induced that gives rise to the resonant structure of dI/dV in the sub-Kelvin regime (thick line in Fig. 4.3). Due to the well-pronounced peaks one could think of using these as a probe for the magnetic subband structure. At higher temperatures thermal broadening causes averaging over a larger part of the spectrum including many adjacent minibands and gaps. This increases the low-field conductance whereas simultaneously decreases the corresponding higher field values.

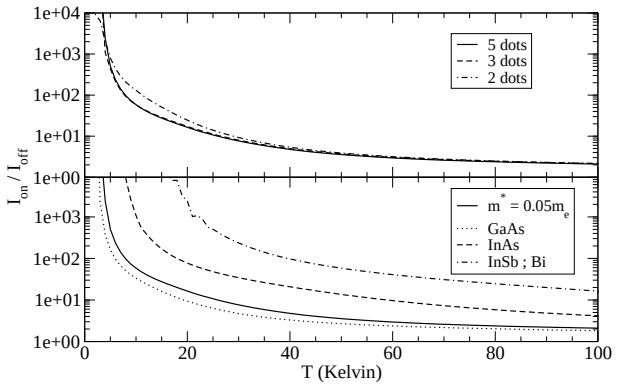

Figure 4.4: (Upper panel) Ratio I_{on}/I_{off} of the current flow in the on ($B = 0.3B_c \approx 1.13$T) and off ($B = 0$) state as a function of temperature for an array of $N = 2, 3, 5$ coupled-dots. (Lower panel) Temperature dependence of the I_{on}/I_{off} ratio for various materials parameterized by m^*. $k_F D/\pi$ and E_F are the same as in Fig. 4.3.

A significant quantity in our design is the enhancement (on) - suppression (off) ratio of current flow I_{on}/I_{off} in the linear response regime. In what follows, we analyze its typical behavior heading towards finite temperatures for various materials parameterized via the effective mass by fixing $k_F D/\pi \approx 1.5$. In the upper panel of Fig. 4.4, the temperature dependence of the I_{on}/I_{off} ratio is shown for an array with varying number N of coupled-dots. Remarkably enough the results hardly modify with $N \gtrsim 3$ in support of our previous remarks. We observe that relatively large ratios in excess of 100 can be achieved for temperatures up to ~ 10K and can be preserved to $I_{on}/I_{off} > 10$ for temperatures up to ~ 26K. Further temperature increase makes the ratio to decay smoothly to $I_{on}/I_{off} = 2$ at room temperature. Note that this behavior may be drastically improved with a selective choice

of materials and geometry. A search in the parameter space for the latter is presented in the following subsections. Rather, in the lower panel of Fig. 4.4 we show how the effective mass of common materials can be readily used in order to considerably improve the device operation since I_{on}/I_{off} ratios magnify at all temperatures as m^* decreases. Notably, for $m^* = 0.01m_0$ (InSb;Bi), $I_{on}/I_{off} > 100$ can be obtained up to ~ 50K and rather enhanced $I_{on}/I_{off} > 10$ can be preserved for temperatures up to ~ 100K.

So far we have presented an investigation of ballistic transport through a finite array of coupled-dots from the perspective of a quantum mechanical magnetically tunable mechanism that redefines bright and dark transport windows. The latter have been respectively identified as the energy bands and gaps of the electronic structure of the corresponding one-dimensional artificial crystal despite the small number of dots. Thus, by tracing their magnetic field dependence we showed that the precursor of magnetic subband formation in the energy spectrum can be readily observed. The broad energy range of the transport windows also reveals a well defined mechanism that yields magnetically controlled currents with large enhancement - suppression ratios which can extend up to several tens of Kelvin depending on material parameters. With present technology such a device can be realized within a region of ~ 300 nm at a magnetic field of ~ 0.5T.

In the following let us discuss the role of the geometry of the building blocks of the array, i.e. the quantum dots and the bridging leads based on our intuition and verified by numerical results. Firstly, we will concentrate on the role of the coupling strength between the quantum dot as it is induced by the geometry of the coupling media. Thus, in the following sections we will show numerical results for the strong and weak coupling regime as it is defined by the width of the coupling leads. After the discussion of the geometry of the bridging leads we will show some results concerning rectangular dots.

4.2.2 Strong coupling regime

We remind the reader that the underlying mechanism that induces quantum transport through quantum-dot arrays is their artificial energy bandstructure. We have observed that broader energy bands correspond to a transmission mechanism with robust and strong signals in comparison to thin energy bands which induce a rather weak transmission of electronic signals. In the light of these observations, one would suggest that the optimal coupling between the quantum dots would be the strongest possible since broad energy bands would allow for transparent transmission signals. Let us simulate such a scenario by increasing the fraction of the leads' width D over the side of the dot to $D = 0.5W$.

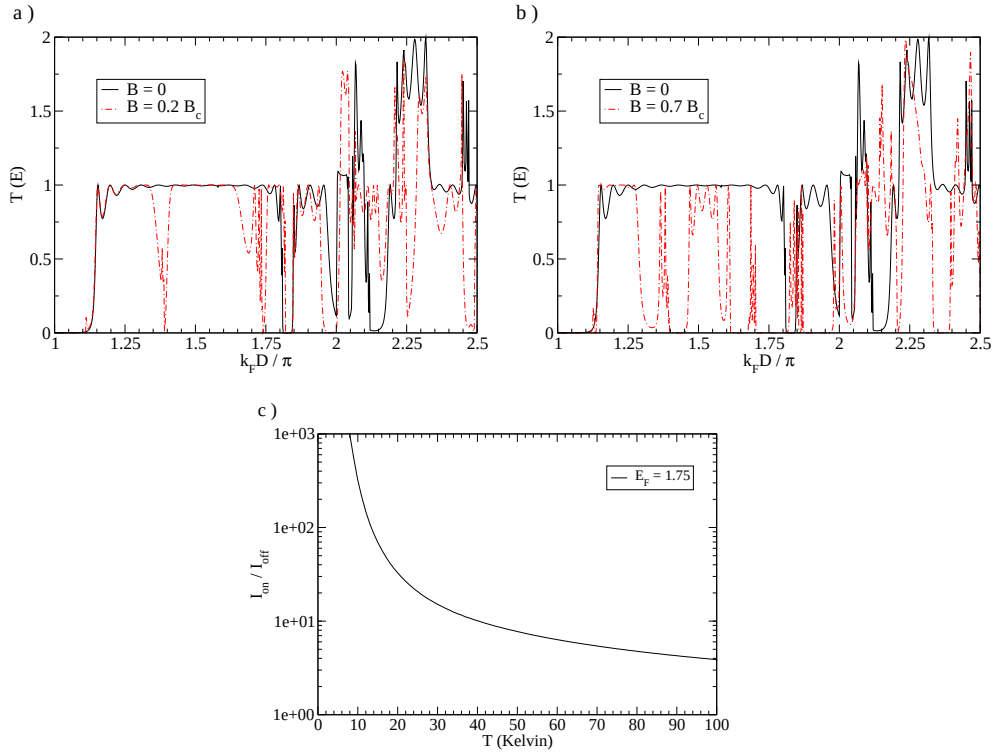

Figure 4.5: (a) - (b) Quantum transmission coefficients for two values of magnetic field and (c) I_{on}/I_{off} ratio for $\xi = 0.7$ in a strongly ($D = 0.5W$) coupled array of dots with $L_b = 0.285W$. E_F is given in units of open channels $k_F D/\pi$.

Figure 4.5(a)-(b) shows the transmission coeffcient for such a geometry of leads ($L_b = 0.285W$). We observe that the transmission spectra require a rather strong magnetic field ($\xi = 0.7$) in order to be modified enough such that a sufficient suppression-enhancement mechanism is imposed. For the setup in discussion and operation typically at 1.4 open channels the magnetic field $B_c \sim 7.389$ T, i.e. a magnetic field of strength ~ 1.4 T is not sufficient and one should use a stronger field of the order of 5 T. Figure 4.5(c) shows the I_{on}/I_{off} ratios for the latter case. Enhanced ratios larger than 100 are achieved for temperatures lower of 14 K whereas a sufficient portion of current flow larger than ten is preserved up to 40 K. These efficiencies are indeed better than the ones achieved before, however, the large magnetic field is not so preferable with respect to our switching mechanism.

Further, in Figure 4.6 we present results for leads of the same width but with larger length $L_b = W$. The conclusions that were extracted for shorter leads' length ($L_b = 0.3W$) hold equally for the case presented here, i.e. much stronger magnetic fields are required to modify the transmission spectra. In subfigure 4.6(c) we present the I_{on}/I_{off} ratios which are comparable to the ones of subfigure 4.5(c) however $I_{on}/I_{off} > 10$ extends to 44 K.

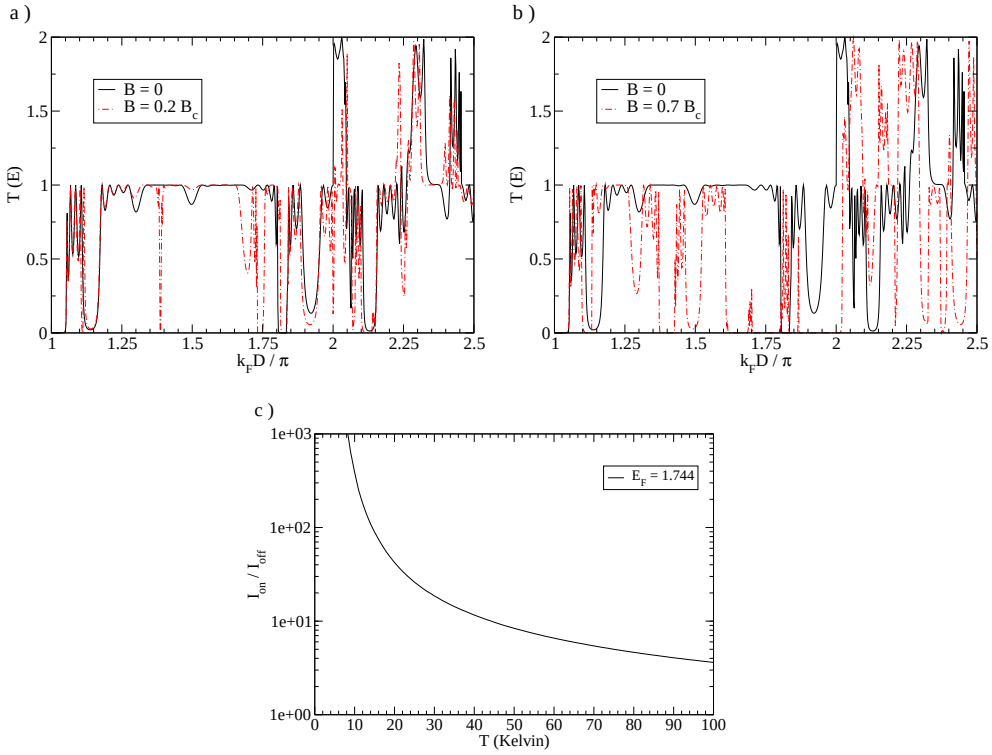

Figure 4.6: (a) - (b) Quantum transmission coefficients for two values of magnetic field and (c) I_{on}/I_{off} ratio for $\xi = 0.7$ in a strongly ($D = 0.5W$) coupled array of dots with $L_b = W$. E_F is given in units of open channels $k_F D/\pi$.

Thus, we conclude that leads that are strongly coupled to the array correspond to a more robust transmission mechanism on the expense of a stronger magnetic field required to provoke a sufficient current flow.

4.2.3 Weak coupling regime

On the contrary, thin energy bands induce a a less clear transmission of electrons in the sense that apart from its small width the transmission coeffcient does not even approach one (see for example subfigures 4.1 (b) and (c)). Significant changes in the transmission spectra are indeed invoked by much weaker magnetic fields. In our simulations the weak coupling regime corresponds to $D = 0.2W$ and for an operation at typically 1.4 open channels $B_c \sim 2.955$ T. The following results hold for $L_b = 0.3W$. In Fig.4.8(a) we observe that at $E_F = 1.81$ channels there is a bright window for $B = 0$ T which is suppressed to dark for already $\xi = 0.2$. Fig.4.8(b) shows the I_{on}/I_{off} for this set of parameters; the efficiency is however rather poor. The result does not significantly modify even if we further increase the magnetic field to $\xi = 0.7$. In subfigures 4.8(e)-(f) we present the transmission coefficient (left column) and I_{on}/I_{off} ratio (right column) for an intermediate lead which is considerably longer, namely $L_b = W$. The results do not show severe modifications in

comparison to the cases with shorter length and they lead us to conclude that the thin energy bands provide a transmission and subsequently current flow that is insufficient to provide a switching mechanism even when we apply rather strong fields.

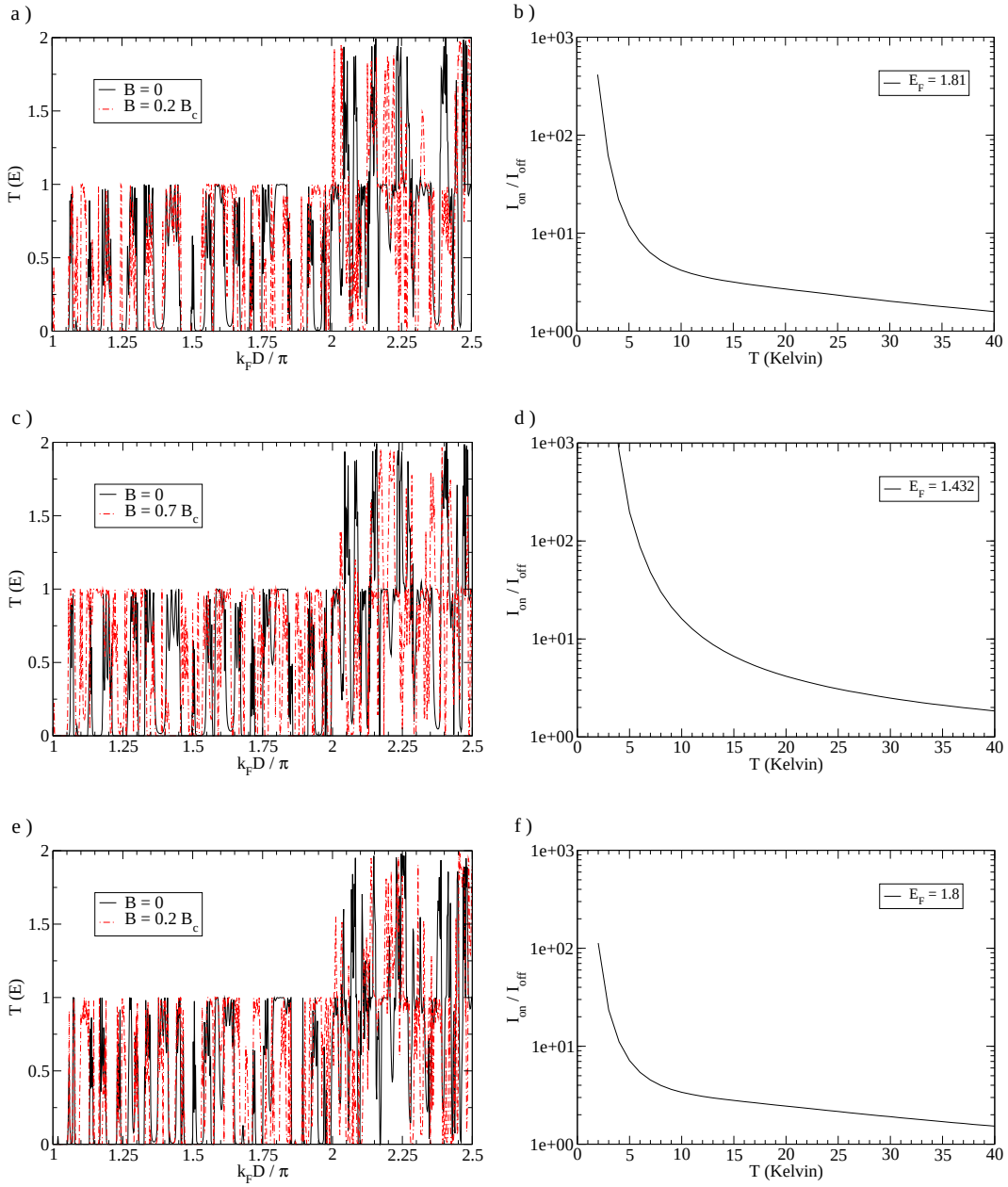

Figure 4.7: Quantum transmission coefficients (left column) and I_{on}/I_{off} ratios (left column) for a weakly ($D = 0.2W$) coupled array of dots. Subfigures (a)-(d) correspond to $L_b = 0.3W$ and subfigures (e)-(f) correspond to $L_b = W$. E_F is given in units of open channels $k_F D/\pi$.

For the purposes of our study we have investigated so far several geometries of the coupling media that belong either to the strong or to the weak coupling regime. We have seen

that the former require strong magnetic fields so as to modify enough, the latter however provide a mechanism that is insufficient to cause enough portion of current flow. The optimal solution has proven to be the regime of intermediate coupling strength, i.e. the one where $D = 0.3W$. Regarding the length L_b of the coupling leads, analogous changes in the transmission spectra have been induced by various values of L_b, however the best qualitative results have been obtained for the chosen value of $L_b = D$.

4.2.4 Quantum dots of rectangular shape

Concerning the geometry of the quantum dots we have also performed simulations for rectangular shaped dots. By reducing the length of the dots and keeping their width constant, we effectively change the coupling between them, since one of their dimensions becomes comparable to the width of the leads leading to the strong coupling regime. In Fig.4.8 we present the transmission coefficients for dots with length $L_d = 0.3W$. Subfigure (a) corresponds to $D = 0.3W$ and (b) $D = 0.2W$. We observe broad bright windows which show an even more robust behaviour as it has been expected. Our results confirm this statement and therefore we conclude that rectangular shape quantum dots rather complete than suit to the purposes of our analysis. The above mentioned arguments have led us to the choice of the square geometry for the dots of the array, which we believe gives better response in an environment of finite temperatures.

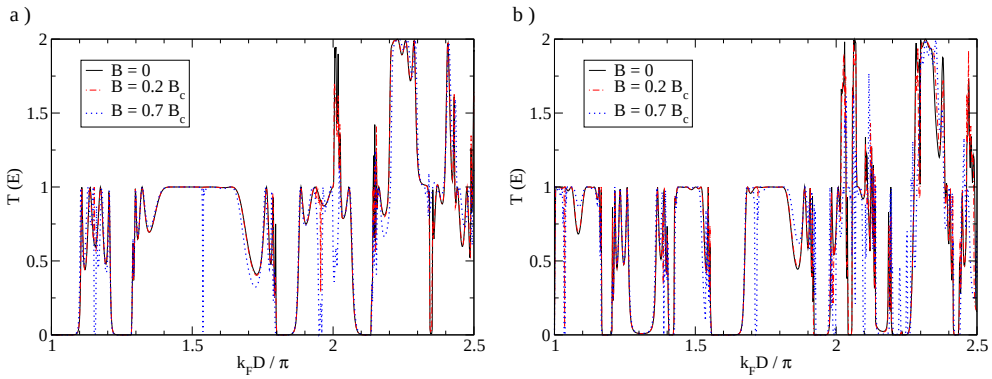

Figure 4.8: Quantum transmission coefficients for quantum dots of rectangular shape $L_d = 0.3W$ for (a) $D = 0.3W$ and (b) $D = 0.2W$ and several magnetic field strengths. E_F is given in units of open channels $k_F D/\pi$.

Hence, we conclude that optimal shape for the quantum dots should belong to the square geometry.

4.3 Discussion of spin splitting

Some further comments concerning our investigations are in order. During our calculations we have neglected the Zeeman energy splitting due to the applied magnetic field. In the however non-negligible Zeeman term, the two-fold spin degenerate energy bands split and their positions are symmetrically shifted with respect to with spin up and down electrons. The energetical shift is given by,

$$E_S = \pm\frac{1}{2}g^*\mu_B B \tag{4.2}$$

where the Bohr magneton $\mu_B = \frac{\hbar}{2m_0}$ and within our calculations $B = \xi B_c = \xi\frac{n_{ch}\hbar\pi}{eDW}$. The variable $n_{ch} = \frac{k_F D}{\pi}$ denotes the number of open channels. In the system of natural units that we have introduced, $\hbar = 2m^* = a = e = 1$ and therefore the contribution of the Zeeman energy term simplifies to $E_S = \pm\frac{1}{2}g^*c^*\xi\frac{n_{ch}\pi}{DW}$ where the dimensions of the physical system are now given in units of the lattice constant a ($m^* = c^*m_0$). Let us now estimate its contribution to the total energy of the system for a GaAs material with effective mass $m* = 0.067$ and Landé factor $g^* = -0.44$. In our calculations the typical strength of the magnetic field is $\xi = 0.3$. By taking into account these values, the correction to the energy due to the Zeeman term for operating at the maximalistic value of $n_{ch} = 2.5$ channels is of the order of $10^{-5}V$. One up to three open channels correspond to a Fermi energy that ranges typically between $\sim 0.05 - 1.5$ in natural units V and therefore we are justified in neglecting the Zeeman contribution to the energy of the system. Although the Zeeman term turns out to be negligible, we do not consider that spin-selective transport spoils our results. On the contrary we believe that in the strong magnetic field regime it would much improve them, in the sense that spin filtering for at least one spin component would become much more enhanced in comparison to its counterpart that would be suppressed, leading to the functionality of our array as a spin filtering device. We remark however that the magnetic field should be particularly stronger, therefore departing from the purposes of the present investigation.

4.4 Conclusions

To summarize, we have presented an investigation of linear quantum transport through an array of a varying small number of quantum dots. Our results have shown a well defined enhancement - suppresion current flow mechanism, which is induced by the electronic band structure of the periodic system and is robust for several tens of Kelvin in a region of ~ 300 nm with a field strength of the order of ~ 0.5 T. The geometries of the array's ingredient units have been discussed in the light of robust on/off ratios. We have concluded that the optimal switching mechanism is provided by an intermediate coupling between the quantum

dot cells which is translated to $D = 0.3W$. Stronger or weaker couplings offer various setups with potential advantages which however cancel in the view of our calculations. Quantum dots of rectangular shape have shown an effective stronger coupling if one of their dimension becomes comparable with the dimensions of the leads. Additional possibilities to increase the efficiency of the I_{on}/I_{off} ratios have been investigated for several materials.

Chapter 5

Short review on the field of closed quantum dots and motivaton

5.1 Electronic structure of quantum dots

So far we have viewed the quantum dots (QDs) in terms of a two-dimensional electron gas which with applying external electrostatic voltages, one can restrict the space of the electronic motion thereby imposing hard wall boundary conditions for it. So far we have investigated ballistic transport with respect to the fact that transmission is defined in by the sample's boundaries. In this regard we have used the terminology "open quantum dots" in order to indicate the fact that the single-electron picture has provided a reliable description of the physics in systems strongly coupled to the environment. In the following chapters we are going to deal with the physics of a system in which a bunch of electrons is severely restricted or "isolated" from its external environment, i.e. the leads. In these systems, i.e. that are weakly coupled to the external environment, transport is dominated by their many-body electronic structure. In order to make the link to the Landauer formalism one could think that to a first order the effect of the coupling $\Gamma(E)$ to the external environment broadens the energy levels. The weaker the coupling is the less overlap between the energy levels is observed and therefore transport through the quantum dot is solely defined by its electronic structure. In this sense quantum dots have established fascinating laboratories for the observation of many kinds of atomic-scale phenomena in a controlled manner due to the fact that their shape and number of confined electrons can be controlled experimentally. Several books [42, 43] and reviews [44, 45] have offered detailed insight in the physics of these low dimensional quantum confined structures at both a theoretical and experimental level.

Electrostatic confinement can be usually well approximated by a parabolic well, at least in the few electron regime. So far many theoretical investigations, have assumed a circular symmetry of the confinement, while the number of electrons ranges from a few to many hundreds. In beautiful analogy to the atomic shell structure a two-dimensional single-particle harmonic oscillator model has provided a fairly good description of the quantum dot shell

structure [44]. This fact is further supported by experimental measurements in which the magic numbers, i.e. number of confined electrons belonging to a shell, that are observed in the addition energy spectra are in good agreement with those for circularly symmetric QDs e.g. in [45–48]. Excitation spectra of QDs can be also probed by single-electron transport spectroscopy [47, 49]. From a theoretical point of view, one of the most powerful tools to study the electronic properties of few-electron quantum dots in a 'clean' and accurate way, is the configuration interaction method which has been extensively employed [50–72]. Additionally, the few-electron problem allows to apply various other theoretical approaches such as perturbative techniques [73–76], semiclassical analysis [77–79] and Padé approximation [80].

Imposing external magnetic fields leads to a variety of new and unexpected properties. The ground state parity oscillations [81, 82] or the magic numbers in the angular momentum [50, 53, 83–86] are beautiful manifestations of the response of the interelectronic interaction to the magnetic field. Experimentally, the magnetic field has been a useful tool for probing the electronic structure of QDs. Hence, the change of the ground state parity was identified as a kink in the addition energy spectra [87–91] and the excitation spectrum of a QD could be probed and compared with exact calculations [45, 47]. Moreover, the response of the many-electron QD to magnetic fields has revealed further rich scenarios. For the low-field regime, the measurements were explained within the constant-interaction model taking into account the exchange interaction between electrons with parallel spins [46]. For higher field strengths the enhanced many-body correlations triggered different mechanisms for the reconstruction of a stable electronic configuration, the so called maximum density droplet. Examples are the formation of a hole in the center or at the edge of the QD or a spin texture [92].

For a parabolic confinement which is elliptically deformed, the rotational symmetry is broken altering the dot's atomic-like properties [44, 93]. The reduction of the symmetry lifts the degeneracies of the single-particle excitation spectrum and affects the selection rules by producing coupling effects between the states [94]. Several theoretical investigations [94–105] have demonstrated the effect of anisotropy. The pattern in the addition energy spectra is much less pronounced, even for small deformations, and vanishes for stronger anisotropies. Furthermore, it might affect spin configurations, which are found to obey the Hund's rule for small QDs while for larger ones Hund's rule is supressed to a more Pauli-like behavior [98, 104]. For example, with increasing deformation, the ground state of four electrons undergoes a transition from a spin-triplet (due to the Hund's rule for circular symmetry) to a spin-singlet state. Other interesting effects arise from the possibility of tuning the degree of degeneracy in the single-particle spectrum by changing the anisotropic harmonic configuration. At various configurations we encounter in the corresponding spectra degeneracies and shell structures thereby predicting other sets of magic numbers for the shell closures. However, the reduced energetical spacing between the shells renders it more complicated to be observed experimentally [93, 105, 106]. Dynamically, the anisotropy serves as a rapid path to chaos in the interacting system leading to an interplay of chaos and integrabil-

ity [107, 108]. A variety of numerical approaches has been applied in order to investigate the lowering of the symmetry in the electronic properties of QDs. These include configuration interaction [94–97, 107–110], Hartree [111], Hartree-Fock [98] and spin-density functional theory [100, 103–105, 112, 113]. The effect of the magnetic field on the shell structure of asymmetric quantum dots has also been discussed both theoretically [114] and experimentally [93, 115]. The investigations performed so far, use mainly a quasi two-dimensional model for the QD. In three dimensions anisotropies have been introduced along the z-axis of the confinement [116] and symmetries are controlled via an external magnetic field [117]. Three dimensional cylindrical [77, 82, 117, 118], ellipsoidal [119–121] or lens-shaped [122] QDs have also been studied.

In the following two chapters we are going to focus on closed quantum dots which contain two electrons electrostatically confined by a two-dimensional anisotropic harmonic oscillator potential. The working Hamiltonian is of fundamental interest since it describes two interacting charged particles in an anisotropic confinement and beyond the quantum dot it could equally describe ions that are trapped in external fields. Hence, we are provided with an ideal laboratory to investigate the effects of electron-electron interaction and anisotropy in the dynamics, electronic structure and quantum chaos in isolated quantum dots. Due to the small number of particles, by applying a configuration-interaction approach in combination with the numerical method introduced for the evaluation of the electron-electron integrals in appendix A, it is possible to obtain a global view on the excitation spectra. We study many excited states for the complete range of anisotropies, i.e. from a circular to an elliptically shaped and in the limit a wire-like dot. An amazing variability and complexity of dynamical and spectral properties occur as a result of various configurations of the confinement. Quantum manifestations such as energy gaps and level clustering on the one hand and level repulsion and avoided crossings on the other hand, are accompanied by the interplay of integrability and chaos in the corresponding classical dynamics. The fingerprints of the chaotic dynamics in the spectra for general anisotropies will be shown. Further quantities such as charge densities are studied to elucidate the effect of the elliptical confinement on the interacting system. Chapter 6 deals with the situation where no magnetic field is applied. By imposing an external magnetic field the ground state parity symmetry oscillates between spin singlet and spin triplet symmetry, a sound effect of the Coulomb interaction between the two electrons. The deformation of the confinement potential and the inclusion of the spin Zeeman splitting in the energy of the ground state causes oscillations' crossovers which occur at unique positions in the space of the magnetic field strength and shape of the dot. Usually these crossovers can easily be identified experimentally by a kink in the conductance. As a result we have concluded that information about the exact shape of the dot's confinement can be extracted if one compares the position of the experimental kink with our theoretical calculations. The results for finite magnetic field will be presented in chapter 7.

Chapter 6

Electronic properties of two-electron anisotropic quantum dots

6.1 Introduction

In this chapter we are going to present a detailed investigation of the effects of Coulombic interaction and anisotropy on the electronic structure and dynamical properties of two-electron quantum dots. The system is found to be integrable for two frequency ratios and the excitation spectra exhibit remarkable spin symmetry properties originating from the symmetries of the quantum operators belonging to the integrals of motion. The implemented numerical algorithm for the evaluation of the electron-electron integrals allowed for the efficient and accurate evaluation of several hundreds of energy levels. Hence, we managed to trace the chaotic dynamics in terms of a statistical analysis of the fluctuation properties of the energy levels for a mixed phase space. The structure of the energy level spacings is analyzed in detail. It shows unique characteristics for several cases: for very strong anisotropies, i.e. for the wire-like limit, the dynamical properties comprise the complete regime from softly interacting to kicked oscillators while the quantum counterpart sustains Wigner crystallization and exhibits intriguing patterns in the spectral sequence of level spacings. Further quantities such as the charge density are studied to elucidate the effect of the elliptical confinement on the interacting system..

This chapter is organized as follows. In Sec. 6.2 we formulate the Hamiltonian of the electronic motion and discuss its general properties. Additionally, we present our computational method. In Sec. 6.3 we present and analyze our results on the QD for various configurations by changing the tunable anisotropy parameter. Finally in Sec. 6.4 we provide our conclusions.

6.2 Hamiltonian and computational method

Two conduction band electrons confined in a two-dimensional anisotropic quantum dot in the effective mass approximation are described by the Hamiltonian $\mathcal{H} = \mathcal{H}_{CM} + \mathcal{H}_r$ with

$$\mathcal{H}_{CM} = \frac{1}{4m_e}\mathbf{P}^2 + m_e\omega_o^2\left(cos^2\phi\, X^2 + sin^2\phi\, Y^2\right) \tag{6.1}$$

$$\mathcal{H}_r = \frac{1}{m_e}\mathbf{p}^2 + \frac{m_e}{4}\omega_o^2\left(cos^2\phi\, x^2 + sin^2\phi\, y^2\right) + \frac{e^2}{4\pi\epsilon\epsilon_o\,|\mathbf{r}|} \tag{6.2}$$

where $m_e, \epsilon, \omega_o, \phi$ are the electron effective mass, dielectric constant, the characteristic oscillator frequency and the anisotropy parameter, respectively. Small and capital letters refer to the relative and center of mass (CM) degrees of freedom, respectively.

Quantization of the CM harmonic oscillator motion given by $\mathcal{H}_{CM}$ is straightforward. Direct observation of the electronic properties due to $\mathcal{H}_r$ via far infrared spectroscopy is prohibited, since radiation in the dipole approximation contains only CM degrees of freedom and decouples from the relative motion $\mathcal{H}_r$. This property is discussed in Maksym and Chakraborty [50], Bakshi *et al* [123] as well as Peeters [124] and is in principle due to the Kohn theorem [125–127]. In the following we focus on the non-trivial relative motion governed by $\mathcal{H}_r$.

To simplify our Hamiltonian we apply a canonical transformation, $x = lx'$, $y = ly'$, $p_x = p'_x/l$, $p_y = p'_y/l$ thereby scaling $\mathcal{H}_r$ into a dimensionless one, via $\mathcal{H}_r = \frac{\hbar^2}{ml^2}\mathcal{H}'_r$. For a GaAs substrate the effective unit of energy and length translate into: the effective Rydberg $Ry^* = 11.8$meV and the effective Bohr radius $l = 9.8$ nm ($\hbar\omega_o = 4.96$meV). This scaling yields the following expression for the dimensionless Hamiltonian of the relative motion,

$$\mathcal{H}_r = -\frac{\partial^2}{\partial x^2} - \frac{\partial^2}{\partial y^2} + \frac{1}{4}\omega_o^2\left(cos^2\phi\, x^2 + sin^2\phi\, y^2\right) + \frac{1}{\sqrt{x^2+y^2}} \tag{6.3}$$

in which the primes have been dropped for simplicity. $\mathcal{H}_r$ belongs to the C_{2v} point-group with parity ($\mathbf{r} \to -\mathbf{r}$) as well as x- and y-parity being symmetries. Hence, due to the Pauli exclusion principle, spin singlet eigenfunctions (even spatial symmetry) can either have odd-odd $(--)$ or even-even $(++)$ x-y-parity, and spin triplet eigenfunctions (odd spatial symmetry) odd-even $(-+)$ or even-odd $(+-)$ x-y-parity.

For the investigation of the properties of the two-electron QD we solve the Schrödinger equation for the Hamiltonian $\mathcal{H}_r$ using a variational full configuration interaction approach leading to an algebraic eigenvalue problem. For convenience (see below) we write eq.(6.3) as $\mathcal{H}_r = (\mathcal{H}_r - \mathcal{H}_0) + \mathcal{H}_0$, where $\mathcal{H}_0$ is the two-dimensional anisotropic harmonic oscillator Hamiltonian,

$$\mathcal{H}_0 = -\frac{\partial^2}{\partial x^2} - \frac{\partial^2}{\partial y^2} + \frac{1}{4}\omega_o^2 \left(cos^2\phi\, x^2 + sin^2\phi\, y^2\right) \tag{6.4}$$

In our approach we use the basis set comprising the eigenfunctions of $\mathcal{H}_0$

$$\Psi_{n_x n_y} = \frac{\sqrt[4]{\omega_x \omega_y / 4}}{\sqrt{\pi 2^{n_x+n_y} n_x! n_y!}} H_{n_x}(\sqrt{\omega_x/2}\, x) H_{n_y}(\sqrt{\omega_y/2}\, y) exp(-\frac{\omega_x}{4}x^2 - \frac{\omega_y}{4}y^2) \tag{6.5}$$

The off-diagonal part of the corresponding Hamiltonian matrix is due to the electron-electron Coulomb repulsion. The electron-electron integrals can be evaluated analytically yielding a fourfold series. Unfortunately, and despite the closed form of the analytical expressions, their evaluation turns out to be numerically unstable. To remedy instabilities, we have used an efficient numerical technique for the evaluation of the Coulomb matrix elements which is described in appendix A. At the same place we provide convergence tests for comparison of our method with respect to analytical attempts to remedy the instabilities.

6.3 Results and discussion

Figure 6.1 (a) shows the evolution of the energies of the first one hundred energetically lowest even-even x-y-parity states (even parity) with respect to the anisotropy angle ϕ. For $\phi = 45^\circ$ the dot acquires a rotational symmetry and the Hamiltonian is integrable. Electron-electron interaction lifts the degeneracies in the even-even x-y-parity states. The energy levels, though non-degenerate, group in clusters and form energy gaps which are particularly pronounced in the higher excitation spectrum. By departing from integrability thereby gradually introducing anisotropies in the shape of the confinement potential the clusters widen and the energy levels interact thereby showing avoided crossings. The inset in Fig. 6.1(a) illustrates this for a certain window of energies and anisotropies. In the regime of intermediate anisotropies we observe pronounced clustering of the energy levels specifically for $\omega_y : \omega_x = 2 : 1$. The width of the energy gaps is however smaller than the one of the isotropic case. By further increasing anisotropy, we observe an interplay of avoided crossings and level clustering at certain frequency ratios. Figure 6.1(b) portrays the energy levels at $\omega_y : \omega_x = n : p, n, p \in \mathcal{N}^*$, ($\mathcal{N}^*$ being the set of positive integers) in comparison with those of the non-interacting system (set of two-dimensional anisotropic harmonic oscillators). For the ratios $\omega_y : \omega_x = n : 1$, we observe level clustering, particularly for $n = 2, 3$. For $n > 3$ the shell structure is much less pronounced. At ratios $\omega_y : \omega_x = n : p$ for $n, p > 1$, for which a rather high degree of degeneracy occurs in the non-interacting system, the shell structure tends to vanish with increasing n, p. In between the angles corresponding to the low-order ratios $n : p$ mentioned above, avoided crossings dominate the spectra. In

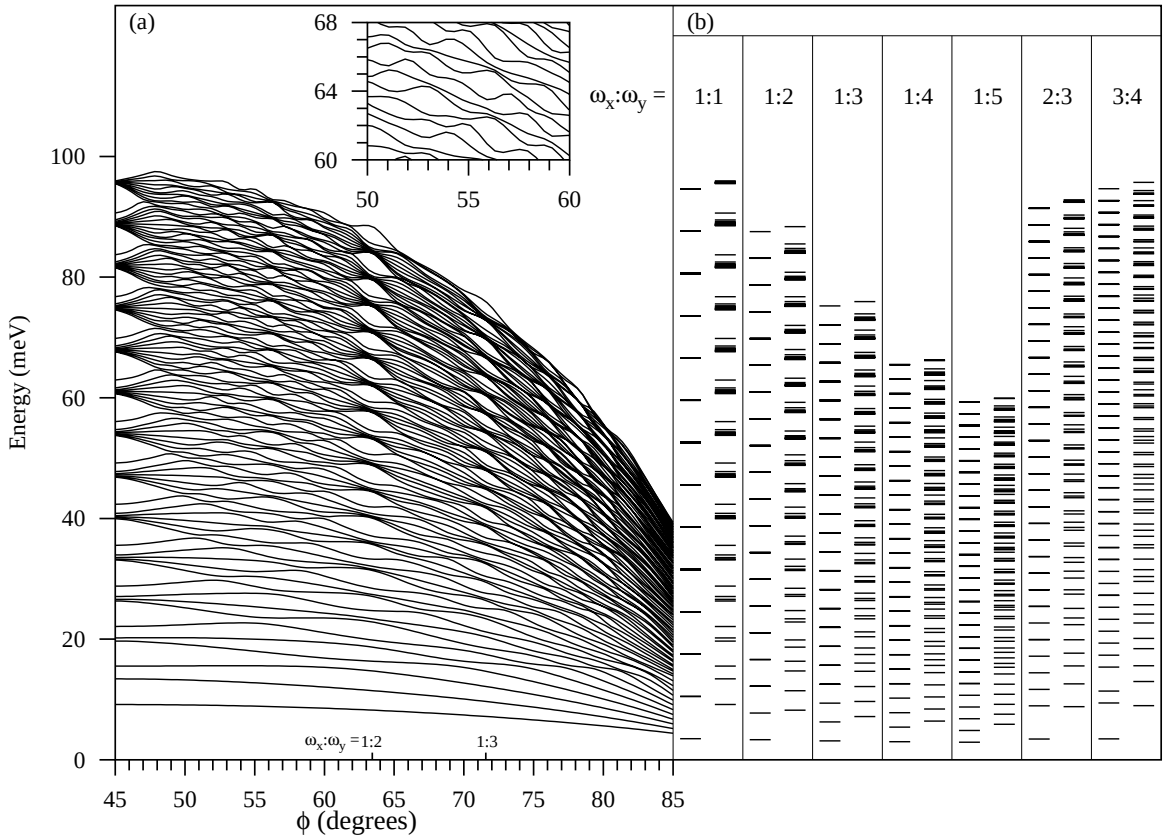

Figure 6.1: (a) The spectrum for the first hundred even-even x-y-parity states of the anisotropic QD as a function of the anisotropy angle ϕ. The inset shows an enlargement for a certain subinterval of energies and angles. (b) Sketch of the shell structure of the energy levels for several frequency ratios $\omega_y : \omega_x = n : p$. The first column corresponds to the non-interacting system while the second one is for the interacting system.

the following subsections we present a detailed investigation of the two-electron dot for the specific regimes of anisotropy we mentioned above.

6.3.1 Isotropic parabolic confinement

In this case the Hamiltonian of the relative motion of equation 6.3 takes the form, in polar coordinates (ρ, θ),

$$\mathcal{H}_r = -\left(\frac{\partial^2}{\partial\rho^2} + \frac{1}{\rho}\frac{\partial}{\partial\rho}\right) + \frac{\hat{L}_z^2}{\rho^2} + \frac{1}{8}\omega_o^2\rho^2 + \frac{1}{\rho} \tag{6.6}$$

$\mathcal{H}_r$ is rotationally symmetric, i.e. it belongs to the $C_{\infty v}$ group, and L_z is conserved. The classical Poincaré Surface of Section (PSOS) in Fig. 6.2 demonstrates integrability.

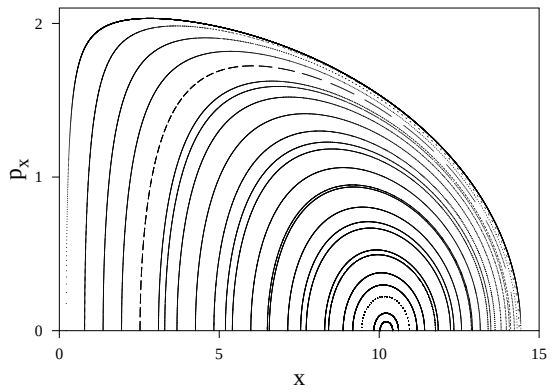

Figure 6.2: Classical phase space (x, p_x for $y = 0$) for $\phi = 45°$ and $E = 55$ meV.

The eigenstates of this Hamiltonian have been obtained both analytically [73, 118, 128] and numerically [51, 59]. Table 6.1 includes the first low-lying excited eigenstates (calculated in effective units) with their symmetries and their magnetic quantum numbers m.

Table 6.1: The sequence of energetically lowest energy levels for isotropic parabolic confinement. Spin symmetry is denoted by s (spin singlet) or t (spin triplet) and the spatial symmetries by the brackets (x-parity, y-parity) where the sign $+$ stands for even and the sign $-$ for odd parity.

Energy (e.u.)	_ symmetries _	m	Energy (e.u.)	_ symmetries _	m
0.776	(s) $(++)$	0	1.668	(s) $(++)$ $(--)$	±4
0.907	(t) $(+-)$ $(-+)$	±1	1.713	(s) $(++)$ $(--)$	±2
1.136	(s) $(++)$ $(--)$	±2	1.873	(s) $(++)$	0
1.316	(s) $(++)$	0	1.947	(t) $(+-)$ $(-+)$	±5
1.396	(t) $(+-)$ $(-+)$	±3	1.978	(t) $(+-)$ $(-+)$	±3
1.471	(t) $(+-)$ $(-+)$	±1	2.044	(t) $(+-)$ $(-+)$	±1

We observe an arrangement of states with respect to their parity. Hence, the ground state is a spin singlet state and the first excited state a spin triplet. Excited states arrange either in groups of spin singlet (even m) or spin triplet (odd m) symmetry with an increasing range of magnetic quantum number m as the energy increases. The states for $m \neq 0$ are two-fold degenerate with respect to the sign of m. In the following we study the discrete energy level spacing (ELS) $\Delta E_i = E_{i+1} - E_i$ as a function of the energy E_i, for the states with even-even x-y-parity. Fig. 6.3 shows $\Delta E_i(E_i)$ for both the non-interacting (inset) and interacting system.

In Fig. 6.3 (inset) one recognizes the energy gaps that occur between the (n_x+n_y+1)-fold degenerate states due to the spectrum of the harmonic oscillator. If we include the electron-electron interaction (Fig. 6.3) well-separated energy gaps persist but the manifold due to the harmonic oscillator splits. Remarkably enough, the sequence of the spacings typically

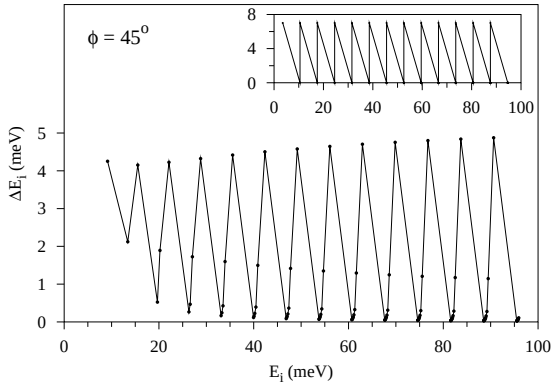

Figure 6.3: Discrete energy level spacing $\Delta E_i(E_i)$ for the first 100 states with $(++)$ symmetry. The inset shows the spectral sequence for the non-interacting system.

increases strongly up to the value of the energy gap and then, i.e. for further increasing energy, 'collapses' in order to increase again. Therefore we encounter a repeated stretching phase of the level spacings for the interacting system.

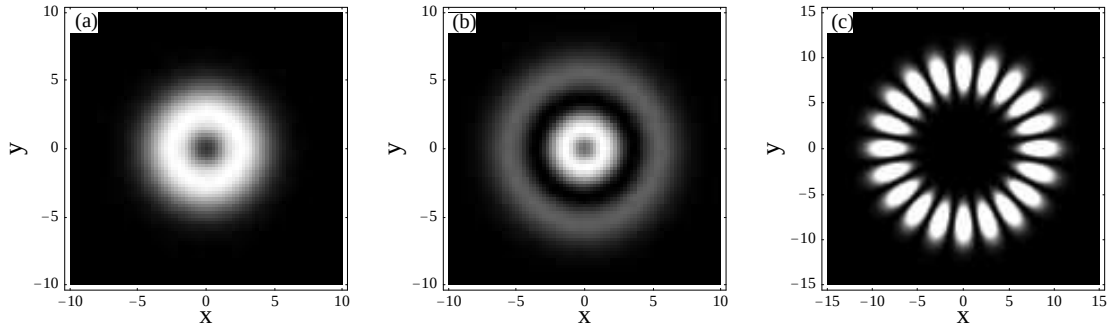

Figure 6.4: Density plot of the square of the absolute value of the two-electron wave function in the circular quantum dot for (a) the singlet ground state (m = 0), (b) the first excited singlet state (m = 0) and (c) a superposition of degenerate states $|\Phi(m = 10) + \Phi(m = -10)|^2$ (dark regions correspond to low and the bright ones to high densities).

In Fig. 6.4 we provide two-dimensional density plots of the charge distribution for selected states. For the ground state the charge density forms a circularly symmetric electronic cloud which contains a central hole due to the pole of the Coulomb repulsion potential.

6.3.2 Transition regime from weak to intermediate anisotropies

The introduction of small anisotropies (with increasing ϕ) breaks the rotational symmetry of the confining potential and lifts the degeneracies in the spectrum. The clusters, which correspond to identical parity, widen and for higher energies ($E \gtrsim 40$meV; for a measure the ground state energy corresponds to ~ 9meV) begin to interact already for small deviations from the circular shape e.g. $\phi = 48°$ ($\frac{\omega_y}{\omega_x} \approx 1.1$). For the symmetry pure spectrum, e.g.

Fig. 6.1(a) for the $(++)$ states, the non-crossing rule holds and we observe a large number of avoided crossings. The inset in Fig. 6.1(a) illustrates this for a subinterval of energies and angles.

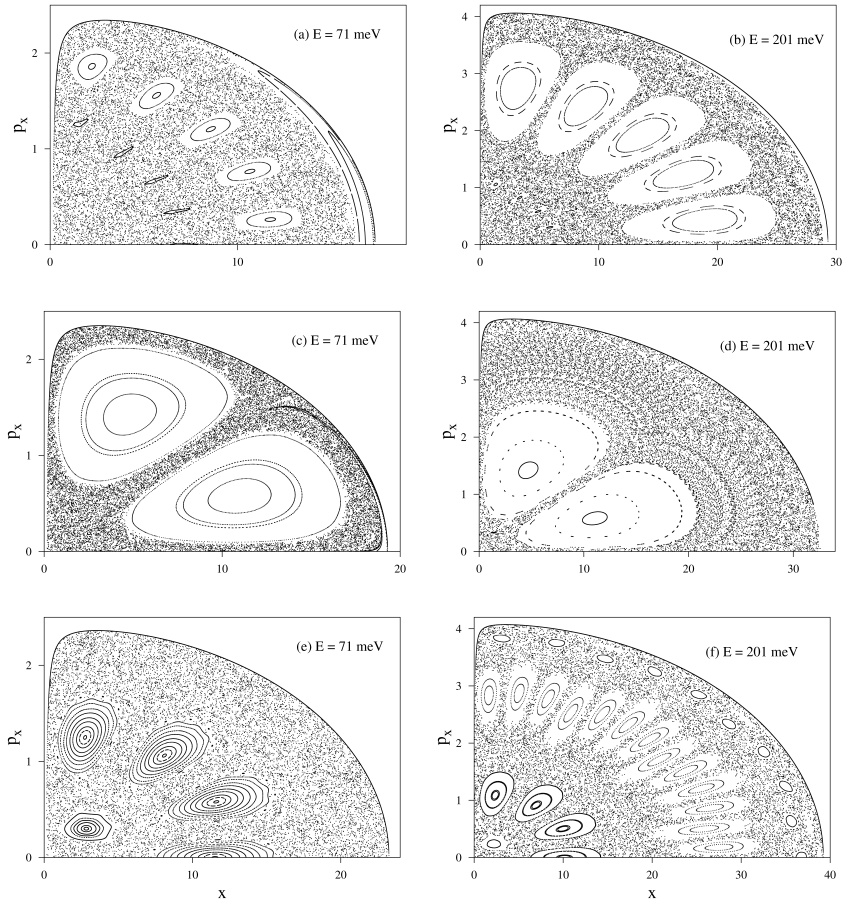

Figure 6.5: The Poincaré surfaces of section (x, p_x for $y = 0$) for various angles and energies. Subfigures (a) and (b) correspond to $\phi = 48°$, (c) and (d) to $\phi = 53°$ and (e) and (f) to $\phi = 60°$.

For a further analysis of the effect of anisotropy, let us consider the underlying classical dynamics. Figure 6.5 shows a series of PSOS for a range of angles in the regime we are studying and for two significantly different energies ($E = 71$, 201 meV). For $\phi = 48°$ ($\frac{\omega_y}{\omega_x} \approx 1.1$) the classical phase space shows already a significant portion of chaos (subfigure 6.5(a)). With increasing energy E, the regular parts of the phase space expand. For $\phi = 53°$ and $E = 71$ meV there are two dominating regular islands embedded in a chaotic sea. This highly regular structure is due to the fact that $\phi = 53°$ is close to the frequency ratio $\omega_y/\omega_x = 4/3 \Rightarrow \phi = 53.1°$, which, as we shall see later on, leads to certain dynamical and spectral properties of the system. For higher energies, e.g. $E = 201$ meV, the portion of chaos has significantly increased. For $\phi = 60°$ the phase space is dominated by chaos for all the energies considered here.

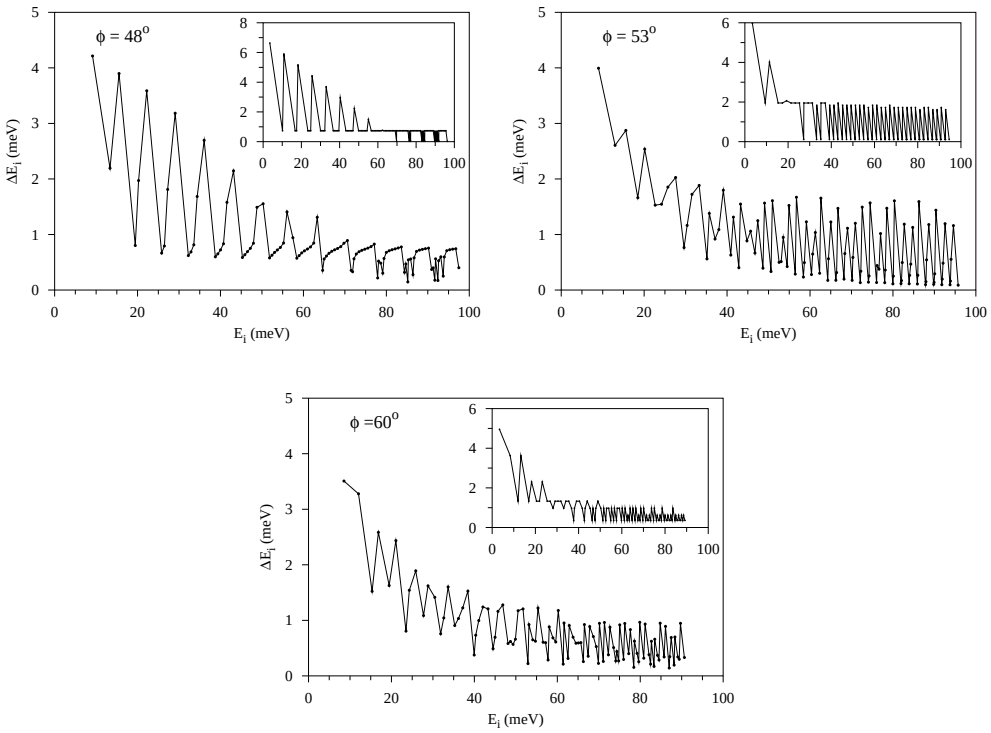

Figure 6.6: Discrete energy level spacing $\Delta E_i(E_i)$ for the non-interacting (inset) and interacting system, for the first 100 states with $(++)$ symmetry and various angles.

Figure 6.6 shows the ELS for the non-interacting and interacting systems for $\phi = 48°$, $53°$ and $60°$. For $\phi = 48°$ and lower energies, the single particle ELS exhibits peaks which correspond to the energy gaps reminiscent of the isotropic case. With increasing energy, these gaps become smaller since the lifting of the degeneracies, due to the anisotropy, leads to widened bunches of clusters, the width of which increases with energy thereby decreasing the gaps between the clusters. The equidistant intracluster spacings lead to the pronounced plateaus. Allowing for interaction results in a similar arrangement of the main peaks concerning the large spacings while we observe an energetical stretching i.e. raise of the plateaus. At $\phi = 53°$ the non-interacting system is, as already indicated, close to the rational frequency ratio $\omega_y/\omega_x = 4/3$, which corresponds to a high degree of degeneracy and therefore we observe level clustering, i.e. $\Delta E_i(E_i)$ comes close to zero, here. The series of the energy gaps shown in Fig. 6.6 are ascribed to the distance between these level clusters while the very small spacings explain the fact that at $53°$ we are close to the degeneracies. In this case interaction effects lead to significant changes of the ELS ,i.e., to an overall more irregular profile. However, major properties such as the repeated occurence of approximate degeneracies and gaps persist. For $\phi = 60°$ the inclusion of interaction results in an even more irregular profile for the ELS, thereby preserving the decaying envelope behavior of the non-interacting ELS. In general, one can conclude that the interaction changes the behavior of the ELS function significantly and only certain overall features of it are preserved

compared to the non-interacting case.

An established tool for tracing the fingerprints of chaotic classical dynamics on the excitation spectrum of the corresponding quantum system, is the study of the fluctuation properties of the excitation spectrum [129–131]. The large number of converged levels (~ 400), allowed us to apply the statistical measures to long spectral sequences. Standard quantities to study are the nearest neighbor spacing distribution (NNSD) and the spectral rigidity (SR). These universal measures should be applied to the unfolded spectrum $\varepsilon_i = \langle N(E_i) \rangle$ where $N(E) = \sum_i \Theta(E - E_i)$, with $\{E_i\}$ being the discrete energy level sequence obtained by our computational method.

For integrable generic systems the NNSD follows a Poisson distribution (PD), $\mathcal{P}_P(s) = e^{-s}$ with s being the spacing between two adjacent levels ε_i. The Hamiltonian (6.3) of the relative motion is invariant under time reversal and reflection in the (x, y) plane. For these symmetries assuming fully chaotic phase space, the statistical properties NNSD and SR of the energy levels are predicted by real symmetric random matrices [Gaussian Orthogonal ensemble (GOE)]. For the NNSD the behavior predicted for the GOE spectra is the Wigner distribution, $\mathcal{P}_W(s) = \frac{\pi}{2} s e^{-\frac{\pi}{4}s^2}$. For mixed phase space, which is typical for our system (e.g. Fig. 6.5), the statistical distributions should be in between the Poisson and Wigner ones. There are various families of distributions which have been proposed to interpolate the NNSD for these cases. Among these are the Brody distribution (BD), [132, 133] $\mathcal{P}_B(s) = a(q+1)s^q e^{-as^{q+1}}$ with $a = \Gamma\left(\frac{q+2}{q+1}\right)^{q+1}$ which interpolates between the Poisson ($q = 0$) and Wigner ($q = 1$) distributions, and the semiclassical approximation, i.e. the Berry-Robnik distribution (BRD), [134] $\mathcal{P}_{B-R}(s) = (1-q)\mathcal{P}_P(s) + q\mathcal{P}_W(s)$ with q being the fraction of chaos in phase space.

The spectral rigidity $\Delta(L)$ is a property attributed to the correlations between the level spacings. For a given substretch $[a, a + L]$ of the spectrum, $\Delta(L)$ measures the mean square deviation of the staircase function $N(\varepsilon)$ from the best straight line fit, $\Delta(L) = \frac{1}{L} \min_{A,B} \int_a^{a+L} [N(\varepsilon) - A\varepsilon - B]^2 d\varepsilon$. For Poisson spectra the spectral rigidity is given by, $\Delta(L) = \frac{L}{15}$ and for GOE spectra it behaves asymptotically (large L) like, $\Delta(L) = \frac{1}{\pi^2} lnL - 0.007$. The exact formula for $\Delta(L)$ is more complicated and we refer the reader to Ref.[[129]] for the corresponding expression.

Figure 6.7 shows the NNSD and the spectral rigidity for the unfolded spectra for the angles $\phi = 48°, 53°$ and $60°$. For $\phi = 48°$ we encounter a mixed phase space (see subfigures 6.5(a) and (b)) with the fraction of chaos varying smoothly with increasing energy between 80% for the energy $E = 50$ meV and 50% for the energy $E = 201$ meV. The energy levels used in the unfolded spectrum correspond to this range of energy. The resulting NNSD deviates significantly from the BRD for $q = 0.5$. Some of the qualitative features of the NNS data such as the maximum of the histogram, are better described by the BD, in comparison with the BRD. The mentioned deviation has its origin in the fact that the underlying inte-

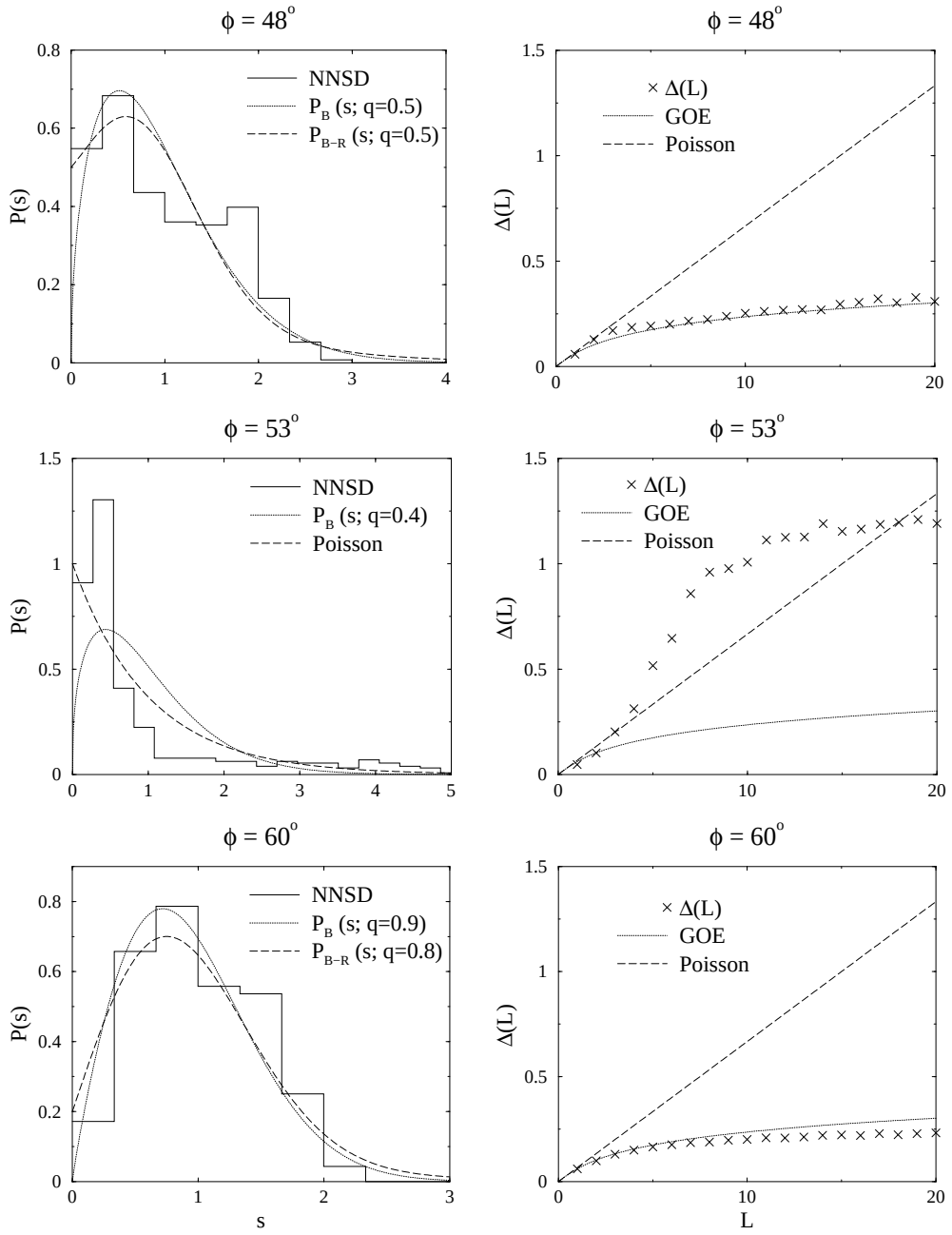

Figure 6.7: Statistical measures NNSD (left column) and spectral rigidity $\Delta(L)$ (right column) for the angles $\phi = 48°, 53°$ and $60°$. The spectral sequences $\{E_i\}$ correspond to sets of converged states with $(++)$ symmetry.

grable system (without the Coulomb interaction) consists of a set of two-dimensional harmonic oscillators whose NNS distribution behaves non-generic, i.e. non-Poissonian. [135] Unexpectedly, the spectral rigidity follows closely the prediction of GOE. For $\phi = 53°$ the classical dot shows a mixed phase space (subfigures 6.5(c) and (d)) being however dominated by two large regular islands. At this ratio (see subsection 6.3.4 for a further analysis

on the electronic structure at the ratios $\omega_y : \omega_x = n : p$) the level clustering observed in the spectrum of the non-interacting system (see Fig. 6.1(b)) occurs, in a somewhat modified way, in the interacting system. This quantum manifestation of the high degree of regularity in the classical phase space results in the oscillating energy gaps in the ELS's (see Fig. 6.6 for $\phi = 53°$). The NNS data show an abnormal behavior compared to the theoretical predictions of the BD and the PD. These two distributions were chosen because they give a better description of the maximum of the histogram (BD) and the behavior for large spacings (PD). The spectral rigidity shows major deviations from the theoretical predictions. For $\phi = 60°$ the phase space is dominated by chaos and the fraction of chaos is roughly independent of energy. It varies smoothly between 90% and 70% for the energies between 50 meV and 150 meV. The corresponding NNSD agrees quite well with the prediction of BRD for $q = 0.8$ chaos and also with BD for $q = 0.9$ (both approach the Wigner distribution). The spectral rigidity follows closely the prediction from GOE spectra.

From our results we conclude that there is no universal family of distributions to describe the NNS data for the regime with mixed phase space, except for the case where chaos is robust with respect to the variation of energy and in particular strongly dominates the phase space ($\phi = 60°$). We ascribe the deviations from the theoretical predictions to the fact that the non-interacting system is non-generic and leaves its fingerprints in the quantum and classical dynamic properties of the interacting system. In particular the abnormal behavior in the case $\phi = 53°$ is ascribed to the robust highly regular behavior of the interacting system (level clustering).

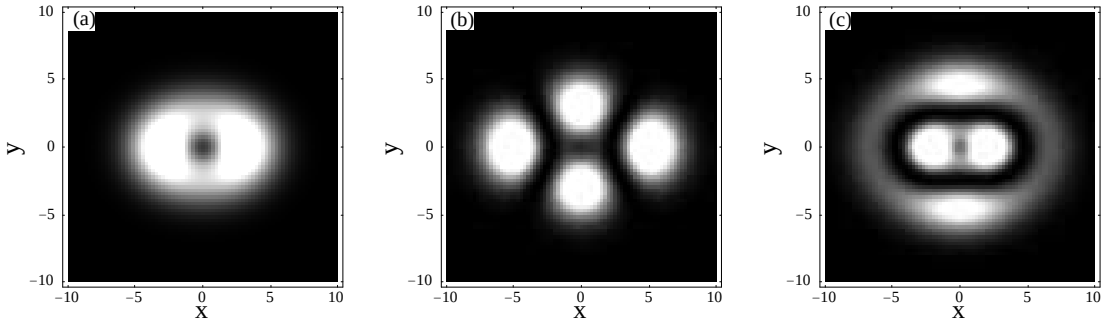

Figure 6.8: Density plot of the square of the absolute value of the two-electron wave function in the case of $\phi = 53°$ for (a) the singlet ground state, (b) the first excited singlet state and (c) the third excited singlet state (dark regions correspond to low and the bright ones to high densities).

Figure 6.8 shows some charge density plots for three selected states. The gradual introduction of anisotropy, with increasing angle ϕ, causes a small weakening in the parabolic confinement along the x-direction ($\omega_x = \omega_o \, cos\phi$) thereby strengthening it in the y-direction. Hence, the two electrons in the ground state are further repelled due to the confinement relaxation along the x-axis and obtain a clear spatial orientation.

6.3.3 Integrable anisotropic configuration

The Hamiltonian (6.3) for the configuration $\omega_y : \omega_x = 2 : 1$ of the confining potential is written explicitly,

$$\mathcal{H}_r = -\frac{\partial^2}{\partial x^2} - \frac{\partial^2}{\partial y^2} + \frac{1}{4}\omega_x^2\left(x^2 + 4\,y^2\right) + \frac{1}{\sqrt{x^2+y^2}} \tag{6.7}$$

At this frequency ratio the spectrum in Fig. 6.1 shows level clustering accompanied by well-pronounced energy gaps. The latter are however of smaller width compared to those of the circular configuration. In the total spectrum, which contains the states of all four symmetries $(++)$, $(--)$, $(+-)$, $(-+)$, we observe groups of energy levels. The classical counterpart (Fig. 6.9) shows a regular phase space and suggests that the system is integrable. The line $p_x = 0$ consists of infinite number of periodic orbits with period one and separates the regular islands (Figure 6.9 shows only one quadrant).

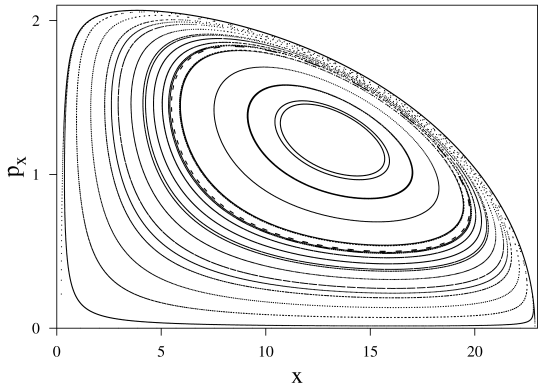

Figure 6.9: Phase space for $\omega_y : \omega_x = 2 : 1$ and $E = 55$ meV.

For three-dimensional systems cases of integrability have been found in previous works, [117, 136–139] addressing different physical settings. In order to prove integrability for our system and calculate explicitly the integral of motion we introduce the two-dimensional parabolic coordinates $x = uv, y = \frac{1}{2}(u^2 - v^2)$, $u \in \mathcal{R}$ and $v \geq 0$, where $\mathcal{R}$ is the set of the real numbers. The Hamiltonian (6.7) then transforms to the new coordinates,

$$\mathcal{H}_r = -\frac{1}{u^2+v^2}\left(\frac{\partial^2}{\partial u^2} + \frac{\partial^2}{\partial v^2}\right) + \frac{\omega_x^2}{4}\,\frac{u^6+v^6}{u^2+v^2} + \frac{2}{u^2+v^2} \tag{6.8}$$

If we apply a product ansatz for the eigenfunctions $\Psi(u,v) = U(u)V(v)$ the Schrödinger equation $\mathcal{H}_r\Psi(u,v) = \varepsilon_r\Psi(u,v)$ can be separated in two ordinary differential equations of the form,

$$\frac{d^2W}{dw^2} + \left(\varepsilon_r w^2 - \frac{\omega_x^2}{4} w^6 - \kappa\right) W = 0 \tag{6.9}$$

where $U(u) = W(u)$ with $\kappa = \lambda_u$, $V(v) = W(v)$ with $\kappa = \lambda_v$, $\lambda_u + \lambda_v = 2$; ε_r denotes the respective eigenvalues. The separation constant $\lambda = \frac{1}{2}(\lambda_v - \lambda_u)$ is the eigenvalue of the operator,

$$\Lambda = \{L_z, p_x\} + \frac{\omega_x^2}{2} y x^2 - \frac{y}{\sqrt{x^2 + y^2}} \tag{6.10}$$

where $\{\}$ denotes the anticommutator. By construction, the operator Λ commutes with the Hamiltonian (6.7) and is indeed the constant of motion of the integrable system. The eigenfunctions $\Psi(u, v)$ are also eigenfunctions of Λ. Λ commutes with the x-parity operator and anticommutes with the y-parity operator. These symmetries of the quantum operator Λ have interesting consequences on the spectrum of the system (see Table 6.2 and discussion below). To our knowledge the operator Λ has no simple geometrical interpretation. We remark that in both angles $\phi = 45^\circ$ and $\omega_y : \omega_x = 2 : 1$ we have non-Abelian symmetry groups which lead to the observed symmetries.

This particular case of integrability of the interacting system can be generalized to include further frequency ratios. Let us consider a general two-dimensional Hamiltonian of the form,

$$\mathcal{H}_r = -\frac{\partial^2}{\partial x^2} - \frac{\partial^2}{\partial y^2} + \frac{\omega_x^2}{4}\left(x^2 + \beta\, y^2\right) + \frac{1}{\sqrt{x^2 + y^2}} \tag{6.11}$$

where anisotropy is tuned via the parameter $\beta = \omega_y^2/\omega_x^2$. For the case of the circular shaped QD the parameter $\beta = 1$ and the constant of motion is L_z (section IV.A). For the case $\beta = 4$ of this subsection the constant of motion is Λ in equation (6.10). For $\omega_y : \omega_x = 1 : 2$ and $\beta = 1/4$ the Hamiltonian (6.11) is again integrable, the constant of motion being now,

$$\Lambda = -\{L_z, p_y\} + \frac{\omega_x^2}{8} x y^2 - \frac{x}{\sqrt{x^2 + y^2}} \tag{6.12}$$

The previously mentioned integrals of motion of the Hamiltonian (6.11) for specific values of β can be summarized and generalized via the scalar quantum operator,

$$\Xi = \vec{f}\left\{2\left(\vec{p}\times\vec{L}\right) - i\hbar\vec{p} + \hat{e}L_z - \frac{\omega_x^2}{6}\left[\left(\vec{r}\times\vec{W}\right)\times\vec{r}\right] + \frac{\vec{r}}{|\vec{r}|}\right\} \tag{6.13}$$

with $\vec{f} = \left(tan\left(\frac{\pi}{3}\left(\beta-1\right)\right), tan\left(\frac{\pi}{3}\left(\frac{1}{\beta}-1\right)\right), 1\right)$, $\vec{W} = (x, \beta y, 0)$, $\vec{L} = (0,0,L_z)$, $\hat{e} = (1,1,1)$ and $\vec{r} = (x,y,0)$.

For the particular values $\beta = 4, 1, 1/4$ the operator (6.13) represents the integral of motion responsible for the integrability of the Hamiltonian (6.11). In the expression (6.13), one can identify in the vector multiplied from the right side by $\vec{f}$, the generalized Runge-Lenz vector as being defined by Beims and Gallas [139] but with a different sign for the last term and additionally some new terms follow, characteristic for our generalized problem. Let us now return to the analysis of the excitation spectrum.

Table 6.2: A sequence of excited energy levels for the configuration $\omega_y : \omega_x = 2:1$ of the confinement. The line separates groups of levels with different x-parity.

Energy (e.u.)	spin / reflection symmetries
0.697	(s) $(++)$
0.732	(t) $(-+)$
0.971	(s) $(++)$ (t) $(+-)$
1.070	(t) $(-+)$ (s) $(--)$
1.248	(s) $(++)$ (t) $(+-)$
1.384	(s) $(++)$
1.408	(t) $(-+)$ (s) $(--)$
1.443	(t) $(-+)$
1.582	(s) $(++)$ (t) $(+-)$
1.682	(s) $(++)$ (t) $(+-)$
1.757	(t) $(-+)$ (s) $(--)$
1.796	(t) $(-+)$ (s) $(--)$

Table 6.2 contains a sequence of low-lying energy eigenvalues. A genuine feature of this table is the groups of energy levels which belong either to $(++)$ and $(+-)$ symmetry or to $(-+)$ and $(--)$ symmetry. This is a result of the symmetry of the constant of motion Λ which commutes with the x-parity and anticommutes with the y-parity operator. The states with eigenvalue $\lambda = 0$ are non-degenerate and those with eigenvalue $\lambda \neq 0$ are doubly degenerate with respect to the sign of λ. The ground state of the system is a spin singlet $(++)$ state which emerges from the isotropic dot, with increasing ϕ. The next two excited states in the isotropic case, are doubly-degenerate spin triplet $(+-)$ and $(-+)$ states, followed by

doubly-degenerate spin singlet $(++)$ and $(--)$ states (see Table 6.1). With the introduction of the anisotropy the doubly degenerate states split in two states. The spin triplet $(-+)$ state forms the first excited state of the system in the case $\omega_y : \omega_x = 2 : 1$ and the spin triplet $(+-)$ state crosses with the spin singlet $(++)$ state at $\omega_y : \omega_x = 2 : 1$ to form a doubly-degenerate state. With increasing energy the states evolve in groups following the above mentioned symmetries.

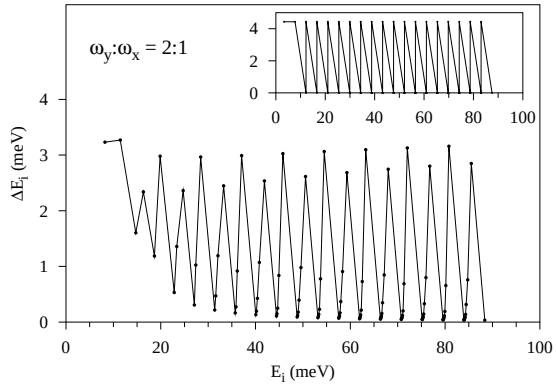

Figure 6.10: $\Delta E_i(E_i)$ for the non-interacting (inset) and interacting system, for the first 100 states with $(++)$ symmetry and $\omega_y : \omega_x = 2 : 1$ anisotropic configuration.

Figure 6.10 shows the ELS for $\omega_y : \omega_x = 2 : 1$. The non-interacting system shows energy gaps which occur due to the $\left[\frac{N_0}{2} + 1\right]$-fold degeneracy (the brackets [] indicate the integer part of the enclosed number) of the energy levels where $N_0 = n_x + 2n_y = 0, 1, 2, \ldots$. The inclusion of interaction lifts the degeneracies in the single-particle spectrum resulting in a repeated energetical stretching phase with increasing energy. The well-pronounced energy gaps follow an oscillatory behavior (see Fig. 6.10).

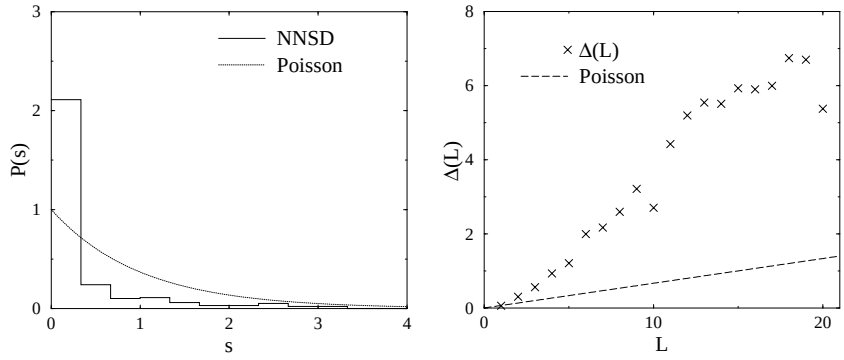

Figure 6.11: Statistical measures NNSD and spectral rigidity $\Delta(L)$ for $\omega_y : \omega_x = 2 : 1$.

In Fig. 6.11 we present the statistical measures NNSD and SR applied to the unfolded spectrum for the integrable case. The NNSD shows a behavior which deviates significantly from a Poissonian distribution and possesses a rather rapid decay. The spectral rigidity $\Delta(L)$

shows again remarkable deviations from the Poissonian prediction. These results show that the high degree of degeneracy in the underlying non-generic single-particle spectrum leads to this specific type of abnormal statistical behavior of the numerical data.

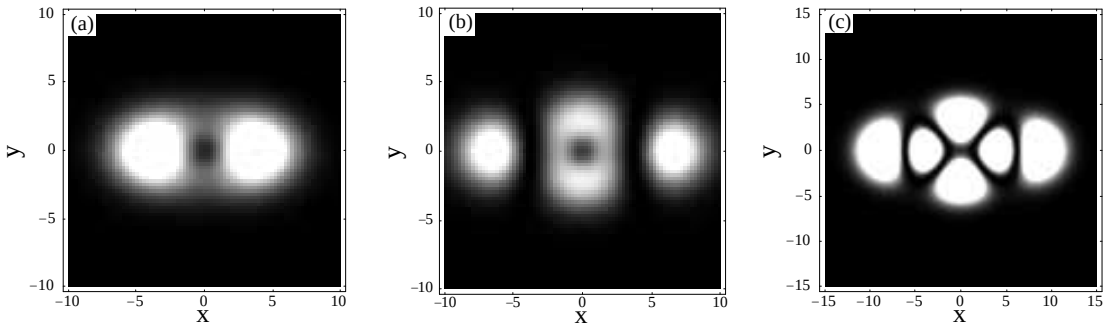

Figure 6.12: Density plot of the square of the absolute value of the two-electron wave function in the case of $\omega_y : \omega_x = 2 : 1$ for (a) the singlet ground state, (b) the first excited singlet state and (c) the third excited singlet state (dark regions correspond to low and the bright ones to high densities).

Fig. 6.12 shows the charge distribution in the case of the well established anisotropy for $\omega_y : \omega_x = 2 : 1$. This resuts in an electronic cloud for the ground state which is clearly elongated along the x-axis.

6.3.4 Regime of strong anisotropies

For $\phi > 63.4°$, the excitation spectrum shows well-pronounced level clustering for the ratios $\omega_y : \omega_x = n : 1, n \in \mathcal{N}^*$. The energy gaps between the clusters of levels for $n \geq 3$ are however smaller, compared to those for $n = 2$. The observed clustering might give rise to the expectation that the corresponding configurations are candidates for integrability. Figure 6.13(a)-(c) shows the PSOS for the angles corresponding to $n = 3, 4, 5$.

For $n = 3, 4, 5$ the phase space is dominated by large elliptic regular islands and a dividing central layer of chaotic dynamics which increases with n. The corresponding quantum behavior shows a pronounced shell structure which weakens gradually with increasing n (Fig. 6.1(b)). In the figures of ELS for $n = 3$ and $n = 4$ (Fig. 6.14) the non-interacting system shows the expected behavior of clusters with degenerate levels, separated by equidistant energy gaps, the width of which decreases with increasing n. The introduction of the anisotropy causes the lifting of the degeneracies leading to the characteristic energetical stretching phases, similar to the ones observed in the ELS for $n = 1$ and $n = 2$. Additionally there is an overall decay superimposed on the oscillatory multi-mode stretching phases.

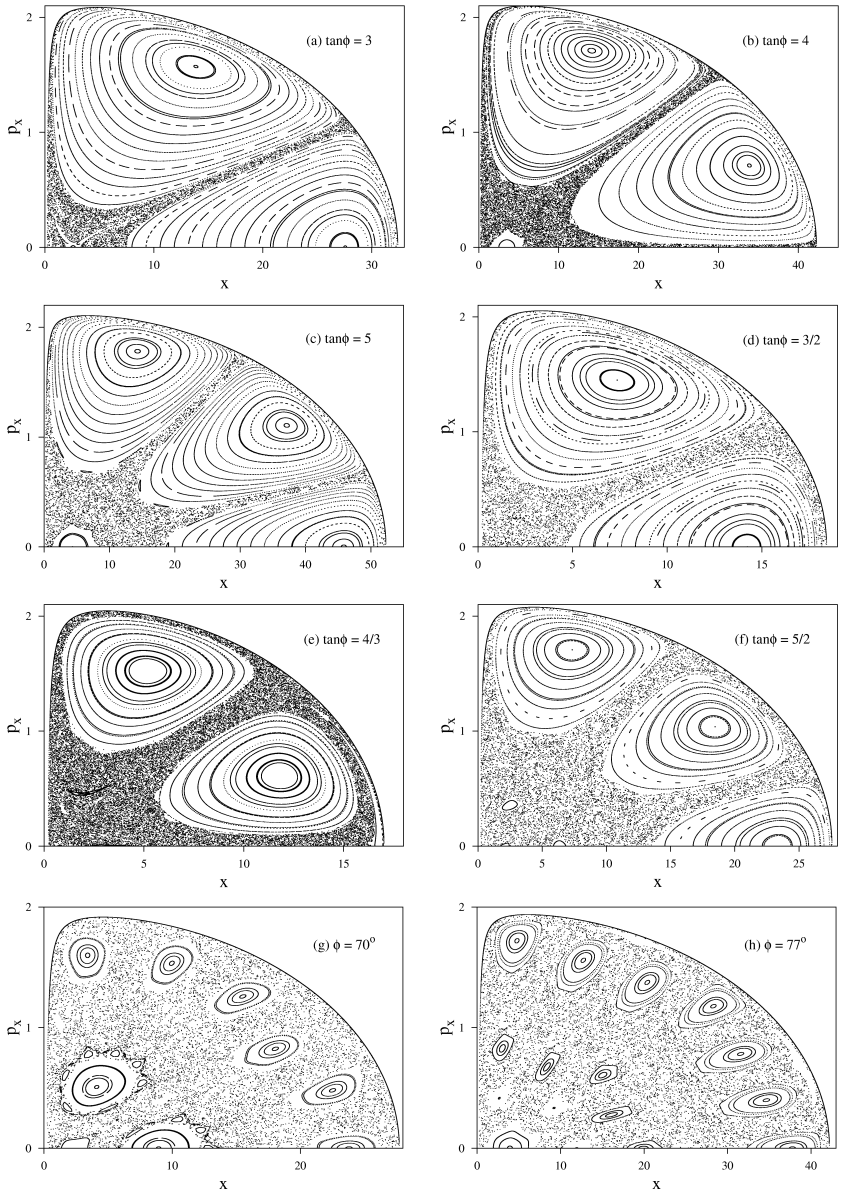

Figure 6.13: Phase space (x, p_x for $y = 0$) for various anisotropies and energies. Subfigures (a) - (e) correspond to energy $E = 55$ meV and (f),(g) to energy $E = 47$ meV.

For ratios $\omega_y : \omega_x = n : p$, $n, p > 1$ the spectra, for relatively small integers n, p, shows in the case of the non-interacting system again level clustering. This feature is apparent in Fig. 6.1(b) and also in the structure of the corresponding ELS drawn in Fig. 6.14 for the case $n = 3$, $p = 2$. When we turn on interaction the energy gaps reduce, thereby almost eliminating the shell structure (see Fig. 6.1(b) for the cases $n = 3$, $p = 2$ and $n = 4$, $p = 3$). However, the energy gaps, although smaller, 'perform' oscillations (Fig. 6.14).

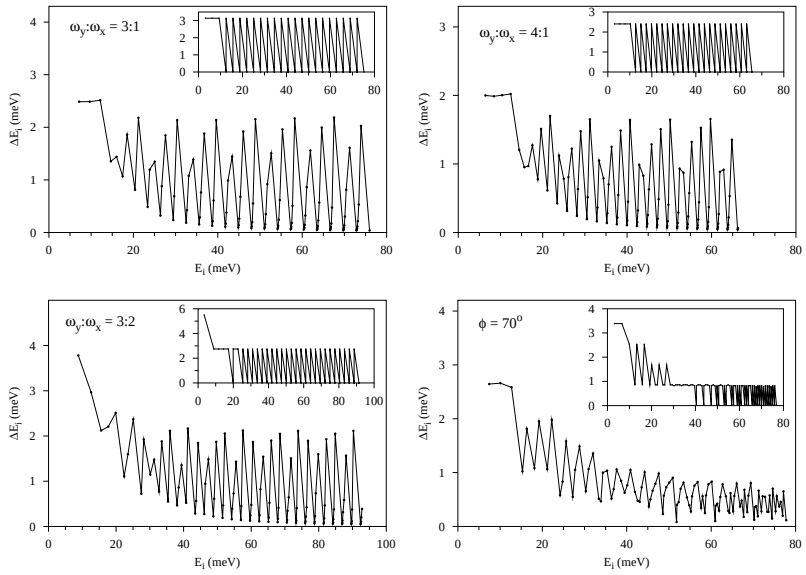

Figure 6.14: ELS $\Delta E_i(E_i)$ for the non-interacting (inset) and interacting system, for the first 100 states with $(++)$ symmetry in the cases $\omega_y : \omega_x = 3, 4, 3/2, 2.747...$

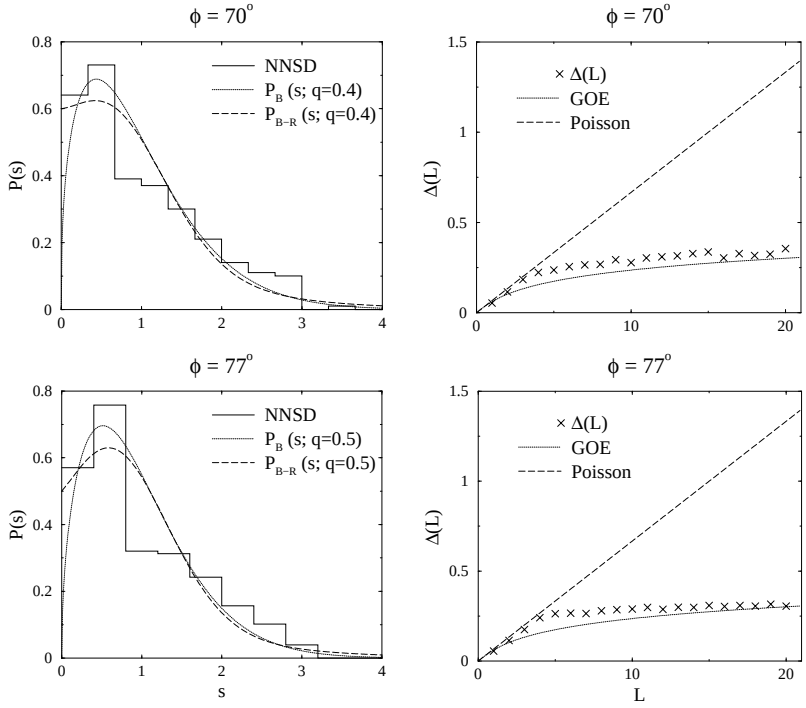

Figure 6.15: Statistical measures NNSD (left column) and spectral rigidity $\Delta(L)$ (right column) for the angles $\phi = 70°$ and $77°$. The spectral sequences $\{E_i\}$ correspond to sets of converged states with $(++)$ symmetry.

The classical counterpart shows a mixed phase space (Fig. 6.13(d)-(f)) of which the chaotic

portion increases with increasing the integer values n, p. The PSOS for higher irrational frequency ratios is shown in Fig. 6.13(g), (h) for the angles $\phi = 70^\circ$ and 77°. The profile of the ELS (Fig. 6.14 for $\phi = 70^\circ$) is irregular and remarkably, shows an evolutionary pattern with increasing energy: apart from the overall decay of the envelope, we observe beats which finally dissolve and provide an irregular behavior.

In the cases of the irrational frequency ratios $\phi = 70^\circ$ and 77° we applied the statistical measures NNSD and SR to the corresponding unfolded spectra (see Fig. 6.15). The fraction of chaos in the PSOS varied for both cases between 70% and 40% for energies between 50 meV and 130 meV where the spectral sequences $\{E_i\}$ converged. Deviations from the theoretical models used for fitting the NNS data are again a major feature, although the fittings using the BD are in general better than, in particular, the case of the weak anisotropies. The spectral rigidity follows a line close to the prediction by the GOE ensemble.

6.3.5 Wire-like dot

The physical picture of this case consists of a very weak confinement along the x- direction and a very strong one along the y-direction ($\omega_x \to 0$, $\omega_y \to \omega_o$). In this limit the Coulomb force plays an essential role for the motion along the x-axis. This phase in the electronic matter is the so called Wigner crystallization in which the electrostatic Coulomb repulsion dominates and localizes electrons in positions that minimize Coulomb repulsion, thereby almost defining the ground state of the system. In this limiting phase, the electrons tend to behave classically and therefore the classical to quantum correspondence of the electronic properties are of particular interest. When we move to higher ϕ in the confinement space, approaching 90°, a ballistic channel along the x-axis opens. Hence, we now have a quantum quasi-wire since the electrons experience intermittently (see below) quasi-free and strongly interacting phases of motion.

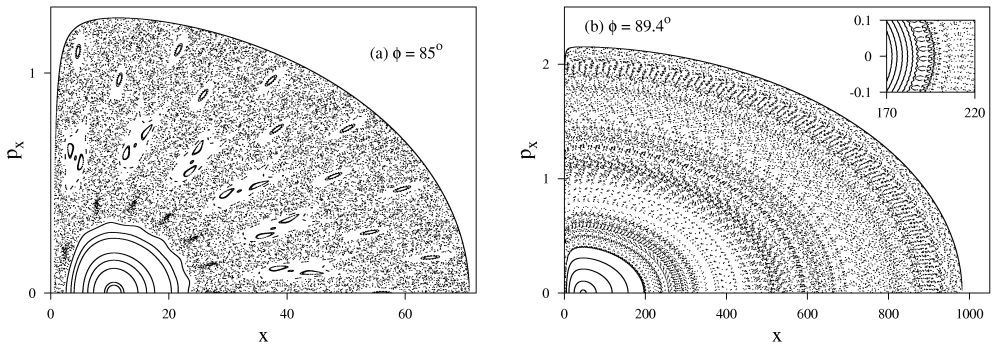

Figure 6.16: PSOS (x, p_x for $y = 0$) for two cases of the wire-like dot, for energy $E = 20$ meV. Subfigure (a) corresponds to the angle $\phi = 85^\circ$ ($\omega_y : \omega_x \approx 11.43$) and (b) to the angle $\phi = 89.4^\circ$ ($\omega_y : \omega_x \approx 95.5$).

Figure 6.16 shows the PSOS for the cases $\phi = 85^\circ$ ($\frac{\omega_y}{\omega_x} \approx 11.43$) and $\phi = 89.4^\circ$ ($\frac{\omega_y}{\omega_x} \approx$

95.5) of the wire-like dot. For $\phi = 85°$, apart from the central regular region, the phase space is dominated by chaos with a large number of small regular islands surviving in it. For very strong anisotropies $\phi = 89.4°$ the PSOS shows a comparatively small central regular region while the biggest part is dominated by a 'distorted pattern' which corresponds to intermittent dynamics. The dynamics within the regular islands is that of a simple harmonic oscillator slightly perturbed by the Coulomb interaction. The mechanism responsible for the 'distorted pattern' in the chaotic part of the phase space is the following. The two electrons are well-separated for long time periods, performing an oscillatory motion. Almost periodically, with an approximate period $T = \frac{2\pi}{\omega_x}$, the electrons come in close proximity and the Coulomb repulsion causes a sudden momentum transfer of varying magnitude. The latter depends on the dynamics, i.e. on the detailed collisional approach of the electrons. The observed pattern is therefore the result of the harmonic oscillator motion combined with Coulomb scattering events, which shift the otherwise regularly arranged points on the PSOS. The inset in Fig. 6.16(b) shows the transition from the regular islands to the chaotic sea.

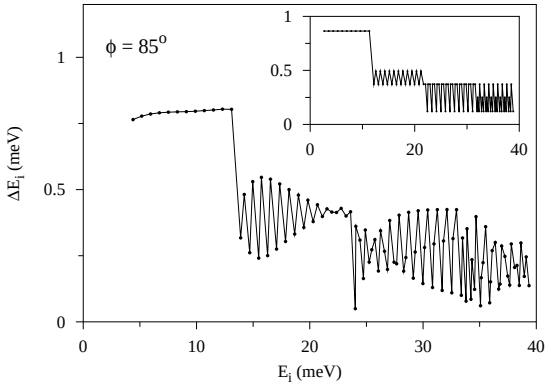

Figure 6.17: ELS $\Delta E_i(E_i)$ for the non-interacting (inset) and interacting system, for the first 100 states with $(++)$ symmetry and $\phi = 85°$.

Figure 6.17 shows the ELS of the quantum system for $\phi = 85°$. It shows remarkable patterns with increasing energy. We observe essentially two eyecatching beats separated by an abrupt transition ($E \sim 23$ meV) that take place on different scales of the energy spacing. After the second beat a transition to an irregular sequence of spacings is observed for high energies $E_i > 35$ meV.

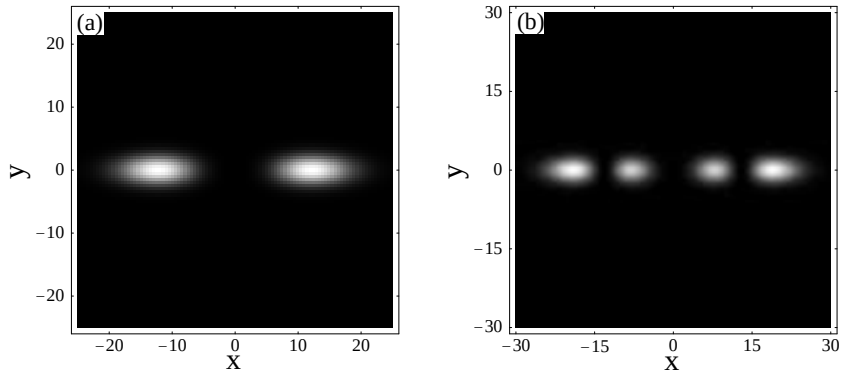

Figure 6.18: Density plot of the square of the absolute value of the two-electron wave function in the quantum dot for strong anisotropy $\phi = 85°$ ($\omega_y : \omega_x \approx 11.43$) for (a) the singlet ground state and (b) the first excited singlet state (dark regions correspond to low and the bright ones to high densities).

Figure 6.18 shows charge density plots for the ground and the first excited singlet state. The electrons localize along the x-axis in well separated positions due to the dominating Coulomb repulsion force.

6.4 Conclusions

In this chapter we have presented a review on the effects of the interaction and anisotropy of two-electron quantum dots from both a dynamical and quantum mechanical point of view. Notably, the employed Hamiltonian is of fundamental interest and equally describes the situation of two ions harmonically confined in traps created by external fields.

We briefly summarize our results. For a quantum dot with isotrpoipc parabolic confinement the spectrum shows groups of energy levels which belong either to spin singlet or to spin triplet symmetry. The Hamiltonian is integrable and the constant of motion being the angular momentum L_z. The levels are non degenerate ($m = 0$) or doubly ($m \neq 0$) degenerate. The introduction of an anisotropy in the interacting system serves as a rapid path to classical chaos, with a severe impact on the quantum spectrum. The level clusters widen and finally overlap and interact obeying, for the pure symmetry spectrum, the non-crossing rule. For the anisotropic configurations $\omega_y : \omega_x = n : 1$ ($n \geq 2$) we again observe level clustering being most pronounced for the case $n = 2$. For the latter configuration the system is despite the interaction integrable. Parity properties of the quantum operator responsible for the integrability result in eigenvalues which for $\lambda \neq 0$, pair in singlet - triplet degenerate subspaces with respect to the x-parity. This symmetry property together with the fact that singlet and triplet states are degenerate, makes the $2 : 1$ configuration unique. For $\omega_y : \omega_x = n : 1$, $n \geq 3$ the shell structure weakens with increasing n. The underlying classical dynamics acquires an increasing portion of chaotic dynamics with increasing n, i.e. changes 'slowly' from integrability to completely mixed phase space. The configurations $\omega_y : \omega_x = n : p$, for

relatively small n, p, still show traces of a shell structure. Standard statistical measures such as NNSD and SR have been applied to certain cases for the whole range of the spectrum. The observed major deviations from the theoretical predictions, where the regular structures in the PSOS dominated, have been assigned to the non-generic nature of the underlying integrable system. In the extreme case $\phi \to 90^\circ$ the wire-like dot represents a paradigm for the transition to Wigner crystallization: the classical dynamics comprises the complete regime from softly interacting to kicked oscillators. The level spacing shows two major beats i.e. remarkable patterns, which do not occur for the non-interacting counterpart, indicating the importance of the Coulomb scattering events in this regime.

Chapter 7

Two-electron anisotropic quantum dots in homogeneous magnetic field

7.1 Introduction

In this chapter, a detailed investigation of the combined effects due to the electronic interaction, anisotropy and the magnetic field on two-electron quantum dots with harmonic confinement will be performed. The electronic level structure, in particular the low-lying excitation spectrum, will be studied with varying field strength and anisotropy by employing an "exact" numerical diagonalisation approach. In addition to this, the magnetisation of the dot will be derived for the complete deformation regime ranging from weak to strong fields. The energetic spacing between the energy levels is comparable to the energetic contribution due to the spin Zeeman term and therefore both cases without and with inclusion of the spin Zeeman interaction will be considered. The latter corresponds to a GaAs semiconductor. The ground state exhibits parity oscillations which depend both on the magnetic field strength as well as on the anisotropy. Therefore the shape of the dot can be mapped on experimental measurements since these oscillations are esaily identified experimentally. Finally, the classical dynamics of the interacting electrons will be studied, exhibiting near integrability for field strengths leading to ratios $\omega_1 : \omega_2 = 1 : n$.

The chapter is organised as follows. In Section 7.2, we provide the Hamiltonian of the electronic motion and discuss its general symmetries. In Section 7.3, we introduce our basis set and present the computational approach. Section 7.4 contains our results. In particular, the low-lying spectrum in a magnetic field and the magnetisation are investigated for the full deformation regime from circularly symmetric to wirelike dots. The results are discussed also in the presence of the Zeeman splitting term. Moreover, the dynamics for a specific deformation is studied with changing magnetic field and is linked to the single-particle picture. Finally, in Section 7.5, we summarize the results of our research.

7.2 Hamiltonian and general symmetries

The conduction band electrons confined in a two-dimensional anisotropic harmonic quantum dot in a magnetic field $\mathbf{B} = (0, 0, B)$, within the framework of the effective mass approximation, are described by the Hamiltonian $\mathcal{H} = \mathcal{H}_{CM} + \mathcal{H}_r$ with

$$\mathcal{H}_{CM} = \frac{1}{4m_e}(\mathbf{P} + 2e\mathbf{A}(\mathbf{R}))^2 + m_e\omega_o^2\left(cos^2\phi\, X^2 + sin^2\phi\, Y^2\right) \tag{7.1}$$

$$\mathcal{H}_r = \frac{1}{m_e}(\mathbf{p} + \frac{e}{2}\mathbf{A}(\mathbf{r}))^2 + \frac{m_e}{4}\omega_o^2\left(cos^2\phi\, x^2 + sin^2\phi\, y^2\right) + \frac{e^2}{4\pi\epsilon\epsilon_o\,|\mathbf{r}|} \tag{7.2}$$

Due to the harmonic confinement the center of mass (CM) and internal motion separate. For the vector potential we choose the symmetric gauge **A(r)** = $\frac{1}{2}$ (**B** $\times$ **r**). The constants $e, m_e, \epsilon, \omega_o, \phi$ are the electron charge, effective mass, dielectric constant, the characteristic frequency and the anisotropy parameter, respectively. Small and capital letters correspond to the relative and center of mass degrees of freedom, respectively. In the following we focus on the non-trivial part $\mathcal{H}_r$, describing the relative motion, for the reasons discussed in chapter 6. Parity ($\mathbf{r} \to -\mathbf{r}$) and spin are interrelated symmetries due to the Pauli exclusion principle and we encounter spin singlet eigenfunctions with even spatial symmetry $\Psi(\mathbf{r}) = \Psi(-\mathbf{r})$ and spin triplet eigenfunctions with odd spatial symmetry $\Psi(\mathbf{r}) = -\Psi(-\mathbf{r})$.

In order to simplify our Hamiltonian, we apply a canonical transformation: $x = lx'$, $y = ly'$, $p_x = p'_x/l$ and $p_y = p'_y/l$ thereby scaling $\mathcal{H}_r$ into a dimensionless one, via $\mathcal{H}_r = \frac{\hbar^2}{m_e l^2}\mathcal{H}'_r$. In the following we adopt the typical values for a GaAs dot and the scaling yields the effective Bohr radius $l = a_B^* = 9.8$ nm, the effective Hartree $Ha^* = 11.8$ meV and 1 effective unit (e.u.) of field strength corresponds to 6.925 Tesla. The artificial (electrostatic) confinement has the characteristic frequency $\hbar\omega_o = 4.96$ meV. This scaling yields the following expression for the dimensionless Hamiltonian of the relative motion (the primes have been dropped for simplicity),

$$\begin{aligned}\mathcal{H}_r &= -\frac{\partial^2}{\partial x^2} - \frac{\partial^2}{\partial y^2} - i\frac{B}{2}\left(x\frac{\partial}{\partial y} - y\frac{\partial}{\partial x}\right) + \frac{1}{4}\left(\frac{B^2}{4} + \omega_x^2\right)x^2 \\ &+ \frac{1}{4}\left(\frac{B^2}{4} + \omega_y^2\right)y^2 + \frac{1}{\sqrt{x^2+y^2}}\end{aligned} \tag{7.3}$$

The two characteristic frequencies of the confinement are $\omega_x = \omega_o\, cos\phi$ and $\omega_y = \omega_o\, sin\phi$. For $\phi = 45°$ the dot has a circular shape. With increasing ϕ it deforms to an elliptic shape and approaches a wirelike dot for $\phi \to 90°$ ($\omega_x \to 0$, $\omega_y \to \omega_o$).

The spin of the two electrons gives an additional contribution to the energy, i.e., the Zeeman term,

$$E_S(B) = g^* \mu_B B S_z \tag{7.4}$$

with μ_B being the Bohr magneton and $g^* = -0.44$ the effective Landé factor for GaAs. E_S splits the threefold degeneracy of the spin triplet states while the energies of the spin singlet states remain unchanged.

7.3 Computational Approach

To investigate the two-electron QD, we solve the corresponding Schrödinger equation using a full configuration interaction (CI) approach with the anisotropic harmonic oscillator basis set

$$\Phi_{n_x n_y} = A(n_x, n_y) H_{n_x}(\sqrt{c_1}\, x) H_{n_y}(\sqrt{c_3}\, y) e^{-\frac{c_1}{2}x^2 - \frac{c_3}{2}y^2 + i(\lambda - \frac{c_2}{2})xy} \tag{7.5}$$

leading to an algebraic eigenvalue problem. In Eq. (7.5) $A(n_x, n_y)$ is the normalization constant, $c_1 = M_1\omega_1/c$, $c_3 = M_2\omega_2/c$, $c_2 = 2\mu M_1\omega_1 M_2\omega_2/c$, $c = \mu^2 M_1 M_2 \omega_1\omega_2 + 1$, $\mu = -2L/(m_e\omega_0 p)$, $\lambda = [m_e\omega_0 L(2+L^2)]/[4(cos(2\phi) - p)]$, $M_{1,2} = m_e p/(p - cos(2\phi) \mp L^2)$, $\omega_{1,2} = (\omega_0/\sqrt{2})\sqrt{1 + L^2 \mp p}$, $L = eB/m_e\omega_0$ and $p = \sqrt{(1+L^2)^2 - sin^2(2\phi)}$. All the units are scaled appropriately. The argumentation for the choice of these orbitals is the following. The single-particle anisotropic harmonic oscillator in a magnetic field, described by the Hamiltonian (7.3) without the Coulomb interaction term, can be transformed unitarily such that we arrive at a Hamiltonian for two independent oscillators in their individual one-dimensional harmonic potentials [140]:

$$\mathcal{H} = \frac{p_1^2}{2M_1} + \frac{p_2^2}{2M_2} + \frac{1}{2}M_1\omega_1^2 x^2 + \frac{1}{2}M_2\omega_2^2 y^2 \tag{7.6}$$

with eigenvalues $E_{n_1,n_2} = (n_1 + \frac{1}{2})\hbar\omega_1 + (n_2 + \frac{1}{2})\hbar\omega_2$ and eigenfunctions of the form,

$$\begin{aligned} \Psi_{n_1 n_2} &= N_{n_1,n_2} e^{-\frac{c_1}{2}x^2 - \frac{c_3}{2}y^2 + i(\lambda - \frac{c_2}{2})xy} \\ &\times \sum_{k=0}^{n_1}\sum_{l=0}^{n_2} c_{kl}(n_1, n_2) H_{n_1-k}(\alpha_1 x + \beta_1 y) H_{n_2-l}(\alpha_2 x + \beta_2 y) \end{aligned} \tag{7.7}$$

The exponential part in $\Psi_{n_1 n_2}$ is exactly contained in our basis set (see equations (7.5) and (7.7)). The analytical expressions for the coefficients $c_{kl}(n_1, n_2)$, α_1, β_1, α_2, β_2 in equation (7.7) can be found in Ref. [140]. The Hermite polynomials $H_{n_1-k}(\alpha_1 x + \beta_1 y)$ and

$H_{n_2-l}(\alpha_2 x + \beta_2 y)$ in equation (7.7) can be equally described by the Hermite polynomials of our basis set in equation (7.5). The corresponding relation is given by [141],

$$H_{n_1-k}(\alpha_1 x + \beta_1 y) = \frac{1}{\sqrt{2^{n_1-k}}} \sum_{i=0}^{n_1-k} H_{n_1-k-i}(\sqrt{2}\alpha_1 x) H_i(\sqrt{2}\beta_1 y)$$

Therefore, in order to describe exactly the eigenstate $\Psi_{n_1 n_2}$ with our basis set, we need to superimpose Hermite polynomials of equation (7.5) up to maximal order $n_x = n_y = n_1 + n_2$.

The next step is the evaluation of the Hamiltonian matrix belonging to equation (7.3). For this purpose, we firstly find a Hamiltonian which can be diagonalised exactly and then subtract it from $\mathcal{H}_r$. To proceed, we write the orbitals, $\Phi_{n_x n_y} = \tilde{\Phi}_{n_x n_y}\mathcal{P}$ where $\mathcal{P} = exp(i(\lambda - \frac{c_2}{2})xy)$ is the phase and $\tilde{\Phi}_{n_x n_y}$ are the eigenfunctions of the dimensionless scaled Hamiltonian,

$$\tilde{\mathcal{H}}_0 = -\frac{1}{2}\frac{\partial^2}{\partial x^2} - \frac{1}{2}\frac{\partial^2}{\partial y^2} + \frac{1}{2}c_1^2 x^2 + \frac{1}{2}c_3^2 y^2$$

with eigenvalues $\tilde{\varepsilon}_{n_x n_y} = (n_x + \frac{1}{2})\hbar c_1 + (n_y + \frac{1}{2})\hbar c_3$. To implement the phase we proceed as follows,

$$\tilde{\mathcal{H}}_0 \tilde{\Phi}_{n_x n_y} = \tilde{\varepsilon}_{n_x n_y} \tilde{\Phi}_{n_x n_y} \Rightarrow \mathcal{P}\tilde{\mathcal{H}}_0 \mathcal{P}^{-1} \mathcal{P}\tilde{\Phi}_{n_x n_y} = \tilde{\varepsilon}_{n_x n_y} \mathcal{P}\tilde{\Phi}_{n_x n_y} \Rightarrow$$

$$\mathcal{H}_0 \Phi_{n_x n_y} = \tilde{\varepsilon}_{n_x n_y} \Phi_{n_x n_y}$$

where $\mathcal{H}_0 = \mathcal{P}\tilde{\mathcal{H}}_0\mathcal{P}^{-1}$ is diagonal in the basis $\Phi_{n_x n_y}$. For our QD we have to consider the Hamiltonian $\mathcal{H}_1 = 2\mathcal{H}_0$, with eigenvalues $\eta_{n_x n_y} = 2\tilde{\varepsilon}_{n_x n_y}$, which takes the explicit form,

$$\begin{aligned}\mathcal{H}_1 = \quad & -\tfrac{\partial^2}{\partial x^2} - \tfrac{\partial^2}{\partial y^2} + 2i\left(\lambda - \tfrac{c_2}{2}\right)\left(x\tfrac{\partial}{\partial y} + y\tfrac{\partial}{\partial x}\right) \\ & + \left[\left(\lambda - \tfrac{c_2}{2}\right)^2 + c_1^2\right] x^2 + \left[\left(\lambda - \tfrac{c_2}{2}\right)^2 + c_3^2\right] y^2\end{aligned}$$

The dimensionless Hamiltonian of the relative motion $\mathcal{H}_r$ can be summarized as,

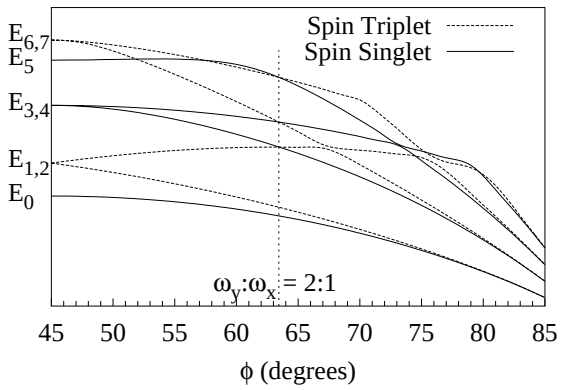

Figure 7.1: Schematic diagram of the energy of the ground and first seven excited states for $B = 0$ with increasing ϕ. The vertical line indicates the angle for which the system is integrable.

$$\begin{aligned}
\mathcal{H}_r &= (\mathcal{H}_r - \mathcal{H}_1) + \mathcal{H}_1 \\
&= -i\left[-\frac{B}{2} + 2\left(\lambda - \frac{c_2}{2}\right)\right] y\frac{\partial}{\partial x} - i\left[\frac{B}{2} + 2\left(\lambda - \frac{c_2}{2}\right)\right] x\frac{\partial}{\partial y} \\
&+ \left[\frac{B^2}{16} + \frac{\omega_x^2}{4} - \left(\lambda - \frac{c_2}{2}\right)^2 - c_1^2\right] x^2 \\
&+ \left[\frac{B^2}{16} + \frac{\omega_y^2}{4} - \left(\lambda - \frac{c_2}{2}\right)^2 - c_3^2\right] y^2 + \frac{1}{\sqrt{x^2+y^2}} + \mathcal{H}_1 \qquad (7.8)
\end{aligned}$$

The eigenvalues $\eta_{n_x n_y}$ will be contained in the diagonal elements of the Hamiltonian matrix. The matrix elements due to the contribution of the first four terms in equation (7.8) can be calculated in a straightforward analytical form. The matrix elements due to the Coulomb repulsion have to be evaluated numerically with the method presented in appendix A.

7.4 Results and Discussion

7.4.1 No magnetic field

The starting point of our analysis is the two-electron anisotropic quantum dot without magnetic field, which has been studied in detail in chapter 6. Figure 7.1 presents the low-lying spectrum of $\mathcal{H}_r(B = 0)$ as function of the anisotropy ϕ. The energy eigenstates follow (with increasing energy) the symmetries: $(m; S)$ = $(0; 0)$,$(\pm 1; 1)$, $(\pm 2; 0)$,$(0; 0)$,$(\pm 3; 1)$,$(\pm 1; 1)$,. . ., where m and S are the magnetic quantum number and the total spin, respectively. The introduction of the anisotropy splits the degeneracies and leads to spin singlet - triplet (ST) crossings. At $\omega_y : \omega_x = 2 : 1$, $\mathcal{H}_r(B = 0)$ becomes integrable and due to the symmetry

of its constant of motion Λ, the eigenstates of the Hamiltonian are pairwise degenerate with identical x-parity. For $\phi \to 90°$ the eigenstates converge to energetically well-separated pairs of spin singlet and and spin triplet states.

7.4.2 Spectrum and magnetisation for $g^* = 0$ in a magnetic field

Before investigating the general situation of our interacting anisotropic QD in a magnetic field let us briefly address, the effect of the magnetic field in the interacting isotropic case, which possesses particular analytical solutions [118, 128]. L_z is a constant of motion and the system is integrable. As stated in the introduction, increasing the magnetic field strength leads to a ground state for the system that changes its spin symmetry, i.e., the well-known ground state ST oscillations [81]. The symmetries of the ground state with increasing magnetic field strength are as follows: $(m; S)$ = (0; 0),(−1; 1),(−2; 0),(−3; 1),. . .. With increasing field strength, the energy spacing between two neighbouring levels $\Delta E_i = E_{i+1} - E_i$ (*i* determines the degree of excitation and takes even values $i = 0, 2, 4$ within our study) oscillates between zero (at the ST crossing of the states with energies E_i and E_{i+1}) and a maximum amplitude ΔE_{max}. For strong external fields ΔE_{max} reduces and the energy curves of the ground and first excited state have a slope approaching the same constant value. A quantity to measure this event is the magnetisation, which, at zero temperature, is defined as $M(B) = -(\frac{\partial E_0}{\partial B})$, where E_0 is the energy of the ground state. Hence, the ST crossings are apparent as steps in the magnetisation curve whose size decreases for strong magnetic fields (see figure 3 for $\phi = 45°$).

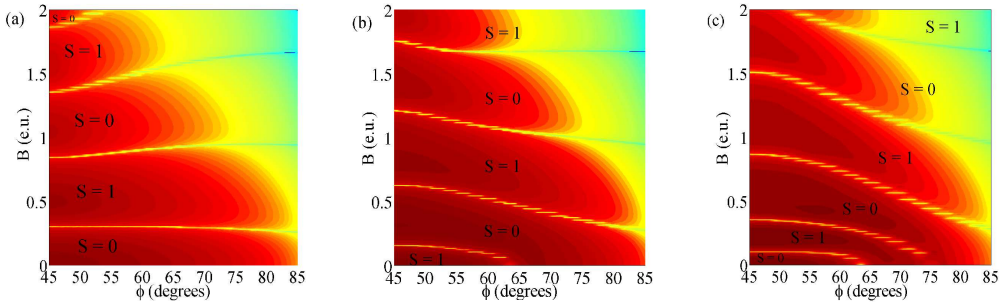

Figure 7.2: Domains of spin multiplicity in the (B, ϕ) plane for (a) the ground state, (b) the second excited state and (c) the fourth excited state. Brightness indicates the energy difference ΔE_0, ΔE_2 and ΔE_4, respectively, on a logarithmic scale. Dark and bright regions correspond to large and small spacings, respectively. The bright curves form the borders between the different ST-symmetry domains.

Introduction of the anisotropy breaks the rotational symmetry of the system and a large number of avoided crossings between the energy curves of states possessing identical symmetry occurs. For $B = 0$ the level spacing ΔE_0 will decrease with increasing deformation (see Figure 7.1). Figure 7.2(a) shows the spin multiplicity $S = 0, 1$ of the ground state in

the (B, ϕ) plane. For $\phi = 45°$ we observe the ST ground state oscillations, discussed above. With increasing deformation we observe a robustness of the first ST crossing, i.e., the curve $B(\phi)$ where the first ST crossing occurs is approximately independent of ϕ. For higher magnetic fields the domains corresponding to different spin multiplicity widen smoothly with increasing deformation and the corresponding curves $B(\phi)$ show a significant positive slope $\frac{dB}{d\phi}$. As a result the fifth domain $S = 0$ is suppressed for $\phi \gtrsim 54°$ in the range of the calculated magnetic field strengths.

Figure 7.2(b) shows the spin multiplicity domains for the second excited state (E_2) in the (B, ϕ) plane. For $B = 0$ this state is a spin triplet state and at $\omega_y : \omega_x = 2 : 1$ it becomes degenerate with the spin singlet state corresponding to the energy E_3 (see Figure 7.1 and discussion in subsection 4.1 for further details). For larger ϕ the state with energy E_2 is a spin singlet. The border curve corresponding to the first ST crossover for relatively weak magnetic fields stops at $\omega_y : \omega_x = 2 : 1$ at $B = 0$. The following border curves for stronger fields show a negative slope and the different symmetry domains slightly widen for stronger anisotropies $\omega_y : \omega_x > 2 : 1$.

The fourth excited state (E_4) shows an even stronger dependence of its spin multiplicity islands on B and ϕ. Figure 7.2(c) shows the spin symmetry domains for the fourth excited state. Initially it is a spin singlet and after $\omega_y : \omega_x = 2 : 1$ it becomes a spin triplet due to a ST crossing as expected. For stronger anisotropies and due to the higher number of excited states involved in the spectrum, at $\phi \approx 75°$ an 'accidental' crossing occurs and the fourth excited state restores its initial parity. The first boundary curve $B(\phi)$ is suppressed at $\phi \approx 63.4°$ ($\omega_y : \omega_x = 2 : 1$) and the second one at $\phi \approx 75°$ as a result of the above discussed behaviour. For higher field strengths, the corresponding spin multiplicity domains and border curves show an even stronger dependence on ϕ than the one observed for the second excited state.

Another complementary measure in order to study the separate implications of the magnetic field and deformation on the ground state is the magnetisation M. It has been shown that for three and four electrons M depends on both anisotropy and number of electrons [111]. Figure 7.3 shows the magnetisation for various anisotropies corresponding to the full deformation regime. For $\phi = 45°$ the steps are more pronounced than for any anisotropy. With increasing ϕ the overall behaviour of $\Delta E_0(B)$ leads to a decrease of the steps in the magnetisation signal, despite the fact that the ST oscillations are present according to Figure 7.2(a). Hence, at $\phi \gtrsim 54°$ the fourth step is eliminated as predicted by figure 7.2(a) but also the third step is no more visible on the scale of figure 3 for $\phi \gtrsim 54°$, the second step disappears for $\phi \gtrsim 70°$ and the first one disappears for $\phi \gtrsim 81°$ resulting in a completely smooth behaviour for $\phi = 85°$.

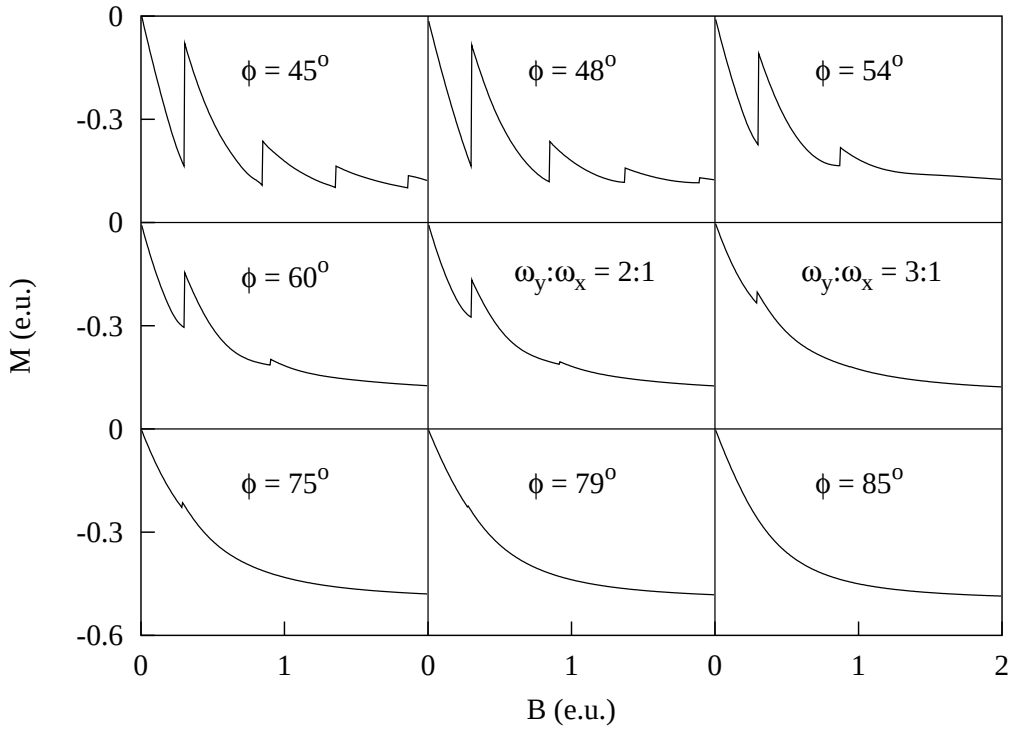

Figure 7.3: The magnetisation $M(B)$ for $g^* = 0$. The various panels correspond to anisotropies covering the full deformation regime.

7.4.3 Spectrum and magnetisation for $g^* = -0.44$

So far, in our discussion, we have neglected the contribution of the Zeeman term (given by Equation (7.4)) in the calculation of the spectrum. The Zeeman term E_S splits the threefold degeneracy of the spin triplet states while it leaves the spin singlet states unchanged. This additional splitting in the energy of the spin triplet states reduces the amplitude ΔE_{max} in the oscillations of the level spacing ΔE_0 and suppresses the ST oscillations in favour of the spin triplet symmetry. Figure 7.4(a) shows the spin multiplicity of the ground state in the presence of the Zeeman term. For $\phi = 45°$, despite the fact that the first ST oscillation survives preserving the first $S = 0$ domain, the second spin singlet domain is clearly reduced in comparison with figure 7.2(a) whereas the third $S = 0$ domain in figure 7.2(a) vanishes completely. The introduction of a deformation results in an elimination of the second spin singlet island for angles $\phi \gtrsim 48°$. The first $S = 0$ domain is preserved up to $\phi \approx 65°$ while for stronger anisotropies E_S dominates due the reduced level spacing $\Delta E_0(B = 0)$ and the $S = 0$ domain smoothly decreases in size with further increasing deformation ϕ.

Figure 7.4(b) and 7.4(c) show the ST oscillations for the second (E_2) and fourth (E_4) excited state in the (B,ϕ) plane respectively. It is clear that for lower fields, where E_S is negligible due to the small effective Landé factor of GaAs, the ST oscillations as described in Figure 7.2(b) and 7.2(c) persist with varying ϕ. For stronger external field (note that figures 7.4(b) and 7.4(c) cover only the weak to intermediate field regime $B \leq 0.9$ whereas

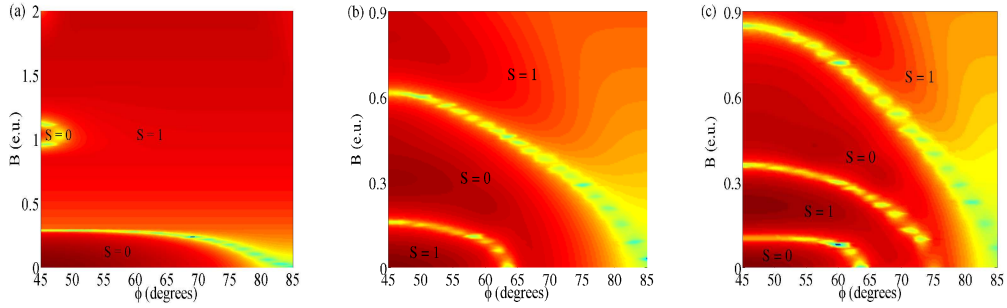

Figure 7.4: Domains of spin multiplicity in the (B, ϕ) plane for (a) the ground state, (b) the second excited state and (c) the fourth excited state in the presence of spin Zeeman splitting. Brightness indicates the energy difference ΔE_0, ΔE_2 and ΔE_4, respectively, on a logarithmic scale. Dark and bright regions correspond to large and small spacings, respectively. The bright curves form the borders between the different ST-symmetry domains.

figures 7.2 cover the range $B \leq 2.0$) the picture is rather complicated. This owes to the competition of the existing energy scales belonging to E_S and the level spacing as well as the large number of excited states involved in the formation of the spectrum. For a better illustration of our results, in figure 7.5 we present the low-lying spectrum for two different anisotropies corresponding to the intermediate ($\omega_y : \omega_x = 2 : 1$) and the wirelike ($\phi = 81°$) regime. In both pictures we observe the suppression of the spin singlet states in the ground state as reproduced in figure 7.4(a) (note that all spin-multiplet components are shown in figure 7.5). For higher excited states, in the regime of intermediate anisotropy we observe avoided crossings and the ST oscillations are preserved for the low field regime while in the wirelike case the pairing of the states leads to a rapid suppression of the spin singlet states in this extreme limit.

In order to complete our analysis for $g^* = -0.44$, we study the behaviour of the magnetisation. Figure 7.6 presents the magnetisation for various anisotropies. For $\phi = 45°$ we observe the first step remaining almost intact in the presence of E_S reflecting the robustness of the first $S = 0$ domain for the ground state energy. The next two steps are reduced in height and their location in terms of field strengths is changed significantly compared to $g^* = 0$, as expected from the discussion of figure 7.4(a). For $\phi \gtrsim 48°$ the second and third steps turn into a hill, due to the suppression of the spin singlet island, which gradually disappears with increasing anisotropy. The first step preserves its position up to $\phi \approx 65°$ while for stronger deformations it shifts towards smaller field strengths due to the competition of E_S and $\Delta E_0(B = 0)$ in the wirelike regime. For $\phi = 85°$ the magnetisation shows a completely smooth diamagnetic behaviour like the one for $g^* = 0$.

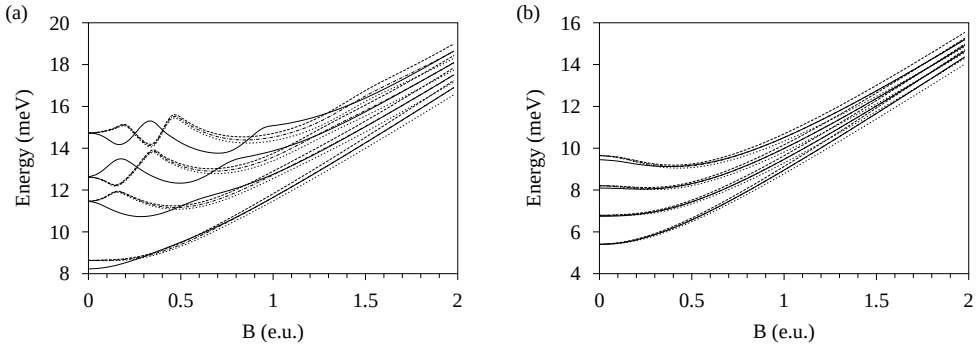

Figure 7.5: Low-lying spectrum for (a) $\omega_y : \omega_x = 2 : 1$ and (b) $\phi = 81°$. Full curves correspond to spin singlet symmetry while the dashed ones correspond to spin triplet symmetry with $S_z = \pm 1, 0$.

7.4.4 Dynamics

Before we investigate the dynamics of our interacting dot let us address some features of the single-particle system, i.e. the Hamiltonian (7.6) which describes the (diagonalised) anisotropic charged oscillator in a magnetic field. Its eigenvalues are $E_{n_1,n_2} = (n_1 + \frac{1}{2})\hbar\omega_1 + (n_2 + \frac{1}{2})\hbar\omega_2$. Figure 7.7(a) illustrates the single-particle spectrum at the anisotropic harmonic configuration $\omega_y : \omega_x = 2 : 1$ with varying field strength. For $B = 0$ we observe the energy gaps due to the $\left[\frac{N_0}{2} + 1\right]$-fold degeneracy (the brackets [] indicate the integer part of the enclosed number) of the energy levels where $N_0 = n_1 + 2n_2 = 0, 1, 2, \ldots$. For finite field strengths the degeneracies are lifted. For rational frequency ratios $\omega_1 : \omega_2 = 1 : n$, where $n \geq 3$ is integer, the energy levels become $\left[\frac{N_1}{n} + 1\right]$-fold degenerate where $N_1 = n_1 + nn_2 = 0, 1, 2, \ldots$. Hence, by varying the magnetic field we can tune the degeneracies of the single-particle spectrum as it has already been noted in reference [142]. The values of the field strengths for which we encounter $\omega_1 : \omega_2 = 1 : n$ are given by the expression,

$$B = \omega_0 \sqrt{sin2\phi \left(\frac{n^2 + 1}{2n}\right) - 1}$$

Table 7.1 contains the values of the field strength corresponding to $n = 3 - 10$. With increasing n the level spacing between two neighbouring degenerate manifolds reduces. In the high field limit the energy levels corresponding to states with $n_2 = 0$ cluster to form the lowest Landau level, the energies corresponding to $n_2 = 1$ the first excited Landau level etc (see figure 7.7(a) for large values of B). Another property of the single-particle degenerate manifolds is that those corresponding to odd n consist exclusively of states that have either even or odd parity, those corresponding to even n consist of both even and odd parity.

Let us now discuss the dynamics of the interacting system following the same path as before when studying the single-particle spectrum, i.e., starting with $\omega_y : \omega_x = 2 : 1$ and increasing B. The parameter characterising the dynamics is the fraction of regular phase

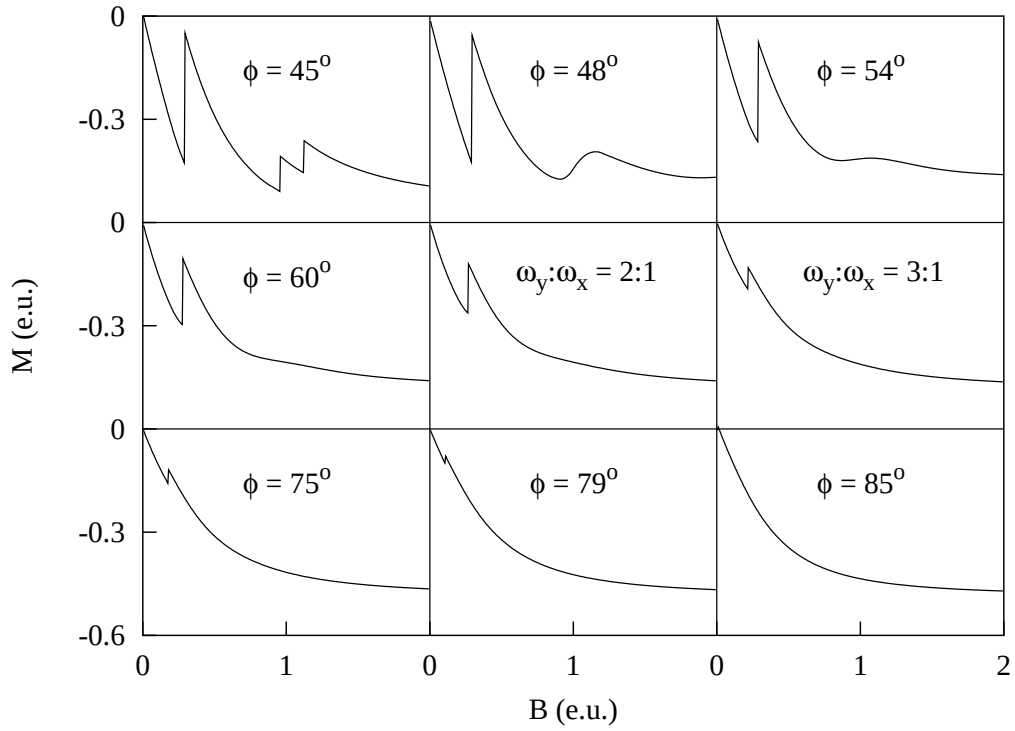

Figure 7.6: The magnetization $M(B)$ for $g^* = -0.44$. The various panels correspond to anisotropies covering the full deformation regime.

space defined as f = (Number of regular trajectories)/(Total number of trajectories). The criterion whether a trajectory is regular or chaotic is, of course, the finiteness of the Lyapounov exponent. Figure 7.7(b) shows f as a function of the magnetic field. For $B = 0$ the system, as discussed in subsection 4.1, is integrable and therefore $f = 1$. Introduction of the external field serves as a rapid path to chaos. Figure 7.7(c) shows a Poincaré Surface of Section (PSOS) for $B = 0.05$. It can be seen that even for such a weak field, the regularity is dramatically suppressed and the phase space is dominated by chaos. Further increasing the field strength we are led to an impressive peak for f at $B = 0.242487$. This field strength corresponds to the frequency ratio $\omega_1 : \omega_2 = 1 : 3$. The next major peak of $f(B)$ in figure 7.7(b) occurs at $\omega_1 : \omega_2 = 1 : 4$ and consequently at $\omega_1 : \omega_2 = 1 : n$ for $n \geq 5$. We observe, that the peaks of $f(B)$ corresponding to odd n are in general more pronounced than those corresponding to even n. However, both cases lead to a similar level clustering for the quantised system. Although we can not provide a thorough explanation for this, we remark that the states for a given cluster of levels corresponding to a frequency ratio with odd n possess the same parity (i.e., either spin - singlet or spin - triplet), while the states of a given cluster of levels corresponding to even n involve both parities (i.e., spin - singlet and spin - triplet). From this behaviour of f we conclude that interaction effects of the QD usually destroy the regularity of classical phase space, but at rational frequency ratios $\omega_1 : \omega_2 = 1 : n$ regularity still plays an important role and dominates the phase space (see also figure 7.7(d)

Table 7.1: Field strengths corresponding to the frequency ratios $\omega_1 : \omega_2 = 1 : n$ ($\hbar\omega_0 = 4.96$ meV, $\omega_y : \omega_x = 2 : 1$)

n	Magnetic field (e.u.)
3	0.242487
4	0.351397
5	0.436477
6	0.508645
7	0.572364
8	0.63
9	0.682993
10	0.732295

for $\omega_1 : \omega_2 = 1 : 3$). Of course, this behaviour is only well-pronounced for not too large values of n and the overall tendency of f with increasing field strength is to increase, finally leading to a dominant regular phase space for a very strong field (see figure 7.7(b) and 7.7(e) for $B = 2.0$). In this limit the magnetic interaction dominates and the anisotropic confinement due to the geometry of the dot is of perturbative character, i.e., we encounter an approximate rotational symmetry and we are close to integrability. For $B = 0$ and changing ϕ the property of dominant regular classical phase space at ratios $\omega_x : \omega_y = 1 : n$ reflects itself in the quantum behaviour of the dot as follows. The energy level degeneracies at the ratios $\omega_x : \omega_y = 1 : n$ for the non-interacting system are rather robust with respect to interaction effects in the sense that energy level clustering occurs at these ratios (for not too large n) if the interaction between the electrons is included [107, 108]. For finite magnetic field strengths the above-observed enhanced fraction of regularity in classical phase space for the ratios $\omega_1 : \omega_2 = 1 : n$ of the interacting system reflects itself also in the quantum spectrum, i.e., we encounter level clustering for higher excited states.

7.5 Conclusions

To conclude, we performed a detailed investigation of the effects of electronic interaction, anisotropy and magnetic field interaction in the electronic structure and dynamical properties of two-electron QDs with harmonic confinement. We have calculated the low-lying energy spectrum of the two-electron QD in a magnetic field for the full deformation regime from circular to wirelike dots. The calculation reveals the ground state ST oscillations for $\phi = 45°$ and their weak dependence on the anisotropy. Despite this robustness of the ground state ST oscillations the magnetisation is much more sensitive to the anisotropy in the sense that it smooths, i.e., it looses gradually its step-like structure with increasing ϕ. Furthermore,

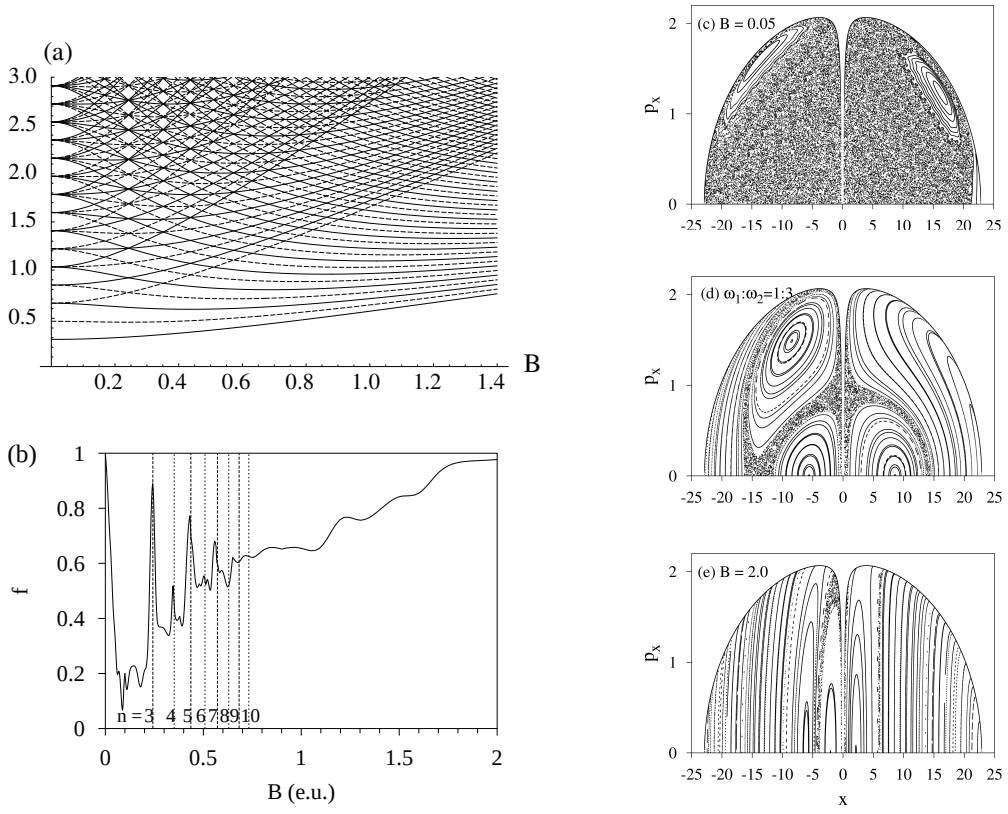

Figure 7.7: (a) Single-particle spectrum. Full curves correspond to states of even parity and dashed curves to states of odd parity, (b) fraction f of regular phase spase as a function of the magnetic field for the interacting dot and (c) - (e) Poincaré Surfaces of Section (x,p_x for $y = 0$ and $E = 55$ meV) for various magnetic fields ($\omega_y : \omega_x = 2 : 1$, $\hbar\omega_0 = 4.96$meV for all subfigures).

we study the excited states and reveal their ST oscillations which depend not only on the magnetic field but also significantly on the anisotropy. If we include the Zeeman splitting E_S contribution to the energy, the picture for the ground state ST oscillations changes as the spin singlet states are suppressed in favour of the spin triplet ones. The competition of the energy scales of E_S and ΔE_0 already for $\phi \gtrsim 48^\circ$ destroys the second spin singlet island yielding a bump in the magnetisation whereas the first spin singlet domain is eliminated with increasing ϕ. For higher excited states and intermediate field strengths the ST oscillations persist as shown for example for the second and fourth excited states. Finally, we have investigated the dynamics of the interacting system for the specific deformation $\omega_y : \omega_x = 2 : 1$. Despite the interaction, we find a phase space that is dominated by regularity for rational ratios $\omega_1 : \omega_2 = 1 : n$. For stronger field strengths the Hamiltonian acquires an approximate rotational symmetry and approaches integrability.

Chapter 8

Conclusions

We hope that the completion of this thesis leaves the reader with a feeling of satisfaction due to the wide range of phenomena that have been reported as well as with the question of what is going to happen next. With respect to the first comment we would like to remind the reader with the main stations of our journey. In the first two chapters, an introduction to the theory of linear quantum transport has been given and the parallel algorithm which has been developed for the necessary computations has been presented. We believe that these two chapters supply a short but rather deep and practical overview in this field. Many theoretical details which are beyond the scope of the present thesis have been commented with the necessary references in which they have been extensively analysed. Our journey continued with investigations of quantum magnetotransport through quantum dot arrays. These systems have proven to show sound fingerprints of their electronic band structure in their transport properties as well as substantial current flows for moderate magnetic fields. The latter have been "optimized" with respect to the semiconductor material, Fermi energy, geometry and temperature. We have shown therefore a nice paradigm of an electronic system which could serve as a potential application in nanoelectronics solely based on quantum features. In the second part of the thesis, we have discussed systems of quantum dots possessing tunneling barriers, which are high and thick enough such that these systems can be considered as practically isolated. In such systems the transport properties are defined from their electronic structure since interactions with the continuum bath due to the leads are negligible. We have investigated two electrons confined in a quantum dot. The response of their electronic spectrum with respect to an anisotropy in the artificial confinement potential as well as to an applied magnetic field has been discussed in detail. We have offered a global review of properties which extends from the quantum up to a classical point of view. The implementation of an efficient method for the evaluation of the two-electron integrals has offered access to a very large part of the excitation spectrum thereby allowing us to analyse them statistically. In addition to this we have discovered an a new two-dimensional integrable system and we have analytically derived the expression for its constant of motion. The application of the magnetic field causes an interplay of spin singlet - spin triplet (ST) symmetry of states,

the evolution of which has been investigated as a function of anisotropy for the low-lying spectrum. These ST oscillations which can be identified experimentally, could lead to a prediction of the type of the confinement to few-electron quantum dot experiments.

Regarding the second comment in the introductory sentence of our conclusions this has to do more with the expectations that have been cultivated throughout our journey. To stress the situation further with respect to the field of quantum transport we will borrow a comment from the epilogue of the book of S. Datta [2]. This comment refers to the present status of knowledge as only the “tip of the iceberg”, thereby implying that there is still a lot of research to be performed in order to obtain a more global view. This may require the development of novel theoretical approaches that take into account electronic correlations inside the scattering regions as well as inside the leads. Effects due to large applied source-drain voltage or electron-phonon interactions should equally be taken into account. During this journey, the available computational resources and numerical techniques should be rather flexible in order to adapt to the requested numerical problem. Architectures of parallel processors should play in this sense an important role for the successful and efficient implementation of the computations. In any case, we will agree that the research in this field is expected to be at least fascinating...

Appendix A

Efficient computation of the electron-electron integrals

A.1 Introduction

In this appendix, we are going to present the various numerical techniques that we have used in order to calculate the electron-electron integrals. The starting point in our evaluation is the Coulomb integral for our two-dimensional quantum dot which takes the general form,

$$I_{m_1,m_2,n_1,n_2} =< \Phi_{m_1,m_2} \mid \frac{1}{\sqrt{x^2+y^2}} \mid \Phi_{n_1,n_2} >= \frac{A_{m_1,m_2,n_1,n_2}}{\sqrt{\pi}} \tag{A.1}$$

$$\times \int_{-\infty}^{+\infty} dy \int_{-\infty}^{+\infty} dx H_{m_1}(\sqrt{c_1}\, x) H_{m_2}(\sqrt{c_3}\, y) H_{n_1}(\sqrt{c_1}\, y) H_{n_2}(\sqrt{c_3}\, x) \frac{e^{-c_1 x^2 - c_3 y^2}}{\sqrt{x^2+y^2}}$$

where the normalization constant,

$$A_{m_1,m_2,n_1,n_2} = \frac{\sqrt{c_1 c_3}}{\pi 2^{\frac{1}{2}(m_1+m_2+n_1 n_2)} \sqrt{m_1! m_2! n_1! n_2!}}$$

Our scope is to provide a rapid and accurate calculation of the Coulomb matrix elements for large values of the indeces m, n. The methods are divided in two categories: (i) analytical attempts using analytical expressions and/or employing reordering techniques and (ii) numerical techniques. The latter have provided an efficient, accurate and rapid evaluation of the electron - electron integrals. The results of the employed methods are presented separately in the according sections. At the end we discuss an overview of the employed methods in terms of the stability of our results.

A.2 Analytical expansion & reordering techniques

The corresponding integrals of eq. A.1 is possible to be evaluated analytically by using the properties of the Hermite polynomials [143] and standard integration tables [141]. The analytical result yields a fourfold series which can be summarised in equation A.2,

$$
\begin{aligned}
I_{m_1,m_2,n_1,n_2} = \quad & A'_{m_1,m_2,n_1,n_2} \sum_{k_1=0}^{[\frac{m_1}{2}]} \sum_{k_2=0}^{[\frac{m_2}{2}]} \sum_{l_1=0}^{[\frac{n_1}{2}]} \sum_{l_2=0}^{[\frac{n_2}{2}]} \frac{(-1)^{k_1+k_2+l_1+l_2}}{k_1!k_2!l_1!l_2!} \times \\
& \times \frac{2^{m_1+m_2+n_1+n_2-2(k_1+k_2+l_1+l_2)}}{(m_1-2k_1)!(m_2-2k_2)!(n_1-2l_1)!(n_2-2l_2)!} \times \\
& \times g_1(m_1,m_2,n_1,n_2,k_1,k_2,l_1,l_2)
\end{aligned}
\tag{A.2}
$$

where,

$$
\begin{aligned}
A'_{m_1,m_2,n_1,n_2} &= \frac{\sqrt{c_1}}{\pi\sqrt{\pi}2^{\frac{1}{2}(m_1+m_2+n_1n_2)}} \sqrt{m_1!m_2!n_1!n_2!} \\
g_1(m_1,m_2,n_1,n_2,k_1,k_2,l_1,l_2) &= (\frac{c_1}{c_3})^{a_1}\Gamma(\frac{a_1+1}{2})\Gamma(\frac{a_2+1}{2})B(\frac{a_1+a_2+1}{2},\frac{1}{2}) \times \\
& \quad {}_2F_1(\frac{a_1+1}{2};\frac{a_1+a_2+1}{2};\frac{a_1+a_2}{2}+1;1-\frac{c_1}{c_3})
\end{aligned}
$$

The constants $a_1 = m_1 + n_1 - 2(k_1 + l_1)$, $a_2 = m_2 + n_2 - 2(k_2 + l_2)$, $B(M,N) = \Gamma(M)\Gamma(N)/\Gamma(M+N)$ is the Beta-function and ${}_2F_1$ is the hypergeometric function.

Despite the closed form of the analytical expression of equation A.2 its evaluation turns out to be numerically unstable, due to the fact that the resulting series possesses alternating signs, which leads to the subtraction of terms of almost equal absolute values. This problem becomes particularly hard to solve for large values of the quantum numbers. Table A.1 contains the values computed from the analytical expression of equation A.2 compared with the exact values. The exact values of the computed integrals have been obtained by using the mathematical software Mathematica which offers the flexibility to set the precision of numerical evaluations to a large number of digits such that instabilities due to the above mentioned problem do not occur. The integrals have been computed for a magnetic field of 1.0 in effective units and anisotropy $\phi = 60°$. The values of the coefficients c_1 and c_3 that correspond to these specific values of B and ϕ can be obtained by the expressions found in chapter 6.

Already for moderate values $N \gtrsim 10$ a reliable evaluation of the analytical expressions for the electron-electron integrals fails to converge whereas for large values larger than $N \gtrsim$

Table A.1: Comparison of the computed integrals between the analytical expansion and the exact results for various basis functions $m_1 = m_2 = n_1 = n_2 = N$. The fourth column contains the absolute error $\Delta\varepsilon$. The integrals have been evaluated for $B = 1.0$ and $\phi = 60°$. All units are scaled.

N	Exact value	Analytical expansion	$\Delta\varepsilon$
0	$9.296234032641283e-01$	$9.296234032642079e-01$	$8.0e-14$
1	$3.461664587340224e-01$	$3.461664587340197e-01$	$2.7e-15$
2	$3.390906375609172e-01$	$3.390906375609423e-01$	$2.5e-14$
3	$2.421233479478790e-01$	$2.421233479478727e-01$	$6.3e-15$
4	$2.406804934369633e-01$	$2.406804934369568e-01$	$6.5e-15$
5	$1.966846436200880e-01$	$1.966846436202302e-01$	$1.4e-13$
6	$1.961614412833192e-01$	$1.961614412833726e-01$	$5.3e-14$
7	$1.698500416255150e-01$	$1.698500416124770e-01$	$1.3e-11$
8	$1.696039606554327e-01$	$1.696039606027132e-01$	$5.3e-11$
9	$1.516451318474188e-01$	$1.516451320291830e-01$	$1.8e-10$
10	$1.515112751426992e-01$	$1.515112738295054e-01$	$1.3e-09$
11	$1.382608450645461e-01$	$1.382607963909410e-01$	$4.9e-08$
12	$1.381810564985637e-01$	$1.381809618209626e-01$	$9.5e-08$
13	$1.278888321424660e-01$	$1.278863885350074e-01$	$2.4e-06$
14	$1.278382503991035e-01$	$1.278247435483298e-01$	$1.3e-05$
15	$1.195465733111034e-01$	$1.193752973772361e-01$	$1.7e-04$
16	$1.195130988405291e-01$	$1.972873651086735e-01$	$2.2e-03$
17	$1.126484380737557e-01$	$1.119892462372837e-01$	$7.2e-03$
18	$1.126256047285915e-01$	$2.266200485835555e-01$	$1.1e-01$
19	$1.068208788952894e-01$	$-5.039664623646392e-01$	$6.1e-01$
20	$1.068049777966132e-01$	$-2.772799341045502e+00$	$2.9e+00$
21	$1.018129401242934e-01$	$-3.849233597671662e+01$	$3.8e+01$
22	$1.018017228534539e-01$	$-1.211138629801601e+03$	$1.2e+03$
23	$9.744896431041962e-02$	$2.491326570513548e+03$	$2.5e+03$
24	$9.744100585758125e-02$	$6.465158716349043e+04$	$6.5e+04$

15 the computed integrals diverge.

To remedy the instability we applied several techniques such as reordering via complex branch recursion relations following the McMurchie-Davidson scheme. This scheme is mostly used in the calculation of molecular integrals (see ref.[[144]] and references therein). These relations follow if we use the generating formula for the Hermite polynomials

$$H_n(t - A_t) = e^{(t-A_t)^2}(\frac{\partial}{\partial A_t})^n e^{-(t-A_t)^2}$$

and express the electron-electron integral in the form,

$$I_{m_1,m_2,n_1,n_2} = A_{m_1,m_2,n_1,n_2} D^{m_1,m_2,n_1,n_2} R^{k_1;k_2}_{0,0,0,0} \tag{A.3}$$

where the operator,

$$D^{m_1,m_2,n_1,n_2} = (\frac{\partial}{\partial A_t})^{m_1}(\frac{\partial}{\partial A_s})^{m_2}(\frac{\partial}{\partial B_t})^{n_1}(\frac{\partial}{\partial B_s})^{n_2}$$

and the integral,

$$R^{k_1;k_2}_{0,0,0,0} = \int_{-\infty}^{+\infty} dy \int_{-\infty}^{+\infty} dx \frac{e^{t^2+s^2}}{\sqrt{c_3 t^2 + c_1 s^2}} t^{k_1} s^{k_2} e^{-(t-A_t)^2-(t-B_t)^2-(s-A_s)^2-(s-B_s)^2}$$

Hence, by evaluating a set of initial integrals $R^{k_1;k_2}_{i,j,k,l}$ where in practice the indeces i, j, k, l form all permutations between the values 0 and 1 one is possible to construct all higher order integrals I_{m_1,m_2,n_1,n_2} by using recursive formulas of the operator D^{m_1,m_2,n_1,n_2}. At this point we note that the set of initial integrals $R^{k_1;k_2}_{i,j,k,l}$ can be expressed with respect to $R^{k_1;k_2}_{0,0,0,0}$ by the general expression $R^{k_1;k_2}_{i,j,k,l} = 2^{i+j+k+l} R^{k_1+i+k;k_2+j+l}_{0,0,0,0}$. These derivations occur in a straightforward manner by the form of the integrals. This approach, essentially reestablished the instability, which now appears inside the recursive relations, thereby maintaining the problem instead of canceling it. Table A.2 shows the computed integrals by using the presented recursive scheme and the exact values of the integrals for $B = 1.0$ and $\phi = 60°$.

The results in table show that our computed integrals hardly benefitted from the recursive formulas and the efficiency in terms of converged integrals did not improve.

A.3 Numerical integration

In this section we introduce a computational method that is based on numerical integration of the electron-electron integral. This method allowed for the efficient and accurate implementation of integrals even for several hundreds of the quantum numbers. Starting point in our method is the electron-electron integral I_{m_1,m_2,n_1,n_2} in which the Coulomb repulsion term being replaced by an auxiliary Gaussian integral, the so-called Singer transform.

Table A.2: Comparison of the computed integrals between the recursive McMurchie-Davidson scheme and the exact results for various basis functions $m_1 = m_2 = n_1 = n_2 = N$. The fourth column contains the absolute error $\Delta\varepsilon$. The integrals have been evaluated for $B = 1.0$ and $\phi = 60°$. All units are scaled.

N	Exact value	Recursive scheme	$\Delta\varepsilon$
0	$9.296234032641283e-01$	$9.296234032641278e-01$	$4.4e-16$
1	$3.461664587340224e-01$	$3.461664587340228e-01$	$3.9e-16$
2	$3.390906375609172e-01$	$3.390906375609170e-01$	$1.6e-16$
3	$2.421233479478790e-01$	$2.421233479478763e-01$	$2.7e-15$
4	$2.406804934369633e-01$	$2.406804934369557e-01$	$7.6e-15$
5	$1.966846436200880e-01$	$1.966846436200446e-01$	$4.3e-14$
6	$1.961614412833192e-01$	$1.961614412831206e-01$	$2.0e-13$
7	$1.698500416255150e-01$	$1.698500416249788e-01$	$5.4e-13$
8	$1.696039606554327e-01$	$1.696039606548629e-01$	$5.7e-13$
9	$1.516451318474188e-01$	$1.516451318663649e-01$	$1.9e-11$
10	$1.515112751426992e-01$	$1.515112755152837e-01$	$3.7e-10$
11	$1.382608450645461e-01$	$1.382608482167373e-01$	$3.2e-09$
12	$1.381810564985637e-01$	$1.381810716735176e-01$	$1.5e-08$
13	$1.278888321424660e-01$	$1.278888668276617e-01$	$3.5e-08$
14	$1.278382503991035e-01$	$1.278378324125402e-01$	$4.2e-07$
15	$1.195465733111034e-01$	$1.195361544382266e-01$	$1.0e-05$
16	$1.195130988405291e-01$	$1.193803186777891e-01$	$1.3e-04$
17	$1.126484380737557e-01$	$1.122378654349025e-01$	$9.7e-03$
18	$1.126256047285915e-01$	$1.097582838747395e-01$	$1.6e-02$
19	$1.068208788952894e-01$	$1.619270614409117e-01$	$5.5e-02$
20	$1.068049777966132e-01$	$1.237928236906391e+00$	$1.1e+00$
21	$1.018129401242934e-01$	$1.316256588134142e+01$	$1.3e+01$
22	$1.018017228534539e-01$	$1.131245739071058e+02$	$1.1e+02$
23	$9.744896431041962e-02$	$7.674634794295492e+02$	$7.7e+02$
24	$9.744100585758125e-02$	$3.889278613953067e+03$	$3.9e+03$

$$I_{m_1,m_2,n_1,n_2} = \frac{A_{m_1,m_2,n_1,n_2}}{\sqrt{\pi}} \tag{A.4}$$

$$\times \int_{-\infty}^{+\infty} dy \int_{-\infty}^{+\infty} dx \int_{-\infty}^{+\infty} du H_{m_1}(\sqrt{c_1}\, x) H_{m_2}(\sqrt{c_3}\, y) H_{n_1}(\sqrt{c_1}\, y) H_{n_2}(\sqrt{c_3}\, x) e^{-(c_1+u^2)x^2-(c_3+u^2)y^2}$$

By changing variables, $t = \sqrt{c_1 + x^2}$ and $s = \sqrt{c_3 + y^2}$ we can write I_{m_1,m_2,n_1,n_2} in the form,

$$I_{m_1,m_2,n_1,n_2} = \frac{A_{m_1,m_2,n_1,n_2}}{\sqrt{\pi}} \int_{-\infty}^{+\infty} du \frac{1}{\sqrt{c_1 + u^2}} \frac{1}{\sqrt{c_3 + u^2}} I_t(u) I_s(u) \tag{A.5}$$

where the integrals $I_z(u)$, with $z = t, s$ are,

$$I_z = \int_{-\infty}^{+\infty} dz H_m(\frac{\sqrt{c_1}z}{\sqrt{c_1 + u^2}}) H_n(\frac{\sqrt{c_1}z}{\sqrt{c_1 + u^2}}) e^{-z^2}$$

The set of indeces $(m, n) = (m_1, n_1)$ for $z = t$ and $(m, n) = (m_2, n_2)$ for $z = s$. The advantage of writing the integrals I_{m_1,m_2,n_1,n_2} in this form is that integrals $I_z(u)$ can be evaluated numerically exactly as a function of the variable u, by employing a Gauss-Hermite quadrature. In this respect,

$$I_z = \sum_{j=1}^{\frac{m_1+n_1}{2}+1} H_m(\frac{\sqrt{c_1}x_j}{\sqrt{c_1 + u^2}}) H_n(\frac{\sqrt{c_1}x_j}{\sqrt{c_1 + u^2}}) w_j$$

where x_j are the j-th zeros of the Hermite polynomials $H_p(x)$ and $w_j = \frac{2^{p-1} p! \sqrt{\pi}}{p^2 H_{p-1}^2(x_j)}$ where the index $p = \frac{m_1+n_1}{2} + 1 + 1$. In order to check the Gauss-Hermite quadrature one can use an analytical formula for the evaluation of the integrals $I_z(u)$,

$$I_z = \sqrt{\pi} \sum_{k=0}^{min\{m,n\}} 2^k k! \binom{m}{k} \binom{n}{k} (\frac{u^2}{c_z + u^2})^{\frac{m+n}{2}-k} H_{m+n-2k}(0) \tag{A.6}$$

The constants $c_z = c_1$ for $z = t$ and $c_z = c_3$ for $z = s$. A natural question that arises is why we prefer the Gauss-Hermite integration formula instead of the analytical expansion. The main reason for that is that the sum in eq. A.6 converges very slowly. A similar disadvantage with respect to efficiency has also been met in Ref. [145]. So far we have transformed our electron-electron integrals in a $1d$ integration with respect to the auxiliary variable u and have kept additionally our calculation exact. In order to proceed with the integration left we employ a Gauss-Kronrod quadrature [146] which is a standard numrical quadrature technique used very often by mathematical libraries. In table A.3 we present the

results of our numerical technique in comparison with the exact results. We observe that the computed values converge to the exact ones even for high order Hermite polynomials. We remark that the proposed method is particularly efficient and can be therefore employed for the online calculation of the Coulomb matrix elements.

Table A.3: Comparison of the computed integrals between the numerical integration approach and the exact results for various basis functions $m_1 = m_2 = n_1 = n_2 = N$. The fourth column contains the absolute error $|\Delta\varepsilon|$. The integrals have been evaluated for $B = 1.0$ and $\phi = 60°$. All units are scaled.

N	Exact value	Numerical integration	$\|\Delta\varepsilon\|$
0	$9.296234032641283e-01$	$9.296234032641276e-01$	$6.6e-16$
1	$3.461664587340224e-01$	$3.461664587340228e-01$	$3.9e-16$
2	$3.390906375609172e-01$	$3.390906375609178e-01$	$6.1e-16$
3	$2.421233479478790e-01$	$2.421233479478788e-01$	$1.9e-16$
4	$2.406804934369633e-01$	$2.406804934369317e-01$	$3.2e-14$
5	$1.966846436200880e-01$	$1.966846436200863e-01$	$1.7e-15$
6	$1.961614412833192e-01$	$1.961614412833195e-01$	$3.1e-16$
7	$1.698500416255150e-01$	$1.698500416255159e-01$	$8.9e-16$
8	$1.696039606554327e-01$	$1.696039606554364e-01$	$3.7e-15$
9	$1.516451318474188e-01$	$1.516451318474189e-01$	$1.1e-16$
10	$1.515112751426992e-01$	$1.515112751426992e-01$	0.0
11	$1.382608450645461e-01$	$1.382608450645463e-01$	$1.9e-16$
12	$1.381810564985637e-01$	$1.381810564985648e-01$	$1.1e-15$
13	$1.278888321424660e-01$	$1.278888321424663e-01$	$3.1e-16$
14	$1.278382503991035e-01$	$1.278382503991038e-01$	$3.1e-16$
15	$1.195465733111034e-01$	$1.195465733111046e-01$	$1.2e-15$
16	$1.195130988405291e-01$	$1.195130988405286e-01$	$5.0e-16$
17	$1.126484380737557e-01$	$1.126484380737580e-01$	$2.3e-15$
18	$1.126256047285915e-01$	$1.126256047285920e-01$	$5.0e-16$
19	$1.068208788952894e-01$	$1.068208788952800e-01$	$9.4e-15$
20	$1.068049777966132e-01$	$1.068049777966136e-01$	$4.0e-16$
21	$1.018129401242934e-01$	$1.018129401242923e-01$	$1.1e-15$
22	$1.018017228534539e-01$	$1.018017228534560e-01$	$2.1e-15$
23	$9.744896431041962e-02$	$9.744896431042029e-02$	$6.7e-15$
24	$9.744100585758125e-02$	$9.744100585758363e-02$	$2.4e-14$

In figure A.1 we plot the logarithm of the absolute error as we increase the order of the basis functions' polynomials for the several techniques we presented throughout the ap-

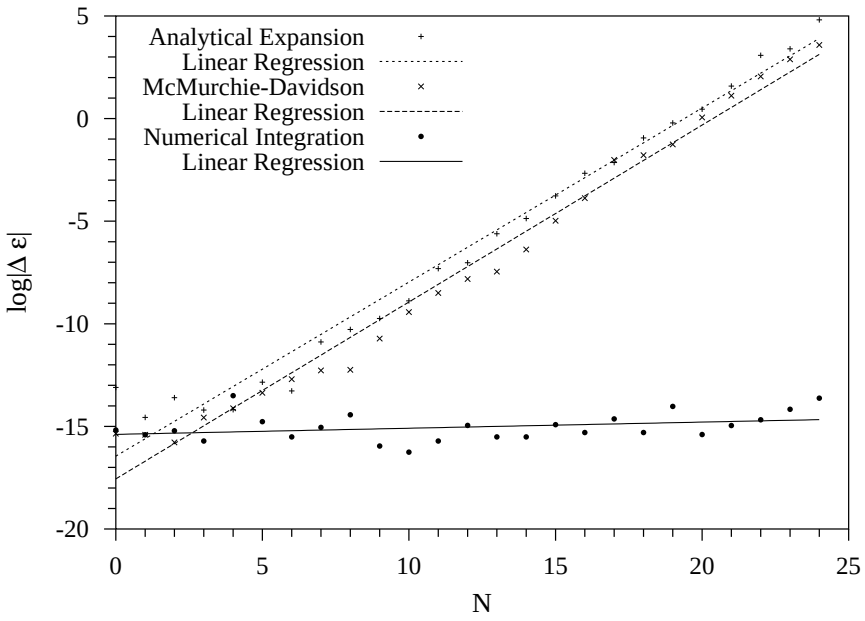

Figure A.1: Logarithmic dependence of the absolute error for the analytical expansion, the recursive McMurchie-Davidson scheme and the numerical integration with increasing the order of the basis functions' polynomials. A linear regression model has been applied to describe all approaches with dotted, dashed and solid lines respectively.

pendix. The graph shows an exponential increase of the instability for the analytical expansion which hardly improves when employing recursive techniques, thereby maintaining the exponential trend. By employing the numerical quadrature techniques, the absolute error oscillates around a very high precision.

Appendix B

Acknowledgements

I think this part of the thesis is one of the most important ones because without these people to which I owe gratitude, the realisation of the present thesis would be almost improbable. I am writing these comments with a feeling of nostalgy for all the great moments I have had during the time of my PhD and owe mostly to these people as well as deeply regreting for the fact that this period is over..

Prof. Dr. Fotis Diakonos, for all scientific discussions as well as friendly atmosphere in his group, during my Diploma in the University of Athens, which have inspired me to deal with science. I am almost unlimited grateful to him because he pumped me to the experience of living in Heidelberg, the most unforgettable experience in my life so far.

Prof. Dr. Jochen Schirmer, for his comprehensive lectures which consist the major part of my education regarding many-body methods. I also thank him for the time he devoted in our discussions, which have been always characterised by pleasure. This thesis leaves him with my most sincere wishes that in the next years his knowledge will extend in greek language as well as beyond the first ten rimes in the classical work of Homer "Odyssey".

Leo Löffel the best poet writer I have ever met at a personal level and apart from it, the senior forest-guard who is still looking for his forest and the same time can make the frogs look so sympathetic. I thank him for showing to me how important it is some times to write poems instead of writing dissertations. What?! You do not know who is Löffel?! You still have some time to know..

PhD-student and nowadays a very promising postdoc Alexej Streltsov with whom I have shared the largest amount of my working place and time.

PhD-student Daniel Buchholz with whom I have had extensive discussions and collaboration with respect to the physics of quantum transport. I also thank him for carefully reading the

manusript of the thesis and supplying me with his very detailed comments.

Researcher Dr. Giorgos Fagas for all discussions and introduction with respect to the field of quantum transport in both physical and computational sense. Collaboration with him has been always very fruitful.

Ms. Sofia Roumbakis for giving color to new perspectives with respect to my life.

Dr. Rosario Gonzalez-Ferez colleague and simultaneously one of my best friends for all discussions and time we have spent together. It has been a great experience to have her known.

A number of friends that supported me and tolerated extensively long discussions regarding my work, which from an helicopter's point of view, i.e. these acknowledgements, may sound uninteresting to them. In this regard, I would like to thank Stathis, student in dentistry, Giorgio, musician and piano player and Theo, PhD-student in prehistoric archaeology for the interesting time we have spent together. I wish to all of them good luck!

I would also like to thank all *members of the Theoretical Chemistry Group for working environment stimulating the work and especially our system administrators, who made it possible to perform all computations.*

I am grateful to Eva Zanders and Annette Braun, ex- and present secretaries of our group for their support any time it had been required and creating home-like conditions in the group.

I am grateful to the director of the group Prof. Lorenz S. Cederbaum for creating an excelent and open atmosphere in the group and his continuously friendly as well as enjoyable company.

I would like also to thank all members of the International Graduate College (IGC) 710: "Complex Processes: Simulation Modelling and Optimization". They all showed me how fascinating, pleasant and interesting the collaboration from a mathematical point of view can be.

I am also grateful to the speaker of the IGC 710 Prof. Hans-Georg Bock for his great and highly appreciable work that keeps this community live and supports interdisciplinarity and cooperation between people from different scientific communities. He may remain sure that the horizons before and after the experience of joining IGC are almost uncomparably wider.

I would like also to thank both secretaries of the IGC 710, Astrid Sudmann and Ria Lynott for the very friendly atmosphere they have created in the framework of this scholarship thereby

harmonically joining the international level of students with the standards of the german culture. I could hardly imagine a more suitable and more pleasant environment.

Prof. Peter Bastian for showing to me apart from the optimised communication among processors how pleasant and creative, in other words optimal in a human sense, communication between people can be.

I am unlimited grateful to my supervisor Prof. Dr. Peter Schmelcher for his constant support and inspiration regarding the scientific part of my thesis. His comments have been always very fruitful, thorough and professional thereby severely improving this piece of work.

Finally, I would like to express my most sincere thanks to my parents, as well as my brother, for their constant support and for the fact that they have been always present, even invisible, during the years of my PhD in Heidelberg.

Appendix C

Publication list, contributions to conferences and invited speeches

C.1 Publications

- P. S. DROUVELIS, P. SCHMELCHER AND F. K. DIAKONOS: *Two-electron anisotropic quantum dots.* Europhysics Letters, Volume 64, Pages 232-238. (2003)

- P.S. DROUVELIS, P. SCHMELCHER AND F.K. DIAKONOS: *Global view on the electronic properties of two-electron anisotropic quantum dots.* Physical Review B, Volume 69, Article 035333 Pages 1-15. (2004)

- P. S. DROUVELIS, P. SCHMELCHER AND F. K. DIAKONOS: *Probing the shape of quantum dots with magnetic fields.* Physical Review B, Volume 69, Article 155312 Pages 1-5. (2004)

- P. S. DROUVELIS, P. SCHMELCHER AND F. K. DIAKONOS: *Effects of anisotropy and magnetic fields on two-electron parabolic quantum dots.* Journal of Physics: Condensed Matter, Volume 16, Pages 3633-3646. (2004)

- P. S. DROUVELIS, P. SCHMELCHER AND P. BASTIAN: *Parallel implementation of the recursive Green's function method.* Journal of Computational Physics, Volume 215, Pages 741-756. (2006)

- D. BUCHHOLZ, P. S. DROUVELIS AND P. SCHMELCHER: *Single-electron quantum dot in a spatially periodic magnetic field.* Physical Review B, Volume 73, Article 235346, Pages 1-16. (2006)

- P. S. DROUVELIS, G. FAGAS, AND P. SCHMELCHER: *Magnetically controlled current flow in coupled-dot arrays.*

C.2 Contributions to conferences

- *Two-electron anisotropic quantum dots.* SPIN AND CHARGE TRANSPORT IN NANOSTRUCTURES, September 1-5, Braga, Portugal. 2003
- *Two-electron anisotropic quantum dots.* 316. WE HERAEUS SEMINAR: CORRELATION, DECOHERENCE AND SPIN EFFECTS IN SIMPLE AND COMPLEX QUANTUM DOT SYSTEMS, October 23 - 25, Physikzentrum Bad Honnef, Germany. 2003
- *Two-electron anisotropic quantum dots.* 69. ANNUAL MEETING OF THE DEUTSCHE PHYSIKALISCHE GESELLSCHAFT (DPG), March 4 - 9, Berlin, Germany. 2005
- *Parallel recursive Green's function method.* 6TH INTERNATIONAL WILHELM AND ELSE HERAEUS SUMMER SCHOOL ON SPINELECTRONICS, August 1 - 12, Wittenberg, Germany. 2005
- *Parallel recursive Green's function method.* COMPUTATIONAL NANOSCIENCE: DO IT YOURSELF!, NIC WINTER SCHOOL, February 14 - 22, Jülich, Germany. 2006
- *Parallel recursive Green's function method.* DPG - SPRING MEETING OF THE DIVISION CONDENSED MATTER, March 26 - 31, Dresden, Germany. 2006
- *Parallel recursive Green's function method.* IWCE-11 INTERNATIONAL WORKSHOP ON COMPUTATIONAL ELECTRONICS, May 25 - 27, Dresden, Austria. 2006

C.3 Invited Speeches

- *Interplay of regularity and chaos in two-electron anisotropic quantum dots.* DEPARTMENT OF PHYSICS, UNIVERSITY OF ATHENS, January 10, Athens, Greece. 2003
- *Two-electron anisotropic quantum dots.* DEPARTMENT OF PHYSICS, UNIVERSITY OF HAMBURG, April 20, Hamburg, Germany. 2004
- *Two-electron anisotropic quantum dots.* DEPARTMENT OF PHYSICS, UNIVERSITY OF NAPOLI, May 3, Napoli, Italy. 2004
- *Mathematical modeling and simulation of quantum mesoscopic transport.* ANNUAL COLLOQUIUM OF THE INTERNATIONAL GRADUATE COLLEGE (IGK 710), December 3, Academy of Sciences, Heidelberg, Germany. 2004
- *Quantum magnetotransport through quantum dot arrays using parallel computing techniques.* NATIONAL HELLENIC RESEARCH FOUNDATION, April 10, Athens, Greece. 2006

- *Quantum magnetotransport through quantum dot arrays using parallel computing techniques.* DEPARTMENT OF PHYSICS, UNIVERSITY OF ATHENS, April 13, Athens, Greece. 2006

Bibliography

[1] R. Turton, *The Quantum Dot: A Journey into the Future of Microelectonics* (Oxford University Press, 1996).

[2] S. Datta, *Quantum Transport: Atom to Transistor* (Cambridge University Press, 2005).

[3] H. Grabert and M.H. Devoret *Single Charge Tunneling* (Plenum Press, New York, 1992).

[4] I. Žutić *et al*, Rev.Mod.Phys. **76**, 323 (2004).

[5] S. Datta, *Electronic Transport in Mesoscopic Systems* (Cambridge University Press, 1995).

[6] G. Bergmann, Phys. Rep. **107**, 1 (1984).

[7] B.L. Altschuler, JETP Lett. **41**, 648 (1985).

[8] P.A. Lee and A.D. Stone, Phys. Rev. Lett. **55**, 1622 (1985).

[9] S. Washburn and R.A. Webb, Adv. Phys. **35**, 375 (1986).

[10] Y. Alhassid, Rev. Mod. Phys. **72**, 895 (2000).

[11] R. Landauer, IBM J. Res. Dev. **32**, 306 (1988); R. Landauer, Physica Scripta **T42**, 110 (1992).

[12] H. Haug and A.-P. Jauho, *Quantum Kinetics and Optics of Semiconductors* (Springer-Verlag, Berlin, 1996).

[13] Y. Meir and N.S. Wingreen, Phys. Rev. Lett. **68**, 2512 (1992).

[14] D.K. Ferry and S.M. Goodnick, *Transport in Nanostructures* (Cambridge University Press, 1997).

[15] D.S. Fisher and P.A. Lee, Phys. Rev. B **23**, 6851 (1981).

[16] M. Büttiker, IBM J. Res. Dev. **32**, 63 (1988).

[17] H.M. Pastawski, L.E.F. Foa Torres and E. Medina, Chem. Phys. **281**, 257 (2002).

[18] M. Macucci, G. Iannacone, G. Basso and B. Pellegrini, Phys. Rev. B **67**, 115339 (2003).

[19] H.R. Frohne, M.J. McLennan and S. Datta, J. Appl. Phys. **66**, 2699 (1989).

[20] S. Rotter, J.-Z. Tang,L. Wirtz, J. Trost and J. Burgdörfer, Phys. Rev. B **62**, 1950 (2000).

[21] S. Rotter, B. Weingartner, N. Rohringer and J. Burgdörfer, Phys. Rev. B **68**, 165302 (2003).

[22] G. Metalidis and P. Bruno, Phys. Rev. B **72**, 235304 (2005).

[23] D. Mamaluy, M. Sabathil and P. Vogl, J. Appl. Phys. **93**, 4628 (2003).

[24] D. Mamaluy, D. Vasileska, M. Sabathil, T. Zibold and P. Vogl, Phys. Rev. B **71**, 245321 (2005).

[25] E.F. Van de Velde, *Concurrent Scientific Computing* (Springer-Verlag, 1994).

[26] V. Kumar, A. Grama, A. Gupta and G. Karypis, *Introduction to Parallel Computing* (Benjamin-Cummings, 1994).

[27] G. Fagas, G. Tkachov, A. Pfund and K. Richter, Phys. Rev. B **71**, 224510 (2005).

[28] H.U. Baranger *et al*, Phys. Rev. B **44**, 10637 (1991).

[29] I.V. Zozoulenko, F.A. Maaø and E.H. Hauge, Phys. Rev. B **53**, 7975 (1996).

[30] http://helics.uni-hd.de/

[31] N.G. Fytas *et al*, Phys. Rev. B **72**, 085336 (2005).

[32] J. Zak, Phys. Rev. **134**, A1602 (1964); J. Zak, Phys. Rev. **134**, A1607 (1964).

[33] E. Brown, Phys. Rev. **133**, A1038 (1964).

[34] D.R. Hofstadter, Phys. Rev. B **14**, 2239 (1976).

[35] C. Albrecht, J. H. Smet, K. von Klitzing, D. Weiss, R. Hennig, M. Langenbuch, M. Suhrke, U. Rössler, V. Umansky and H. Schweizer, Phys. Rev. Lett. **86**, 147 (2001).

[36] R.R. Gerhardts, D. Weiss and U. Wulf, Phys. Rev. B **43**, R5192 (1991).

[37] M. Langenbuch, M. Suhrke, and U. Rössler, Europhys. Lett. **61**, 520 (2003).

[38] J.F. Song, Y. Ochiai, and J.P. Bird, Appl. Phys. Lett. **82**, 4561 (2003).

[39] S. Oberholzer, E. V. Sukhorukov, C. Strunk, C. Schönenberger, T. Heinzel, and M. Holland, Phys. Rev. Lett. **86**, 2114 (2001).

[40] M. Elhassan, R. Akis, J. Bird, D. Ferry, T. Ida, and K. Ishibashi, Phys. Rev. B **70**, 205341 (2004).

[41] G. Fagas, A. Kambili and M. Elstner, Chem. Phys. Lett., **389**, 268 (2004).

[42] L. Jacak, P. Hawrylak and A. Wojs, *Quantum Dots* (Springer, 1997).

[43] T. Chakraborty, *Quantum Dots* (Elsevier, 1999).

[44] S.M. Reimann and M. Manninen, Rev. Mod. Phys. **74**, 1283 (2002).

[45] L.P. Kouwenhoven, D.G. Austing and S. Tarucha, Rep. Prog. Phys **64**, 701 (2001).

[46] S.Tarucha *et al*, Phys. Rev. Lett. **77**, 3613 (1996).

[47] L.P. Kouwenhoven *et al*, Science **278**, 1788 (1997).

[48] L. Kouwenhoven and C. Marcus, Physics World **11**, 35 (1998).

[49] J. Weis *et al*, Semiconduct. Sci. Technol. **9**, 1890 (1994).

[50] P.A. Maksym and T. Chakraborty, Phys. Rev. Lett. **65**, 108 (1990).

[51] U. Merkt, J. Huser and M. Wagner, Phys. Rev. B **43**, 7320 (1991).

[52] P.A. Maksym and T. Chakraborty, Phys. Rev. B **45**, 1947 (1992).

[53] P.A. Maksym, Physica B **184**, 385 (1993).

[54] D. Pfannkuche, V. Gudmundson and P.A. Maksym, Phys. Rev. B **47**, 2244 (1993).

[55] D. Pfannkuche, R.R. Gerhardts, V. Gudmundson and P.A. Maksym, Physica B **189**, 6 (1993).

[56] P. Hawrylak, Phys. Rev. Lett. **71**, 3347 (1993).

[57] S.-R. Eric Yang, A.H. MacDonald and M.D. Johnson, Phys. Rev. Lett. **71**, 3194 (1993).

[58] J.J. Palacios, L. Martín-Moreno, G. Chiappe, E. Louis and C. Tejedor, Phys. Rev. B **50**, 5760 (1994).

[59] D. Pfannkuche and S.E. Ulloa, Phys. Rev. Lett. **74**, 1194 (1995).

[60] P.A. Maksym, L.D. Hallam and J. Weis, Physica B **212**, 213 (1995).

[61] M. Eto, Jpn. J. Appl. Phys. **36**, 3924 (1997).

[62] A. Wójs and P. Hawrylak, Phys. Rev. B **56**, 13227 (1997).

[63] G. Lamouche and G. Fishman, J. Phys.: Condens. Matter **10**, 7857 (1998).

[64] W. Xin-Qiang and M. Ling-Feng, J. Phys.: Condens. Matter **10**, 11025 (1998).

[65] M. Eto, Jpn. J. Appl. Phys. **38**, 376 (1999).

[66] W.Y. Ruan and H.-F. Cheung, J. Phys.: Condens. Matter **11**, 435 (1999).

[67] S.A. Mikhailov and N.A. Savostianova, Phys. Rev. B **66**, 033307 (2002).

[68] S.A. Mikhailov, Phys. Rev. B **66**, 153313 (2002).

[69] M.B. Tavernier, E. Anisimovas, F.M. Peeters, B. Szafran , J. Adamowski and S. Bednarek, Phys. Rev. B **68**, 205305 (2003).

[70] M.-C. Cha and S.-R. Eric Yang, Phys. Rev. B **67**, 205312 (2003).

[71] B. Szafran, S. Bednarek and J. Adamowski, Phys. Rev. B **67**, 115323 (2003).

[72] P. Lucignano, B. Jouault and A. Tagliacozzo, Phys. Rev. B **69**, 045314 (2004).

[73] M. El-Said, Phys. Status Solidi (b) **193**, 105 (1996).

[74] A. Gonzalez, R. Perez and P. Fileviez, J. Phys.: Condens. Matter **9**, 8465 (1997).

[75] E. Anisimovas and A. Matulis, J. Phys.: Condens. Matter **10**, 601 (1998).

[76] W.Y. Ruan, K.S. Chan, H.P. Ho and E.Y. Pun, J. Phys.: Condens. Matter **12**, 3911 (2000).

[77] R.G. Nazmitdinov, N.S. Simonović and J.M. Rost, Phys. Rev. B **65**, 155307 (2002).

[78] S. Klama and E.G. Mishchenko, J. Phys.: Condens. Matter **10**, 3411 (1998).

[79] R.M.G. García-Castelán, W.S. Choe and Y.C. Lee, Phys. Rev. B **57**, 9792 (1998).

[80] A. Gonzalez, J. Phys.: Condens. Matt. **9**, 4643 (1997).

[81] M. Wagner, U. Merkt and A.V. Chaplik, Phys. Rev. B **45**, 1951 (1992).

[82] M. Dineykhan and R.G. Nazmitdinov, J. Phys.: Condens. Matter **11**, L83 (1999).

[83] W.Y. Ruan, Y.Y. Liu, C.G. Bao and Z.Q. Zhang, Phys. Rev. B **51**, 7942 (1995).

[84] P.A. Maksym Phys. Rev. B **53**, 10871 (1996).

[85] C.G. Bao, Phys. Rev. Lett. **79**, 3475 (1997).

[86] P.A. Maksym, H. Imamura, G.P. Mallon and H. Aoki, J. Phys.: Condens. Matter **12**, R299 (2000).

[87] R.C. Ashoori, H.L. Stormer, J.S. Weiner, L.N. Pfeiffer, K.W. Baldwin and K.W. West, Phys. Rev. Lett. **71**, 613 (1993).

[88] B. Su, V.J. Goldman and J.E. Cunningham, Surface Science **305**, 566 (1994).

[89] T. Schmidt, M. Tewordt, R.H. Blick, R.J. Haug, D. Pfannkuche, K. .von Klitzing, A. Förster and H. Lüth, Phys. Rev. B **51**, 5570 (1995).

[90] W.G. van der Wiel, T.H. Oosterkamp, J.W. Jannsen, L.P. Kouwenhoven, D.G. Austing, T. Honda and S. Tarucha, Physica B **256**, 173 (1998).

[91] M. Ciorga, A. Wensauer, M. Pioro-Ladriere, M. Korkusinski, J. Kyriakidis, A.S. Sachrajda and P. Hawrylak, Phys. Rev. Lett. **88**, 256804 (2002).

[92] T.H. Oosterkamp, J.W. Jannsen, L.P. Kouwenhoven, D.G. Austing, T. Honda and S. Tarucha, Phys. Rev. Lett. **82**, 2931 (1999).

[93] S. Tarucha *et al*, Appl. Phys. A **71**, 367 (2000).

[94] P.A. Maksym, Physica B **249**, 233 (1998).

[95] T. Ezaki, N. Mori and C. Hamaguchi, Phys. Rev. B **56**, 6428 (1997).

[96] T. Ezaki, N. Mori and C. Hamaguchi, Semicond. Sci. Technol. **13**, A1 (1998).

[97] T. Ezaki, N. Mori and C. Hamaguchi, Physica B **249-251**, 238 (1998).

[98] M. Fujito, A. Natori and H. Yasumaga, Phys. Rev. B **53**, 9952 (1996).

[99] I.-H. Lee *et al*, Phys. Rev. B **57**, 9035 (1998).

[100] I.-H. Lee, Y.H. Kim and K.H. Ahn, J. Phys. Condens. Matt. **13**, 1987 (2001).

[101] S.M. Reimann *et al*, Phys. Rev. B **58**, 8111 (1998).

[102] S.M. Reimann *et al*, Physica E **2**, 648 (1998).

[103] S.M. Reimann *et al*, Eur. Phys. J. D **9**, 105 (1999).

[104] K. Hirose and N.S. Wingreen, Phys. Rev. B **59**, 4604 (1999).

[105] D.G. Austing *et al*, Phys. Rev. B **60**, 11514 (1999).

[106] S. Tarucha, D.G. Austing, T. Honda, T. van der Hage and L.P. Kouwenhoven, Japan. J. Appl. Phys. **36**, 3917 (1997).

[107] P.S. Drouvelis, P. Schmelcher and F.K. Diakonos, Europhys. Lett. **64**, 232 (2003).

[108] P.S. Drouvelis, P. Schmelcher and F.K. Diakonos, Phys. Rev. B **69**, 035333 (2004).

[109] P.S. Drouvelis, P. Schmelcher and F.K. Diakonos, Phys. Rev. B **69**, 155312 (2004).

[110] P.S. Drouvelis, P. Schmelcher and F.K. Diakonos, J. Phys.: Condens. Matter **16**, 3633 (2004).

[111] I. Magnúsdóttir and V. Gudmundson, Phys. Rev. B **61**, 10229 (2000).

[112] I.-H. Lee, V. Rao, R.M. Martin, J.-P. Leburton, Phys. Rev. B **57**, 9035 (1999).

[113] S.M. Reimann, M. Koskinen, P.E. Lindelof and M. Manninen, Physica E **2**, 648 (1998).

[114] A.V. Madhav and T. Chakraborty, Phys. Rev. B **49**, 8163 (1994).

[115] Y. Tokura, S. Sasaki, D.G. Austing and S. Tarucha, Physica B **298**, 260 (2001).

[116] R.G. Nazmitdinov, N.S. Simonović and J.M. Rost, Phys. Rev. B **65**, 155307 (2002).

[117] N.S. Simonović and R.G. Nazmitdinov, Phys. Rev. B **67**, 041305(R) (2003).

[118] M. Dineykhan and R.G. Nazmitdinov, Phys. Rev. B **55**, 13707 (1997).

[119] G. Cantele, D. Ninno and G. Iadonisi, J. Phys.: Condens. Matter **12**, 9019 (2000).

[120] G. Cantele, D. Ninno and G. Iadonisi, Phys. Rev. B **64**, 125325 (2001).

[121] G. Cantele, D. Ninno and G. Iadonisi, Nanoletters **1**, 121 (2001).

[122] L.C. Lew Yan Voon and M. Willatzen J. Phys.: Condens. Matt. **14**, 13667 (2002).

[123] P. Bakshi *et al*, Phys. Rev. B **42**, 7416 (1990).

[124] F.M. Peeters Phys. Rev. B **42**, 1486 (1990).

[125] W. Kohn, Phys. Rev. **115**, 1160 (1959).

[126] W. Kohn, Phys.Rev. **123**, 1242 (1961).

[127] L. Brey, N.F. Johnson and B.I. Halperin, Phys. Rev. B **40**, 10647 (1989).

[128] M. Taut, J. Phys. A **27**, 1045 (1994).

[129] O. Bohigas in *Chaos and Quantum Physics, Les Houches, 1989,* edited by M.-J. Giannoni, A. Voros and J. Zinn-Justin (North-Holland, 1991) pp.91-199.

[130] M.L. Mehta, *Random Matrices, Academic* (Academic Press, 1991).

[131] F. Haake, *Quantum Signatures of Chaos* (Springer, 2000).

[132] T.A. Brody, Lett. Nuovo Cimento **7**, 482 (1973).

[133] A. Hönig and D. Wintgen, Phys. Rev. A **39**, 5642 (1989).

[134] M.V. Berry and M. Robnik, J. Phys. A **17**, 2413 (1984).

[135] A. Pandey, O. Bohigas and M.J. Giannoni, J. Phys. A **22**, 4083 (1989).

[136] L.L. Foldy and S.E. Stansfield, Phys. Rev. A **35**, 1415 (1987).

[137] K. Ganesan and M. Lakshmanan, Phys. Rev. A **42**, 3940 (1990).

[138] M. Moore and R. Blümel, Phys. Rev. A **48**, 3082 (1993).

[139] M.W. Beims and J.A.C. Gallas, Phys. Rev. A **62**, 043410 (2000).

[140] Dippel O., Schmelcher P. and Cederbaum L.S. Phys. Rev. A **49**, 4415 (1994).

[141] Gradshteyn I.S. and Ryzhik I.M., *Table of Integrals, Series and Products* (New York: Academic, 1980).

[142] W.D. Heiss and R.G. Nazmitdinov R.G., JETP Lett. **68**, 915 (1998).

[143] M. Abramowitz and I.A. Stegun, *Handbook of Mathematical Functions* (Dover,New York, 1970).

[144] T. Helgaker and P.R. Taylor, in *Modern Electronic Structure Theory,* edited by D.R. Yarkoni (World Scientific, 1995), Part II, Chap.12.

[145] M. Stone, H.W. Wyld and R.L. Schult, Phys. Rev. B **45**, 14156 (1992).

[146] R. Piessens *et al, QUADPACK A Subroutine Package for Automatic Integration* (Springer, 1983).

a) Ich erkläre hiermit an Eides statt, daß ich die vorgelegte Dissertation selbst verfaßt und mich dabei keiner anderen als der von mir ausdrücklich bezeichneten Quellen und Hilfen bedient habe.

b) Ich erkläre hiermit an Eides statt, daß ich an keiner anderen Stelle ein Prüfungsverfahren beantragt beziehungsweise die Dissertation in dieser oder anderer Form bereits anderweitig als Prüfungsarbeit verwendet oder einer anderen Fakultät als Dissertation vorgelegt habe.

Panagiotis Drouvelis